AD NUMBER

AD487783

LIMITATION CHANGES

TO:

Approved for public release; distribution is unlimited.

FROM:

Distribution authorized to U.S. Gov't. agencies and their contractors; Critical Technology; JAN 1966. Other requests shall be referred to Air Force Office of Scientific Research, Bolling AFB, Washington, DC 20332. This document contains export-controlled technical data.

AUTHORITY

AFOSR ltr dtd 12 Nov 1971

AFOSR Scientific Report
AFOSR 66-0858

Contract AF 49(638)-1263
Project 9751-01

COMBUSTION INSTABILITY IN LIQUID PROPELLANT ROCKET ENGINES:

Bi-Propellant Spray Combustion

by

Sanford S. Hammer, Vito D. Agosta

and William T. Peschke

JANUARY 1966

POLYTECHNIC INSTITUTE OF BROOKLYN

DEPARTMENT
of
AEROSPACE ENGINEERING
and
APPLIED MECHANICS

PIBAL REPORT NO. 891

COMBUSTION INSTABILITY IN LIQUID PROPELLANT ROCKET ENGINES:

Bi-Propellant Spray Combustion

by

Sanford S. Hammer, Vito D. Agosta,

and William T. Peschke

This study was supported by the
Air Force Office of Scientific Research
under Contract No. AF 49(638)-1263,
Project No. 9751-01.

Polytechnic Institute of Brooklyn

Department

of

Aerospace Engineering and Applied Mechanics

January 1966

PIBAL Report No. 891

COMBUSTION INSTABILITY IN LIQUID PROPELLANT ROCKET ENGINES:

Bi-Propellant Spray Combustion †

by

Sanford S. Hammer,* Vito D. Agosta** and William T. Peschke***

Polytechnic Institute of Brooklyn

SUMMARY

The present investigation is concerned with the development of an analytical bi-propellant spray combustion model and an experimental investigation of steady state and longitudinal wave propagation phenomena in liquid propellant rocket engines.

A model is proposed for the combustion of a bi-propellant spray in a rocket motor. The model considers evaporation of both fuel and oxidizer without any restrictive assumption concerning their relative rates. The spray is approximated by n different size fuel drops and m different size oxidant drops. Each group of drops has N_n or N_m drops per second flowing

---

† This study was supported by the Air Force Office of Scientific Research under Contract No. AF 49(638)-1263, Project No. 9751-01.

* Research Associate, Dept. of Aerospace Engineering and Applied Mechanics.

** Professor of Aerospace Engineering.

*** Research Assistant, Dept. of Aerospace Engineering and Applied Mechanics.

in the combustion chamber at any section. The gas is assumed to be in chemical equilibrium and is coupled to the spray analysis by heat, mass, and momentum transfer. Combustion gas properties are evaluated at the local temperature, pressure, and O/F ratio. The solution of the problem requires the simultaneous solution of six ordinary differential equations. The system of coupled equations are integrated and solved on an IBM 7040 digital computer. The analysis is applied to a 500 lbf. nominal thrust JP-5A, liquid oxygen rocket motor. The results indicate that the oxidizer evaporates more rapidly than the fuel, producing a combustion gas O/F ratio during the initial stages of evaporation which is considerably greater than the O/F ratio of the injected propellants. Therefore, the flame temperature in the beginning of the chamber, and the subsequent rate of fuel evaporation are less than those predicted by a model which assumes proportional rates of oxidizer/fuel evaporation.

A series of steady state and wave propagation experiments are conducted with a 2-in.-diam. variable length rocket motor using JP-5A and liquid oxygen. A simple converging-diverging nozzle is employed to yield high chamber exit Mach numbers (0.45). The steady state experiments are primarily concerned with the measurement of axial combustion chamber pressure gradients in order to correlate the spray combustion analysis and provide initial conditions for wave propagation studies. The data obtained is useful in establishing design criteria for steady state operation and optimization of the rocket chamber geometry. The results from ten different injector configurations indicate that the slope of the axial pressure gradient can be altered by changing the impingement point and/or the diameter of the fuel orifice.

Wave propagation experiments are conducted by utilizing the combustion chamber as a driven tube and mounting a diaphragm and high pressure driver tube upstream of the injector. The initial results indicate that the incident wave causes drop shattering, and prove that wavelet generation, coalescence and wave steepening occur. In addition, the downstream propagating wave is shown to reflect from the sonic plane causing the chamber-nozzle cavity to behave as a half-wave resonator. The fundamental mode of longitudinal oscillation has a frequency equal to that predicted from simple acoustic theory with mass motion.

Additional experiments are conducted to determine the conditions under which input disturbances attenuate or amplify in liquid propellant rocket motors. The results indicate that wave steepening and pressure amplification are strongly coupled to the steady state gas dynamic flow field through which the wave must propagate. Those injector-chamber configurations which result in rapid propellant utilization and high steady-state axial pressure gradient slopes tend to inhibit wave growth. Less rapid conversion to gaseous products, with an attendant low pressure gradient, provides an energy and mass source to drive the wave and amplify the base pressure.

TABLE OF CONTENTS

LIST OF ILLUSTRATIONS

LIST OF ILLUSTRATIONS (Contd.)

SECTION I

INTRODUCTION

A. Definition of the Problem

The occurrence of high frequency oscillatory combustion is of major concern in the development of rocket motors. Basically, high frequency instability involves finite amplitude pressure wave propagation in the combustor and nozzle, which often results in complete destruction of the engine. A coupling mechanism between the wave and gas dynamic processes supplies energy to sustain the oscillations. The instability phenomena has been observed in liquid, solid and pre-mixed gaseous rockets.

The mode of oscillation is primarily dependent upon the geometric configuration of the chamber nozzle cavity. Longitudinal oscillations are prevalent in thrust chambers with large length to diameter ratios, while transverse modes are associated with large diameter, small length units. The transverse waves manifest themselves as radial, tangential, sloshing or spinning modes. The waveform of the longitudinal instability can be either sinusoidal or shock fronted with exponential decay.

Instabilities may be initiated as a result of a spontaneous action within the gas dynamic field or as a consequence of an external triggering action. In the former case, small disturbances in the flow are amplified by the energy addition coupling mechanism with the combustion process. The triggering action type of instability initiation results from large disturbances to the system, such as, vibrations from the engine frame, abrupt changes in

the feed system, etc. The latter mode of initiation involves nonlinear effects at the very beginning of the instability. Nonlinear effects are present with any finite amplitude wave so that they must be considered even for the spontaneous initiation where a small perturbation grows in amplitude. The nonlinearities referred to here manifest themselves ultimately as wave distortion phenomena, which in the limit cause either complete attenuation or shock formation.

Thus the problem of combustion instability in a liquid propellant rocket engine includes: (1) a forcing mechanism which initiates oscillatory behavior; (2) an energy coupling mechanism which sustains these oscillations; and (3) mechanisms which either attenuate or amplify the oscillations. The forcing mechanisms that initiate the instability are generally random in nature and are not amenable to a systematic analysis. The solution to the instability problem therefore resides in a complete understanding of the coupling and attenuation mechanisms.

Energy coupling between the propagating wave and the combustion process is dependent upon the relative magnitudes of characteristic times associated with the source (combustion) and sink (wave). If the relaxation time of a significant transport process such as liquid atomization, vaporization or chemical reaction is less than or equal to the wave residence time in a volume element, coupling can occur with resultant unstable operation. The leading edge of a passing wave in a reacting droplet system can increase the rate of evaporation, which couples as a mass source to the trailing edge of the passing wave, thus producing amplification. It can be further seen

that, for a long relaxation time, the mass source can generate wavelets that coalesce as they propagate and ultimately overtake the initial wave that caused the disturbance, again causing amplification. In addition, as a wave propagates in a gas, it deforms. A compression wave will steepen in a decelerating flow; an expansion wave will broaden in an accelerating flow. A compression wave in an accelerating flow and an expansion wave in a decelerating flow will either broaden or steepen, depending on the wave slope and the velocity gradient of the gaseous medium. Therefore, as a wave moves in a rocket chamber, it will change its geometry, which then alters its residence time in a volume element. In addition, the energy in a wave is a function of its velocity and waveform. Thus, the wave slope assumes a major role in that it determines, by modifying the effective wavelength and amplitude, the nature of the energy or mass coupling to the propagating wave and the ultimate stability of the system.

In order to achieve a series of rational engineering principles for designing stable rocket engines it is necessary to investigate the mechanisms that cause energy coupling and wave deformation. This thesis is directed to that end. Section II presents a steady state aerothermochemical analysis for a liquid bipropellant rocket motor with small contraction ratio. Both fuel and oxidizer ballistics are analyzed simultaneously. The solution to this problem provides a means for synthesizing injector-chamber-nozzle configurations for optimum steady state operation, as well as providing well defined initial and boundary conditions for wave propagation studies. Section III describes the experimental facility designed for this investigation.

Section IV presents the results of an experimental investigation of steady state behavior in a liquid bipropellant rocket motor. In addition, longitudinal wave propagation studies were conducted in order to define the parameters that determine whether an input disturbance will attenuate or amplify. The results of this effort are also presented in Section IV.

B. Review of Previous Spray Combustion Models

A review of the various analyses proposed for describing the phenomenon of spray combustion in liquid propellant rocket motors indicates that all are built upon a foundation of assumptions. The areas of concern included in these assumptions can be categorically listed as follows;

1. Influence of chemical kinetics
2. Vaporization rate limited combustion
3. Injection boundary conditions
4. Relative propellant vaporization rates
5. The effects of forced convection
6. Chamber pressure variation
7. Droplet shattering
8. Spray distributions

Several investigations have treated the liquid rocket combustion problem using the assumption that the combustion rate is controlled by chemical kinetics. Miesse[1] considered a single chemical reaction of first order and assumed a one-dimensional, isothermal system. In addition it was assumed that the propellant vaporization could be described as a linear regression rate of the droplet surface area in the absence of convection.

The implications of the results of Miesse's analysis is that there is little or no difference between spray combustion or premixed gas combustion. This infers that chemical kinetics is the combustion rate limiting process.

The above conclusions conflict with those of Bittker and Brokaw[2] who calculated maximum chemical space heating rates in combustion processes. The results represent the theoretical maximum possible heat release rate to be expected from a unit volume of a reacting fuel-oxidant mixture. Comparison of the results with estimated heat release rates for the same propellants in experimental rocket engines shows that the latter are several orders of magnitude less than the calculated maximum chemical rate for a given propellant. These results indicate that the combustion process in conventional liquid rockets is much less rapid than it would be if limited by chemical kinetics. Therefore, the great bulk of the work in spray combustion is not influenced by chemical kinetics, but rather concludes that the physical processes of liquid atomization, droplet vaporization and gas phase mixing are the rate controlling parameters.

Most spray combustion analysis,[3-8] are based upon a one-dimensional model, i.e., all variables are functions of distance from the injector face. This implies the assumption that gas phase mixing is instantaneous, since any realistic description of the phenomenon requires at least two dimensions. The processes involved in liquid atomization are indeed not uni-directional, so that droplet vaporization must be considered as the dominant process in the rate controlling mechanism. Since most spray combustion models are similar in the manner in which they treat the vaporization limited combustion

gas generation rate, it being assumed that the combustion effects from single droplets are additive, a detailed discussion of each model would be redundant. Rather, the various investigations will be discussed as to the manner in which they treat the various assumptions listed previously.

The region near the injector face has long been a problem for both the rocket designer and theoretician. As the propellants flow from the injector in the form of ligaments or jets, external and internal forces tend to cause atomization. Large transverse gradients of oxidizer-fuel ratio are present as well as strong recirculation currents of combustion gases. The boundary conditions generally employed at the injector face are:

1. The gas velocity is zero at the injector face
2. The liquid propellant sprays enter the chamber completely atomized with a well defined droplet size distribution
3. The initial droplet velocities are all equal to the liquid stream injection velocity

Most investigators actually ignore the region adjacent to the injector face by applying the above boundary conditions at the droplet formation or jet break-up distance which can vary from 1 to 4 inches downstream, depending on the type of injector being simulated. A notable exception to the above is the work of Lambiris, (unpublished), which is qualitatively described in Ref. 32. According to this model the combustion chamber is divided into two regions: (1) the injector face region where large gradients exist in the distribution of propellants, and (2) the remaining portion of the chamber and nozzle where the flow of liquids and gases is assumed to be

one-dimensional and uniform. The region adjacent to the injector face is divided into oxidizer rich zones, fuel rich zones, well mixed zones and recirculation zones, where no liquid is present. In addition an attempt is made to account for liquid fragmentation and incomplete atomization. Although it appears that this is a three space dimension transient problem, the author reduces it to a quasi-steady one-dimensional problem by prescribing all of the zones and processes as functions of the axial distance. As yet, the quantitative description of some of the above processes is not known, even under environmental conditions less severe than those encountered in liquid propellant rocket motors. These parameters, therefore, must be studied and deduced from controlled experiments before the validity of the above model can be ascertained.

Some investigations, [9,10], while recognizing that differences in relative vaporization rates exist, have not distinguished between fuel and oxidizer droplets in the analyses. Still other models [3,4,6,7] have found it convenient to assume that the governing equations could be written for the fuel spray alone and that the oxidizer and fuel vaporization rates ratio was constant and equal to the injected mass mixture ratio. This assumption would imply a relatively constant and high combustion gas temperature since all products are generated as the result of adiabatic chemical combination at a near stoichiometric oxidizer-fuel ratio. In addition, this assumption could not properly model a thrust chamber operating above the critical pressure of one of the propellants.

The vaporization rates of both propellant species must be considered in estimating the overall rate of combustion product formation. The relative rates of evaporation of fuel and oxidizer depends on the heat of vaporization, liquid density, thermal capacity, degree of atomization, the critical properties of the propellants and the operating pressure of the thrust chamber.

Some analytical models, [7,10], are based on the assumption of complete entrainment of the droplets in the gas stream. In the absence of relative motion between the gas and liquid droplets, forced convective effects augmenting heat and mass transfer processes are neglected. Another effect of forced convection on a droplet's behavior is drag with resultant changes in droplet ballistics. Realistic empirical relations for Nusselt numbers for heat and mass transfer and drag coefficients are available and have been employed in several investigations, [3,4,6].

As combustion proceeds along the chamber, the stagnation pressure will decrease and the gas velocity will increase. This requires that the static pressure and gas density decrease. For thrust chambers with high contraction ratios the decrease in static pressure is negligible. Many current liquid propellant rocket motors have small contraction ratios such that the static pressure decrease through the chamber may be as high as 20 percent. The decrease in static pressure causes significant increases in vaporization schedules as it decreases the saturation temperature of the propellant and increases its mass diffusion rate. Most spray combustion models [3,6,7,9,10] have employed an assumption of constant pressure

throughout the combustion chamber. Further assuming constant molecular weight for the gases, coupled with the previous assumption of constant relative vaporization rates and hence constant gas temperature, implies that the combustion gas density is constant throughout the chamber. Therefore, most spray combustion models have analyzed the problem of a liquid droplet propagating through a gas with constant physical properties. Burstein et al. [4] have accounted for the pressure variation by the inclusion of an integrated momentum equation and coupling of the droplet ballistic and gas dynamic equations.

Aerodynamic drag forces exerted on the liquid droplets may reach such proportions that droplet deformation and disintegration will eventually take place. Conditions which eventually result in droplet shattering have been studied experimentally [11,12]. One criterion deduced was that breakup can be expected whenever a critical value of the Weber number, (ratio of external shear forces to surface tension forces), is exceeded. After the critical conditions have been imposed on the droplet, shattering may be delayed and non-uniform. Lambiris, et al. [3] have considered droplet shattering to take place for all drops over 50 microns at a prescribed distance from the injector face based upon streak photographs obtained from a transparent rocket motor. Burstein et al. [4] have included droplet shattering in their spray combustion model by replacing the shattered droplets by an equivalent mass of smaller droplets whenever a prescribed critical Weber number was exceeded.

Spray combustion models of necessity, must take into account the

number of droplets that constitute the spray and the distribution of droplet sizes among that number. Extensive reviews of the statistical description of sprays, [13,14], are available. The log-probability equation, the Rosin-Rammler equation and the Nukiyama-Tanasawa equation have been found to fit observed distributions reasonably well. Rather than employ a cumbersome mathematical expression for the spray distribution, all spray combustion models utilize either a single mean droplet size or approximate the spray distribution with a finite number of droplet size groups.

Consideration of the analyses and assumptions discussed previously leads to the following conclusions regarding the development of a more realistic model for spray combustion in a liquid propellant rocket motor.

1. Spray combustion is vaporization rate limited and the effects of chemical kinetics can be neglected.
2. The region near the injector face is not amenable to incorporation in a one-dimensional steady state combustion model.
3. The overall spray combustion model can be based on the summation of the histories of a large number of individual droplets. The accuracy of the final results is more dependent on the correlation between the assumed droplet sizes and the actual spray distribution than any other single factor in the analysis.
4. The effects of forced convection on heat and mass transfer processes must not be neglected. In addition, heat transfer between the gas and liquid must be carefully considered with particular attention focused on variations in droplet temperature

due to heating up periods and cooling due to large mass diffusion rates.

5. Variations in gas pressure and other properties must be included in the analysis of small contraction ratio motors.

6. Provisions should be made in the model for incorporating droplet break-up processes. At the present time the availability of empirical data on droplet shattering in rocket motor environments is sparse.

7. Vaporization of both the fuel and oxidizer must be analyzed. The implications of incorporating this item in a spray combustion model are worthy of discussion. The energy added to the gas stream is a function of the ratio of oxidizer to fuel evaporated at the volume element being considered. The local gas properties, (specific heat, enthalpy, temperature, molecular weight), are functions of the ratio of oxidizer to fuel evaporated between the injector and the volume element being considered. These parameters are predicted as the results of thermodynamic equilibrium calculations. For a particular propellant combination wherein one specie vaporizes much more readily than the other, (either due to high volatility or operation above the critical pressure), the gas temperatures at the upstream end of the chamber will be considerably lower than those calculated for combustion at the injected O/F ratio.

A model of bi-propellant spray combustion (considering both fuel

and oxidizer evaporation) accounting for all of the assumptions enumerated above is developed in Section II.

C. Review of Previous Experimental Work

This section is concerned with a review of experimental investigations of combustion instability in liquid propellant rocket motors with particular emphasis on diagnostic studies of wave propagation phenomena. Instability in the liquid propellant rocket system manifests itself as uncontrolled cyclic variations of pressure in the feed system and combustion chamber concurrently or in the combustion chamber alone, depending upon the frequency of oscillations. High order frequencies, greater than 1000 cps are almost always confined to the combustion chamber, and oscillations having frequencies below 600 cps reflect simultaneous variations in the feed system.

Initial efforts in analyzing low frequency instability were reported by Gunder and Friant,[15]. Subsequent work by Summerfield,[16], Crocco,[17], Barrère and Moutet,[18], and others,[19,20], have shown that the low frequency instabilities may be related to a difference in phase between the variations of the chamber pressure and the burnt flow of propellant produced by combustion. This phase difference results from the time lag between injection and combustion of a given propellant particle. This ignition delay was at first considered to be constant,[15,16], but subsequently was related to the fluctuations of the pressure in the chamber,[17]. The theoretical analysis predicted stability could be improved by increases in the length of the feed line, the propellant velocity in the feed line, the pressure drop across the injector and the ratio of chamber volume to nozzle area.

In an exhaustive experimental program, Barrère and Moutet,[18] corroborated these results and found that the frequency of oscillations increase with chamber pressure, decrease with characteristic length, (ratio of chamber volume to nozzle area), and increase with injection pressure drop. In general, low frequency instabilities are ascribed to interactions between the processes in the combustion chamber and the propellant feed system. It is sufficiently understood so that it is comparitively easy to avoid or cure.

High frequency oscillatory combustion differs from the low frequency type in many respects besides the magnitude of the observed frequency of combustion chamber pressure fluctuations. The high frequency oscillations, or "screaming", are characterized by high amplitude fluctuations of the chamber pressure only, and are not accompanied by pulsations in the propellant flow. In addition, screaming results in a significant increase in the amount of heat transferred from the combustion gases to the walls of the chamber, whereas low frequency instability does not alter the heat transfer rates.

Screaming has been attributed to combustion-reinforced pressure waves passing through the chamber and reflecting from the chamber surfaces to trigger succeeding combustion surges. The frequency of such waves would therefore be governed by the velocity of wave propagation and the geometry of the chamber. Although the equations of pure acoustics are insufficient to accurately describe the wave propagation phenomena in an inhomogeneous, accelerating, chemically reacting flow, the oscillation

frequencies may be expected to correspond roughly to one of several simple acoustical modes of the chamber.

Levine and Lawhead, [21], showed that liquid propellant rocket motors are indeed capable of sustaining organ pipe type oscillations. Heidmann and Priem, [22], made pyrometry studies with a 2 inch diameter, 27 inch long chamber firing liquid oxygen and hydrocarbon fuel. They observed the two lowest modes of an organ pipe oscillation for a closed-end, open-end system. The most convincing proof of the existence of acoustic type waves in the chamber was obtained by Berman and Logan, [23], Berman and Cheney, [24], and the staff at the California Institute of Technology's Jet Propulsion Laboratory, [25]. These groups have published excellent streak photographs of the longitudinal waves in rocket motors. Their experimental information established definitely that the vibrations of the combustion gases occurring during oscillatory combustion correspond to the propagation of finite pressure disturbances in the combustion chamber. Berman and his co-workers found that the pressure waves, which appear to originate near the injector in the combustion zone, are initially of almost perfect sinusoidal shape. After passing a few times back and forth through the chamber, the waves may become shocks with an attendant increase in peak to peak amplitude. It is also observed that, once the pressure waves travelling back and forth in the chamber assume their saw-toothed shape, the vibrations of the combustion gases are self sustained and of constant amplitude and frequency. Thus the vibrations must be maintained by a feedback mechanism caused by the interaction between waves and reactions in the chamber, since

without energy addition, waves of finite amplitude would be attenuated by viscous and thermal dissipation. Berman and Logan attribute the oscillation reinforcement to intermittent ignition of the accumulated propellants near the injector by the compressive impulse of each longitudinal wave. They also hypothesize that strong waves ignite droplets which burn in the wake of the pressure wave as it propagates through the chamber.

Ellis et al.,[25] also found that the organ-pipe oscillations were of a travelling wave rather than a standing wave character. A strong pulse started at the injector, traveled the length of the chamber, was reflected and traveled back to the head end. During the cycle, the amplitude of the pulse decreased continuously. The weak pulse, upon reaching the head end, triggered a new-strong pulse.

Crocco and his co-workers[26,27] have related the stability of the rocket engine to the exponent of the pressure sensitivity of the combustion reaction. They assume that combustion time is inversely proportional to a power "n" of the chamber pressure. The value of "n" necessary to drive an oscillation then indicates the likelihood of that oscillation; the higher the value of "n", the less likely that the oscillation can set up. The mathematical model chosen by Crocco is based on the linearization of the equations of motion for small perturbations. Implicit in the model is the assumption that the Mach number in the chamber is much less than unity. The experimental verification of the theory,[27], was obtained with rocket motors that had high contraction ratios and hence low Mach numbers. However, the existence of phenomena involving strong waves of large amplitude,[23-25,28],

indicates that the vibrations of the chamber gases which take place during oscillatory combustion are non-linear and, therefore, cannot be described accurately by means of linearized equations.

Recent experimental efforts have been concerned primarily with the gross effects of variations in injector configuration, nozzle geometry, propellant mixture ratio, etc., on the limits of high frequency combustion instability,[29-31] Basic investigations on the interactions of controlled pressure disturbances with well defined steady state rocket motor flow fields have been ignored. The experimental portion of the present investigation, detailed in Section IV, is concerned with first determining the pressure, velocity and combusted gas distributions in a liquid bi-propellant rocket motor and then investigating the interaction of a controlled pressure wave with this field.

SECTION II

STEADY STATE BIPROPELLANT SPRAY COMBUSTION MODEL

A. Description of the Phenomena

The steady state transformation of a pair of injected liquid propellants into hot combustion gases in a rocket engine is the primary concern of this section. An excellent qualitative discussion of the various processes involved has been published in Ref. 32. In describing the overall transformation it is best to separate the various processes involved in order to determine the rate-controlling factors.

The generation of hot combustion gases begins with the injection of liquid propellants into a thrust chamber. Depending on the type of injector employed, e.g., like on like impinging, unlike impinging or showerhead, spray fans are formed, inside which the propellant streams break into ligaments, and eventually into small droplets. The system of injected streams, liquid ligaments and droplets is entirely enveloped by hot combustion gases. Heat is transferred from the combustion gases to the liquid propellants, thereby increasing their temperature and causing them to vaporize. The gases also exert aerodynamic forces on the liquid fragments increasing their rates of atomization, vaporization, and altering their axial velocities. In addition, it has been shown,[33], that the gases near the injector are in a dissociated state and are reactive with either fuel or oxidizer vapors.

The nature of the injection process results in large spatial variations

of the distribution and fragmentation of the liquid propellants. Therefore, gradients in gas temperature, composition and pressure will exist in the region near the injector. However, slightly downstream of the injector face, interactions between the liquids and gases will tend to equalize the gradients, so that for steady state conditions a unique distribution of propellant weight fractions, droplet size, and gas properties can be assumed. The resulting distribution is primarily imposed by the geometrical shape of the injector and its operating conditions. The preceding discussion implies that a well mixed, one-dimensional combustion gas and propellant mixture cannot be assumed near the injector face. Rather, some jet break-up or droplet formation distance must be assumed, and spray combustion calculations commenced at that point. The magnitude of the jet break-up distance is generally between 1 and 4 inches, depending upon the type of injector employed.

In the region downstream of the droplet formation distance, the large transverse concentration gradients diminish until they become negligible. In this region the injected liquid jets have been completely atomized into well defined droplet distributions so that the liquid oxidizer-fuel ratio is nearly constant over the entire chamber cross section. In addition, the evolved gases are uniform over a given chamber cross sectional area.

The volumetric flow rate of the liquid propellants is very small compared to that of the gases so that droplet collisions and interference can be neglected. Heat is transferred from the hot gases to the propellants

causing them to vaporize, interdiffuse, and subsequently react with the surrounding gases. The resulting accelerating gaseous flow imposes aerodynamic forces on the droplets which causes deformation of their shape. Eventually, the induced shearing forces may overcome the droplets cohesive force breaking them into smaller fragments. This phenomenon is referred to as droplet shattering or secondary atomization. When all of the droplets have been completely vaporized the transformation process is complete, and the subsequent flow problem is one of gas dynamics.

As a result of the preceding remarks it appears that the transformation of liquid propellants into hot combustion gases is rate controlled by the heat and mass transfer processes under forced convection conditions. For some propellant combinations, notably the hypergolics, liquid phase chemical reactions can become a controlling factor and should be considered where applicable.

B. Theoretical Analysis

The model of spray combustion in a rocket motor is best divided into two parts which are strongly coupled. The first part concerns itself with the liquid propellant droplets, while the second part describes the combustion gas dynamics. Coupling is obtained by virtue of mass transformation, energy interchange and drag forces. Therefore, a set of equations will be derived that describe the fuel droplet history and a similar set will be used to describe the oxidizer droplet history. A third set of equations will be required to model the combustion gas flow field. The entire system

of equations will then be solved simultaneously with appropriate boundary conditions.

Liquid Droplet Model

The heating and vaporization of fuel or oxidizer is assumed to begin at the point in the chamber at which liquid droplets are formed. At this location the injected propellant streams are represented by a droplet size distribution. The particular distribution employed is dependent upon the type of injector and empirical data. The subsequent evaporation of the oxidizer and fuel sprays is then represented by a summation of the evaporation of a finite number of representative droplets. It is further assumed that mixing and reaction rates are fast and that reacted products are formed as soon as the propellants are vaporized.

A schematic model of fuel or oxidant drops vaporizing in a rocket engine is shown in Fig. 2.1. The liquid droplet is shown at position x in the chamber corresponding to time t and an increment later corresponding to $x+\Delta x$ and $t+\Delta t$. In the interval, the drop velocity changes by Δv and the gas velocity by Δu. While the droplet travels through the increment heat is transferred to its surface at a rate q_v and mass leaves the surface at a rate $\dot{w}$. Therefore, the droplet mass and radius change by an amount Δm and Δr respectively. In addition, the droplet temperature, which is assumed uniform throughout the drop, changes by an amount ΔT_ℓ.

The entire vaporization process is divided into sufficiently small increments so that steady-state mass, momentum, and heat transfer equations are applicable within each interval. One dimensional steady-state flow is

assumed for both the droplet and bulk gas models. The droplet density, surface tension, viscosity, specific heat, vapor pressure and heat of vaporization are taken as functions of temperature. The heat of reaction of fuel and oxidizer is evaluated at the ratio of oxidizer to fuel evaporated within the interval under consideration. Properties of the bulk gas, i.e., molecular weight, specific heat, enthalpy, and viscosity are evaluated as functions of temperature and the ratio of oxidizer to fuel evaporated between the injector and point of interest.

Mass Transfer

Following the correlation of Ranz and Marshall,[36], thermal diffusion is neglected and mass transfer results from a driving force in the direction of film diffusion. The following relationship is obtained:

$$Nu_w = \frac{2K_g R \bar{T} r}{D_v M_v} = 2 + 0.6\,(Sc)^{1/3}(Re)^{1/2} \qquad (1)$$

where Nu_w = Nusselt number for mass transfer

K_g = mass transfer coefficient, lbm/lbf-sec

R = Universal gas constant, ft lbf/lbm-mole ^{o}R

$\bar{T}$ = film temperature, ^{o}R; $\frac{Tgas + Tdrop}{2}$

r = drop radius, ft

M_v = molecular weight of drop vapor, lbm/lbm-mole

D_v = diffusivity, ft^2/sec

Sc = Schmidt number

Re = Reynolds number

The diffusivity, D_v, can be obtained from empirical correlations[6], or from equations given in Bird, et al.,[37]. The latter method is used in this work:

$$D_v = \frac{(p_{ca} p_{cb})^{1/3} (T_{ca} T_{cb})^{5/12}}{\left(\frac{M_a M_b}{M_a + M_b}\right)^{1/2}} \frac{a}{p} T_R^{\,b} \qquad (2)$$

where p_{ca} = critical pressure of droplet substance, lbf/ft^2

p_{cb} = average critical pressure of film constituents, lbf/ft^2

T_{ca} = critical temperature of droplet substance, ^oR

T_{cb} = average critical temperature of film constituents, ^oR

p = static gas pressure, lbf/ft^2

$a = 3.2\ 10^{-6}$

$b = 1.823$

M_a = molecular weight of droplet, lbm/lbm-mole

M_b = average molecular weight of film constituents, lbm/lbm-mole

and

$$T_R = \frac{\overline{T}}{(T_{ca} T_{cb})^{1/2}}$$

The rate of mass diffusion from the droplet is then calculated from

$$\dot{w} = K_g A_d p_v \alpha \qquad (3)$$

where $\dot{w}$ = rate of mass diffusion, lbm/sec

A_d = drop surface area, ft^2

p_v = drop vapor pressure, lbf/ft^2

and

$$\alpha = \frac{p}{p_v} \ln \frac{p}{p-p_v}$$

α is an engineering correction factor which converts the equimolal diffusion coefficient, K_g, (which considers diffusion from the gas to the droplet to be equal to diffusion from the vaporizing material to the surroundings) to a unidirectional diffusion coefficient which only considers diffusion from the droplet to the environment.

Heat Transfer

The heat transfer to the drop analysis is that given in Refs. 4 and 6. The total heat transferred from the gases q_t, goes to heat the liquid drop q_ℓ, vaporize the diffusing vapor q_λ, and heat the diffusing vapor q_{sh}. The heat arriving at the droplet surface q_v, equals the sum of q_ℓ and q_λ and is given by:

$$q_v = hA_d(T_g - T_\ell)\, Z \qquad (4)$$

where h = convective heat transfer coefficient, BTU/ft^2-sec-^{o}F

T_g = gas temperature, ^{o}R

T_ℓ = droplet temperature, ^{o}R

and

$$Z = \frac{\beta}{e^\beta - 1} \qquad \beta = \frac{\dot{w} c_{pv}}{hA_d}$$

In Eq. (4), Z represents the ratio of the heat that is conducted to the droplet surface with convection and mass transfer, to the heat transfer with pure convection and no mass transfer.

The film coefficient is determined from the correlation of Ranz

and Marshall,[36]:

$$Nu_h = \frac{2hr}{k_v} = 2+0.6\,(Pr)^{1/3}(Re)^{1/2} \qquad (5)$$

where Nu_h = Nusselt number for heat transfer

k_v = mean film conductivity, BTU/ft-sec-^oF

Pr = Prandtl number, vapor film $\frac{c_p \mu}{k_v}$

Re = Reynolds number, $\frac{2r|u-v|\rho}{\mu}$

u = gas velocity, ft/sec

v = drop velocity, ft/sec

ρ = gas density, lbm/ft^3

All transport properties, dimensionless numbers and density for the gas are evaluated at the average film temperature, $\overline{T}$.

Momentum Transfer

Aerodynamic drag is the mechanism by which momentum is transferred between the droplets and gaseous environment. The drag forces will either decelerate or accelerate the droplets as the velocity of the drop approaches that of the surrounding gases. For a spherical drop immersed in a moving fluid the drag force F_d is given by:

$$F_d = \frac{m_d}{g}\frac{dv}{dt} = C_D \frac{A_d \rho}{g}\frac{(u-v)|u-v|}{2} \qquad (6)$$

where the drag coefficient, C_D, is given as,[38]

$$C_D = 27\,(Re)^{-0.84} \qquad (7)$$

Changes in Droplet Properties

Changes in droplet properties, $(\Delta r, \Delta v, \Delta T_\ell)$, can be calculated from the set of preceding equations assuming one knows the instantaneous drop radius, drop velocity, drop temperature and state of the surrounding gaseous environment. The change in drop radius with time is determined from the mass transfer equations along with the continuity equation for the liquid drop;

$$\frac{d}{dt}\left(\rho_\ell \frac{4}{3}\pi r^3\right) = -\dot{w} \tag{8}$$

or

$$\frac{dr}{dt} = -\frac{\dot{w}}{\rho_\ell A_d} - \frac{r}{3\rho_\ell}\left(\frac{d\rho_\ell}{dT_\ell}\right)\frac{dT_\ell}{dt} \tag{9}$$

The change in drop temperature with time is determined from an energy balance at the droplet surface;

$$q_v = q_\ell + q_\lambda$$

where

$$q_\lambda = \dot{w}\lambda$$

and q_ℓ is the heat that changes the drop temperature. q_v and $\dot{w}$ are determined from Eqs. (4) and (3) respectively, while λ, the heat of vaporization is a function of the drop temperature. By assuming that the droplet temperature is uniform, the time derivative of the drop temperature is related to the heat transfer as follows;

$$q_\ell = mc_{p\ell}\frac{dT_\ell}{dt}$$

or

$$\frac{dT_\ell}{dt} = \frac{1}{mc_{p\ell}}\left(q_v - \dot{w}\lambda\right) \tag{10}$$

Examination of Eq. (10) shows that if the heat transfer rate q_v is greater than the rate at which energy is carried away by the vaporizing liquid $\dot{w}\lambda$, the droplet temperature increases. Referring to Eq. (9) it can be seen that it is possible for the drop radius to increase. This generally occurs during the initial stages of evaporation when q_v is large, $\dot{w}$ is small and $\frac{dT_\ell}{dt}$ is positive. As the rate of evaporation increases, $\dot{w}\lambda$ eventually exceeds q_v and the drop temperature decreases. This in turn causes a decrease in the drop vapor pressure which subsequently decreases the evaporation rate, Eq. (3). Therefore, a balance is reached wherein the heat transfer rate equals the heat carried away by the vapor and the drop temperature remains constant.

The change in drop velocity is obtained from Eqs. (6) and (7) and is given by:

$$\frac{dv}{dt} = \frac{3}{8} C_D \frac{\rho}{\rho_\ell} \frac{|u-v|(u-v)}{r} \tag{11}$$

The previous system of equations are used for both fuel drop histories and oxidizer drop histories with the substitution of appropriate functions for the physical properties of the droplet. The equations are solved for each of the n sizes of fuel drops and m sizes of oxidizer drops that are assumed to represent the injected spray distribution of each propellant. The average critical properties of the film constituents referred to in the expression for the diffusivity, D_v, Eq. (2), are taken as the average for CO_2 and H_2O for the JP-5A-liquid oxygen system discussed in the analysis. The dimensionless quantities, Re, Sc, Pr and the gas density are evaluated at the film

temperature $\overline{T}$, defined previously.

Droplet shattering or secondary atomization can occur whenever the drag forces exceed the restoring forces due to surface tension. Accordingly, a Weber number criteria has been included in the analysis which replaces the droplet by an arbitrary number of smaller drops of equal total mass whenever a preselected value of the Weber number is exceeded. The Weber number is defined as

$$We = \frac{2r(u-v)^2\rho}{g_c\sigma_\ell}$$

where ρ = gas density, lbm/ft^3

σ_ℓ = surface tension lbf/ft

g_c = universal gravitational constant, 32.2.

Gas Dynamic Model

The gas dynamic model consists of an equation of state, three conservation equations and a system of chemical equilibrium equations. The equilibrium equations for the JP-5A-liquid oxygen system are solved initially to produce a table of enthalpy, molecular weight and specific heat as functions of temperature and combusted oxidizer-fuel ratio in the range of pressure of interest.

The equation of state is assumed to be:

$$p = \frac{\rho R T}{M} \tag{12}$$

The steady state one-dimensional continuity equation is given by:

$$\frac{d}{dx}(\rho u A) = \frac{d\varphi}{dx} \tag{13}$$

where A = chamber cross sectional area, ft^2

φ = rate of flow of gases, lbm/sec

The integrated continuity equation is simply:

$$(\rho u A)_x = (\varphi)_x \tag{14}$$

The rate of gas flow φ is obtained from the droplet model by adding the evaporation of all of the fuel and oxidizer drops, as follows;

$$\varphi_x = \sum_{p=1}^{n+m} \int_0^x \frac{\dot{w}_p N_p}{v_p} \, dx \tag{15}$$

where $p = 1 - - - - - - - n$ represents fuel drops,

$p = (n+1) - - - - (n+m)$ represents oxidizer drops,

and subscript p indicates a particular size (class) fuel or oxidizer droplet. N_p represents the number of drops of the p^{th} class passing location x per second. v_p is their velocity in feet per second. $\dot{w}_p$ is obtained from Eq. (3).

The steady state one-dimensional momentum equation is

$$\frac{1}{\rho}\frac{dp}{dx} = -\frac{u}{g_c}\frac{du}{dx} + F - \frac{1}{\rho A g_c}\frac{d\varphi}{dx}(u-\bar{v}) \tag{16}$$

where F is the force per pound of gas due to drag between the gas and the droplets and the last term on the right hand side represents the force due to the momentum increase of the gaseous mass generated within the control volume. The drop velocity $\bar{v}$ is taken as the average of the velocities of the various size fuel and oxidizer drops. The average is weighted according to the amount of mass evaporated from each class within the interval. The force F is given by:

$$-F = \sum_{p=1}^{n+m} f_p = \frac{1}{\rho A} (BFOR) \tag{17}$$

where the force on an individual drop class is:

$$f_p = \frac{m_p}{\rho A g_c} \left(\frac{dv_p}{dt}\right) N_D \tag{18}$$

and m_p is the mass of the p^{th} size (class) drop.

Integrating the momentum equation yields;

$$p_{x+\Delta x} = p_x - \frac{\rho_x u_{x+\Delta x}}{g_c} (u_{x+\Delta x} - u_x) - \frac{(BFOR)_{x+\Delta x}}{A} \Delta x - \frac{(u-\bar{v})_{x+\Delta x}}{A g_c} \left(\frac{d\varphi}{dx}\right) \Delta x \tag{19}$$

For the purpose of the above integration the gas density is assumed to be constant.

The steady state energy equation for a control volume is

$$\frac{d}{dx}\left[\varphi\left(h + \frac{u^2}{2}\right)\right] = Q - W + h_{st}\frac{d\varphi}{dx} \tag{20}$$

where the left hand side of Eq. (20) represents the change in the energy carried by the gas across the control surfaces and

Q = net heat transfer to the gas within the control volume, BTU/ft-sec

W = work done by the gas within the control volume, BTU/ft-sec

h_{st} = stagnation enthalpy of the propellants evaporated within the control volume, BTU/lbm

The last term on the right hand side of Eq. (20) represents the energy added to the bulk gas flow by the liquid propellants evaporated within the control volume. The net heat transfer to the gas Q is related to the heat transfer to the drop q_v, defined by Eq. (4).

$$Q = -\sum_{p=1}^{n+m}\left(\frac{q_{vp}N_p}{v_p}\right) = -\,BHET \tag{21}$$

where the summation is carried out for all of the classes of fuel ($p = 1\text{-------}n$) and oxidizer ($p = (n+1)\text{ -------}(n+m)$) drops. The work done by the gas in accelerating the drops is given by

$$W = \frac{\rho A}{J}\sum_{p=1}^{n+m}(f_p v_p) = \frac{1}{J}(BFOV) \tag{22}$$

where the summation is again taken over the fuel and oxidizer drops.

The integrated energy equation becomes:

$$h_{x+\Delta x} = \frac{1}{\varphi_{x+\Delta x}}\left[\varphi_x\left(h_x + \frac{u_x^2}{2g_c J}\right) + \left(-(BHET)_{x+\Delta x} - \left(\frac{BFOV}{J}\right)_{x+\Delta x} + h_{st}\,\frac{\partial\varphi}{\partial x}\right)\Delta x\right] - \frac{u_{x+\Delta x}^2}{2g_c J} \tag{23}$$

The gas enthalpy h, is a function of gas temperature and the O/F ratio of the combustion gases. This latter quantity is defined as the ratio of the decrease in liquid oxidizer flow between the injector and point x to the decrease in liquid fuel flow between the injector and point x. It is determined from the results of the liquid drop calculations as follows;

$$(O/F)_x = \frac{(\dot{m}_o)_{inj} - \sum_{p=n+1}^{n+m}(m_p N_p)_x}{(\dot{m}_f)_{inj} - \sum_{p=1}^{n}(m_p N_p)_x} \tag{24}$$

where $\dot{m}_o$ and $\dot{m}_f$ are the injected flow rates of oxidizer and fuel, and the terms under the summation sign are evaluated at x. The molecular weight

of the combustion gases, which appears in Eq. (12) is also a function of gas temperature and the O/F ratio of the combustion gases. The stagnation enthalpy of the evaporated propellants, h_{st}, is dependent upon the drop temperature, drop velocity and ratio of oxidizer to fuel evaporated between x and $x+\Delta x$. The method of calculating the stagnation enthalpy or energy addition from the evaporated propellants is discussed in detail in a subsequent paragraph under the Method of Computation.

The system of equations that must be solved consists of Eqs. (9), (10) and (11) written in finite difference form together with Eqs. (12), (14), (19), and (23). The first three equations must of course be solved for each of the classes of both fuel and oxidizer drops.

Method of Computation

The general scheme for solution of the previous system of equations is to calculate fuel and oxidizer droplet histories based upon an assumed gas dynamic flow field. The hydrodynamic equations of the combustion gases are then solved based upon results from the drop calculations. Iteration between the two systems of coupled equations is performed until convergence is obtained. The problem has been programmed for solution on an IBM 7040.

The Eqs., (9, 10, 11) that describe the history, (T_ℓ, v, r) of a fuel or oxidizer drop are ordinary differential equations that can be solved if initial drop conditions and values of gas temperature, gas pressure, gas velocity and combustion gas O/F ratio are known at all points. The required droplet

initial conditions are; injected mass flow rate of oxidizer, injected mass flow rate of fuel, number of different size drops that represent the fuel or oxidizer droplet distributions, the percentage of total flow of fuel or oxidizer represented by each of the drop sizes, droplet formation distances for each of the drop sizes and initial values of temperature, radius, and velocity for each of the drop sizes. The last four parameters may have different values for each of the drop sizes considered. With the above conditions specified, equations (9, 10, 11) are solved repeatedly to obtain $T_\ell(x)$, r(x) and v(x) of a single drop for each of the drop sizes. The results are then weighted according to the mass fraction of each drop size and then summed over all drop sizes to obtain the total evaporation, heat transfer from the gas and drag forces between the liquid and gas. Physical properties required to perform the calculations are given in appropriate subroutines containing equations or tabular data with interpolation routines. Liquid propellant properties are evaluated at the local drop temperature. Combustion gas properties are evaluated at the local gas temperature and local combusted gas O/F ratio.

The chamber and converging nozzle were divided into 128 differential segments of equal length. Each of these segments was then divided into 8 subdivisions of equal length. The calculation of changes in droplet properties is then performed throughout 1024 increments. However, if the droplet temperature changes by more than 10°F within any subdivision, the number of subdivisions within that segment is doubled. If the liquid

temperature change still exceeds 10^{o}F the number of subdivisions is again multiplied by two. Reduction of the sub-step length continues until the maximum drop temperature change criteria is met.

Equations (12, 14, 19, 23) represent the system of equations to be solved in the gas dynamic subroutine. The chamber-nozzle configuration is divided into the same number of major segments and minor subdivisions as in the liquid droplet calculations. The chamber cross sectional area as a function of axial distance from the injector is calculated by a subroutine program. The terms that couple the liquid drop equations to the gas equations, i.e., $\varphi(x)$, BHET(x), BFOR(x), BFOV(x) and the combusted gas O/F ratio as a function of x are available from the evaporation subroutine. A separate calculation, employing the four gas system equations is performed in each minor subdivision from x to $x+\Delta x$. The method of solution consists of assuming a value for $\rho(x+\Delta x)$ and solving for $u(x+\Delta x)$ from Eq. (14), $p(x+\Delta x)$ from Eq. (19) and $h(x+\Delta x)$ from Eq. (23). The enthalpy, h, determines the temperature T by use of a function subroutine. The density ρ, corresponding to the last calculated values of pressure and temperature is calculated from the equation of state. The iterative procedure is continued by using the new density to solve for velocity, pressure and temperature. When convergence within the minor subdivision has been achieved, calculations are started in the next subdivision. Calculations proceed to the nozzle throat at which point the pressure, temperature and velocity profiles, p(x), T(x) and u(x) are compared with their values from the preceding iteration. If convergence

has not been attained, the liquid droplet calculations are performed using the last set of gas dynamic properties. This in turn will cause the gas dynamic history to be recalculated, etc. The problem is considered to be solved when convergence is obtained in the gas dynamic profiles.

Properties of the combustion products of JP-5A and liquid oxygen, (enthalpy, molecular weight and specific heat), were obtained from chemical equilibrium calculations by Barber and Hersch.[39] These calculations tabulate the above properties as functions of temperature and O/F ratio at different pressure levels. In the present spray combustion analysis the enthalpy, molecular weight and specific heat are evaluated at the local temperature and combusted gas O/F ratio by means of a double interpolation subroutine. Equilibrium temperature can similarly be obtained by means of a double interpolation of enthalpy and O/F ratio.

The enthalpy of the gaseous combustion products as given in the equilibrium calculations is based on datum enthalpies of -653 BTU/lbm at 536°R for the liquid fuel and -173 BTU/lbm at 162°R for the liquid oxygen. Accordingly, the term in the energy equation (23) which represents the energy addition to the gas stream by the evaporated propellants takes these datum states in account.

$$h_{st} \frac{d\varphi}{dx} = \frac{d\varphi}{dx} \left(\frac{1}{ELOF + 1} \right) \left[-635 - 173\,(ELOF) \right] + BHES \qquad (25)$$

where ELOF represents the ratio of liquid oxidizer to liquid fuel evaporated within the minor subdivision under consideration. The term BHES accounts for the fact that the propellants are not at the datum state prior to reaction

but rather are in a vapor state at an elevated temperature moving with a finite velocity.

$$BHES = \sum_{p=1}^{n+m} \left[\left(\int_{T_d}^{T_{\ell p}} c_{p\ell}\, dT_{\ell p} + \lambda + \frac{v_p^2}{2 g_c J} \right) \frac{\Delta m_p}{\Delta x} N_p \right] \qquad (26)$$

where $p = 1 \text{-------} n$ represents fuel drops

$p = n+1 \text{ ----} n+m$ represents oxidizer drops

T_d = datum temperature, ^{o}R

T_ℓ = temperature of drop, ^{o}R

λ = heat of vaporization, BTU/lbm

Δm_p = reduction in droplet mass within the subdivision Δx

N_p = number of drops per second of the p^{th} class.

The calculation within the brackets is performed for each drop size individually and the summation is then carried out over all the classes of fuel and oxidizer drops.

The integral form of the gas dynamic conservation equations written in finite difference form and the equation of state contain only two independent variables; pressure and temperature. Combustion gas flow rate and O/F ratio are specified by the results of the droplet calculations. Gas density is calculated from the equation of state as a function of pressure, temperature and molecular weight, which in turn is a function of temperature and O/F ratio. Gas velocity is determined from the algebraic form of the continuity equation once the gas density has been calculated. The boundary conditions on the gas dynamic equations are therefore given as:

$$\text{at} \quad x = x_i \qquad p = p_o$$
$$T = T_o$$

where x_i is the point at which gas dynamic calculations commence ; the break-up point. If in addition, the existence of a sonic plane is specified, i.e., Mach number equals one at $x = x_L$, the problem becomes overly constrained since the injected mass flow rate and cross-sectional area have previously been specified. Therefore, the constraint on pressure at x_i is removed and the problem is treated as a split boundary value problem. An initial value of p_o is chosen to start the gas dynamic calculations. If the Mach number becomes unity before the throat or if M is less than one at the throat, the value of p_o is changed and the gas dynamic calculations are repeated. The true boundary conditions for the problem considered here are therefore,

$$x = x_i \qquad T = T_o$$
$$x = x_L \qquad M = 1$$

The above boundary conditions are applicable to systems wherein a chamber-nozzle configuration is specified and the problem is basically one of analysis of spray combustion. The pressure-temperature boundary condition is more appropriate for synthesis of a system where the chamber pressure, chamber diameter and injected mass flow rate are specified and the optimum chamber length and nozzle area variation are to be determined.

C. Results

The previous analysis and its attendant computer program, described in the Appendix, are applied to several sets of boundary conditions. For all cases tested, the thrust chamber geometry is similar to that used in the

experimental program. The chamber is 2 in. in diameter by 1.2 ft. long. The nozzle converges in 0.1 ft. to a throat diameter of 1.64 in. The injection rate of fuel and oxidizer is .63 lbm/sec and 1.701 lbm/sec respectively.

In order to test the computer program and compare it with previous results, it is initially modified to simulate the "proportional evaporation" model of Burstein, et. al.[4] This is accomplished by deleting the oxidizer calculations and determining the combustion gas flow by replacing Eq. 15 with;

$$\varphi_x = \left(\sum_{p=1}^{n} \int_0^x \frac{\dot{w}_p N_p}{v_p} dx \right) \left(1 + (O/F)\ \text{inj.} \right) \qquad (27)$$

where p = 1.... n represents the fuel drops

(O/F) inj = ratio of injected oxidizer to injected fuel.

As a result of Eq. (27) the O/F ratio of the combustion gas is constant throughout the motor. The combustion gas properties data of Reference 4 are substituted for the chemical equilibrium data to be used subsequently with the two-component model. This involves using a frozen composition gas specific heat given as a function of temperature only, and substituting the product of specific heat and temperature for enthalpy in the energy equation. The energy contribution of the evaporated propellants, h_{st}, is modified to be consistent with the change in datum temperature.

The fuel spray is approximated by four different drop size groups which are formed at 0.086 feet from the injector. The boundary condtions on the spray are;

radius(ft.)	concentration	temperature(^{o}R)	velocity(fps)
$1(10^{-4})$	.30	540	142
$2(10^{-4})$	.35	540	142
$3(10^{-4})$	.30	540	142
$4(10^{-4})$	.05	540	142

The boundary conditions on the gas system are;

$x = .086$ ft. $T = 5000\ ^{o}R$

$x = 1.3$ ft. $M = 1.0$

The results of the calculations are shown in Figs. 2.2, 2.3 and 2.4. The drop radius initially increases due to a decrease in density as the drop temperature rises. The distance required to completely vaporize a drop is inversely proportional to the initial drop radius. The liquid temperature rises rapidly until an equilibrium condition is achieved, at which point the evaporation rate becomes a maximum and the drop temperature remains constant. In general, the results are in complete agreement with those of Burstein, et. al., wherein it is stated that the phenomena is one of slowly evaporating drops flowing down a field of gradually increasing velocity until a cooperative effect between the drops and flow field causes acceleration of evaporation.

The computer program is next applied to a two component system as described in Part B of this section. The boundary conditions on the fuel are as given previously. The liquid oxygen boundary conditions are:

radius(ft.)	concentration	temperature(^{o}R)	velocity(fps)
$1(10^{-4})$	.10	160	100
$2(10^{-4})$	.20	160	100
$3(10^{-4})$	.40	160	100
$4(10^{-4})$	.30	160	100

The gas system boundary conditions are:

$x = .086$ ft. $\quad T = 3000^{o}$R

$x = 1.3 \quad M = 1$

The results are shown in Figs. 2.5, 2.6, 2.7 and 2.8. The more rapid heat up and evaporation of the liquid as compared to the results of Burstein, et. al. is not expected. However, the phenomena is readily accounted for when one considers the variation in combustion gas property data used for the two analyses. The frozen composition gas specific heat of Burstein is only 25% of the equilibrium composition specific heat used in the present analysis. Since the heat transfer coefficient to the drops is directly proportional to the specific heat, the bi-propellant spray analysis with equilibrium gas composition results in a more rapid heat-up and vaporization process. In order to compare a proportional evaporation model with a bi-propellant evaporation model, the computer program is again modified to delete the oxidizer calculations. However, the combustion gas data is now taken for equilibrium composition. The results of these calculations are shown in Figs. 2.5 and 2.7. Only the results for the largest size drop considered are presented. The figures

clearly indicate that a bi-propellant evaporation model results in longer heat-up periods and vaporization distances. Moreover, comparison of the results in Figs. 2.2 - 2.4 with the proportional evaporation results in Figs. 2.5 and 2.7 indicate the important effect of gas composition data.

The boundary conditions for the spray drop size distribution used in the previous examples were arbitrary selections. In order to simulate the conditions encountered in the experimental engine described in Section III and Section IV of this report, drop size distributions are determined following the method of Priem, (6). The following spray conditions are obtained:

radius (ft)	concentration
$1.5(10^{-4})$	.30
$4(10^{-4})$	.40
$9(10^{-4})$	.30

This distribution is assumed to approximate both the fuel and oxidizer spray. In addition, the fuel drops are all assumed to have an initial velocity of 142 ft/sec and an initial temperature of 540°R. The oxidizer initial temperature is 160°R and the injection velocity is 100 ft/sec. The boundary conditions on the gas system are:

$x = .086$ ft. $\quad T = 3000^{\circ}$R

$x = 1.3$ ft. $\quad M = 1$

The results of the calculations are shown in Figs. 2.9, 2.10 and 2.11. The effect of using larger drop sizes to approximate the spray distribution is clearly shown by comparison with Figs. 2.5 - 2.8. The liquid oxygen

evaporation is not retarded as much as the fuel evaporation, because of its very high vapor pressure. As a result the O/F ratio of the combustion gas during the initial stages of the chamber is increased from approximately 10 in the previous case to 30 in the present example. This causes the gas temperature to decrease initially, which in turn reduces the heat transfer rate to the drops.

Figure 2.9 shows the variation in drop temperature with distance for the various fuel and oxidizer drop sizes. The effect of the increased gas O/F ratio and reduced gas temperature is evidenced by the long heat-up periods required for the larger fuel drops. Figures 2.10 and 2.11 show the variation in fuel and oxidizer evaporation. The results of the gas system calculations are shown in Fig. 2.12. In addition, a curve of pressure vs. distance is presented for a proportional evaporation model, using equilibrium gas composition and the present spray distribution. The proportional evaporation model, by definition, yields a constant gas O/F ratio of 2.7 and hence a gas temperature profile similar to that shown in Fig. 2.4. Therefore, the subsequent rate of gas evolution and acceleration is more rapid causing the pressure to decrease closer to the injector face.

A series of experimental data points, which fall between the two theoretical curves is also presented in Fig. 2.12. It is expected that experimental pressure points fall below a theoretical curve as a result of heat transfer to the motor walls and frictional effects which are neglected in the analysis. It appears that in terms of the present experimental data, the bipropellant evaporation model predicts an evaporation rate that is too low,

while the proportional evaporation model yields a mass liberation profile that is too high. Referring to Fig. 2.8, the pressure profile obtained with a drop size distribution ranging from $1(10^{-4})$ to $4(10^{-4})$ ft is also below the experimental data points. Note also, that the rate of gas evolution with the smaller size drop distribution, Fig. 2.8, is rapid enough to prevent the decrease in gas temperature that is obtained with the larger drop size distribution, Fig. 2.12.

The previous results indicate the importance of the boundary conditions in terms of proper modeling of a rocket combustor. It is reasonable to assume that a realistic fuel drop size distribution exists that would yield a pressure curve in complete agreement with the data points. It has been stated previously that the drop size distribution of Fig. 2.8 was chosen arbitrarily while the logarithmiconormal distribution of Fig. 2.12 was determined by a method suggested by Priem (6). This latter method uses the results of cold-flow tests of an injector to determine a preliminary mass-median drop radius in terms of a jet diameter and a velocity difference between gas and liquid. The preliminary mass median drop radius is then modified to account for injection into a hot combustor. The method of modification involves a vaporization calculation as proposed by Priem. The assumptions required to determine a mass median drop radius for combustor calculations using Priems analysis are not minor, and as a result, large deviations can occur between experimental and theoretical results.

The boundary condition for gas temperature was selected after several trial computer solutions. The value of $3000^{\circ}R$ corresponds to the average

adiabatic flame temperature for the O/F ratio of the combustion gases in the first interval of calculation. While this value is suspect, it has been shown that when a small size drop distribution is used, Fig. 2.8, the gas temperature does not diminish, indicating that this boundary condition plays a secondary role. However, any future modification of the bi-propellant spray combustion model should include a method to vary the gas temperature at the boundary in accordance with the O/F ratio calculated from the previous iteration. In addition, the effects of recirculation, which would tend to increase the gas temperature in the injector region should be examined for inclusion in the analysis.

A more sophisticated analysis of droplet ballistics might include heat conduction through the droplet, with a subsequent radial temperature distribution. This would cause the vaporization rate to be increased, since the surface temperature and hence the vapor pressure would rise more rapidly. The phenomena would be significantly more predominant for the fuel drops, resulting in a lower gas O/F ratio with a subsequent increase in gas temperature. Therefore the rate of gas evolution would be increased leading to a decrease in the gas pressure.

SECTION III

EXPERIMENTAL FACILITY

The experimental facility has been designed with a view towards obtaining both steady state and wave propagation data in a liquid propellant rocket system. The steady state data is acquired and used for verification of theoretical spray combustion models and as boundary and initial conditions for theoretical and experimental wave propagation studies. Information obtained from wave propagation programs is used to determine the parameters which influence energy coupling to the wave, wave coalescence, and the effect of velocity and pressure gradients on wave attenuation.

The test site complex is composed of a control building, an instrumentation building and a test cell building. The buildings are connected via underground conduits which carry hydraulic lines and electrical cable. The test cell building houses four individual test cells which contain a 500 lbf thrust stand; a 4000 lbf thrust stand; a shock tube for instrumentation calibration and a hydraulic bench for injector, valve and flowmeter calibration. One wall of the test building is composed of sliding doors which are rolled back to afford visual observation from the control building. The control building houses the test console from which all command signals are initiated. Visual observation of the actual firing is accomplished through a blastproof window. The instrumentation building contains all of the recording and peripheral equipment necessary for data acquisition.

The rocket engine system used in this investigation is of 500 lbf

nominal thrust. The propellants are JP-5A and liquid oxygen. The rocket motor itself consists of a stainless steel injector, brass or bearing bronze combustion chamber and a stainless steel nozzle in separable units, as shown in Fig. 3.1. The combustion chamber is made from one or more standardized sections depending upon the desired area schedule and length. The three basic components, i.e., injector, chamber and nozzle are held together by a mechanical clamping arrangement with teflon "o-rings" used to seal the joints. The motor is uncooled, and uses the relatively large mass of metal to absorb the heat transmitted from the gases.

The injector head assembly (Fig. 3.2) consists of an injector plate and a two part manifold. The plate threads into the rear manifold section which is then bolted to the front manifold section. Teflon "o-rings" prevent leakage of fuel and oxidizer. The assembly was designed in a modular fashion in order to facilitate changing injector plate configurations. An injector plate blank is shown in Fig. 3.3. A detailed discussion of the injector plate configurations used in the investigation is presented in Section IV.

The design of the nozzle was influenced by the objectives of the program at the Propulsion Research Laboratory. Among the objectives is an investigation of the nonlinear aspects of wave propagation and combustion instability in liquid propellant rocket motors. In the theoretical analysis of combustion instability, the effect of the Mach number of the gases is highly significant, as indicated in [27]. Briefly stated, if $(1-M^2)$ is approximately unity, the mathematical analysis can be greatly simplified

by means of linearizing assumptions. However, the actual problem is nonlinear,[23, 24, 28], and in practice the Mach numbers at the nozzle entrance are well above those consistent with linearized analyses. As a result of the preceding remarks the nozzle contraction ratio was designed for a nozzle entrance Mach number of 0.45, based on isentropic flow and constant isentropic exponent.

The verification of the nozzle entrance Mach number required a measurement of the total pressure at that point. This entailed designing a probe that can withstand extremely high temperatures and a reactive atmosphere. A water-film cooled graphite probe was developed and employed successfully (Fig. 3.4). The cooling water is sprayed through the probe body into the gas stream at a pressure slightly in excess of the gas pressure. Thus, a film type of cooling is obtained. The mass flow of water into the chamber amounts to less than 1% of the propellant flow. The total pressure probe was used only during the initial steady state tests to verify the design Mach number at the nozzle entrance.

The propellant feed system is pressure fed by a battery of trailer-mounted dry nitrogen cylinders. In addition to tank pressurization, nitrogen gas is used for pneumatic-operated valves, post firing propellant line purging and for operation of pressure receiver-transmitters. The nitrogen is distributed throughout the system by an array of Grove Power-reactor dome type pressure regulators. The outlet pressures of the Grove regulators are controlled by the dome pressure applied to them through individual venting-type hand loader regulators mounted on the test console.

The stainless-steel liquid-oxygen tank, insulated by a layer of polystyrene, is filled prior to test from a low pressure vacuum-insulated 250 gallon storage vessel. The fuel tank is loaded from a 55 gallon drum of JP-5A. In addition to the nitrogen inlet and propellant outlet, each tank is equipped with electrically operated vent valves, pre-set pressure relief valves and tank pressure taps. The nitrogen inlet on the liquid oxygen tank is fitted with a diffuser which directs the pressurizing medium away from the surface of the oxidizer. This is done to prevent agitation and subsequent boiloff of the liquid oxygen and to minimize the likelihood of the diffusion and/or dissolving of the warm nitrogen gas in the cryogenic oxidizer.

Propellant flow to the thrust chamber is controlled through individual propellant valves which are electrically coupled by means of a time delay relay circuit. This procedure allows for control of the lead between oxidizer and fuel injection. Secondary shut-off valves are provided in each of the propellant feed lines as a precaution against malfunction of the main propellant valves. Cavitating venturis are employed in the fuel and oxidizer lines to regulate the propellant flow and eliminate feed line coupling in the event of chamber pressure oscillations. A special igniter has been designed (Fig. 3.5) to insure rapid ignition of the propellants upon injection into the combustion chamber. The igniter consists of a paraffin base end burning propellant grain, a cupron ignition wire and a copper fuse wire. The copper fuse wire which passes across the end of the grain, completes a relay circuit which holds the main propellant valves closed until the fuse wire is burned through by the igniter. The presence of a pilot flame upon injection of

propellants eliminates the possibility of forming the highly explosive substance which results from cold flow mixing of liquid oxygen and JP-5A.

Immediately prior to firing, the liquid oxygen lines and injector manifold are chilled by flushing the cryogenic fluid through the system until liquid flow is indicated. At this point the firing button is depressed which transfers test control to a programmed sequential timer. The following commands are then automatically initiated.

1. Open secondary shut-off valves.
2. Initiate ignition which in turn causes main propellant valves to open in predetermined sequence.
3. Initiate experiments and operate remote auxiliary equipment such as cameras, pumps, etc.
4. Close secondary shut-off valves.
5. Open purge valves which causes gaseous nitrogen to flush propellant lines, injector and chamber of residual propellants.
6. Return all systems to pre-firing condition.

Instrumentation requirements are divided into two categories; monitoring systems and permanent recording systems. Monitoring information, such as tank pressures, injection pressures, chamber pressure and valve position is transmitted to the control building where it is displayed on the test console. Those data that require permanent recording such as propellant flow rates, thrust, chamber pressure gradients and the output of high frequency response pressure transducers used in instability studies are transmitted to the instrumentation facility.

Monitoring of the various pressures is facilitated with the use of Ashcroft pressure receiver-transmitters. These systems sense the desired pressure (0-1000 psig) at its source and uses the information to control the output of a low pressure (0-15 psig) regulator. This signal in turn is transmitted to the test console where it is displayed on a companion pre-calibrated Bourdon gage whose face markings correspond to the source pressure range. Thus, several hundred feet of tubing containing either liquid oxygen, JP-5A or combustion products have been replaced with an equivalent tube length of low pressure gaseous nitrogen.

Instrumentation for acquiring steady state axial pressure gradients, which are used to verify theoretical spray combustion models, categorize various injector configurations and serve as boundary conditions for wave propagation studies, was selected after consideration of several factors, namely; proximity of measurements, expected pressure gradient, accuracy, and cost. Assuming that the pressure was to be measured at eight longitudinal locations, the apparent solution would be to install eight transducers down the length of the chamber. However, each of the considerations above eliminated this technique.

Tests conducted on the shorter length chambers would require a pressure measurement at one inch intervals. The physical size of the diaphragm on a water cooled transducer varies from 1/2 to 1 inch depending on the manufacturer. Therefore, each transducer would actually measure an average pressure over an interval comparable to the center to center distance between pressure taps. In addition, it was expected that the gradient at

certain sections of the motor would be as small as 1 psi in 200 psi between adjacent taps. Using a 500 psi full range transducer, a drift of .1% of full scale in opposite directions by two adjacent transducers would yield zero pressure gradient. Rather than develop a method of compensating for the different drift characteristics of adjacent transducers and associated electronics, it appeared more feasible to develop a technique that employed a single transducer to measure the pressure gradient. In addition, if such a system could be developed the dollar savings to the experimental program would be significant. Rather than employ eight water cooled transducers it would be possible to use a single transducer. It will subsequently be shown that the transducer need not be cooled, resulting in an additional savings. All of the above-mentioned factors lead to the development of a pressure scanner (Fig. 3.6).

The scanner permits a single transducer to travel from pressure tap to pressure tap and consecutively record the pressure at eight different locations in the chamber. The pressure scanner consists of three piston and cylinder units. Units A and B contain facilities for measuring the pressure at eight locations, while unit C is a hydraulic driver. The taps located in the rocket motor are extended to the bulkhead of either unit A or B and then to compartments formed by the inner cylinder or piston, "o" rings, and the outer travelling cylinder which houses a transducer. The reciprocating motion of the outer cylinders, (which enables the transducer to consecutively measure the pressure at adjacent taps in the rocket motor) is governed by a double acting hydraulic piston and cylinder; unit C. Provisions have been

made for varying the speed and length of stroke of the unit, by varying the hydraulic pressure and position of the reversing microswitches which in turn controls the hydraulic fluid feed and vent valves. In addition, a method of continuously recording the exact location of the transducer housing has been developed. This consists of measuring the voltage drop between a moving electrical contact mounted on the transducer housing and a flat copper bar mounted alongside the scanner cylinder. The copper bar is actually an eight stepped voltage divider. The length of each step is equal to the length of the compartments in the scanner cylinder. The distance between steps or sections is equal to the thickness of the "O" rings separating the compartments. Each of the copper bar sections is at a different predetermined voltage. Therefore, by simultaneously recording the output of the transducer and the voltage drop to the moving electrical contact, it is possible to match the pressure magnitude with the location at which it was measured.

The scanner was subsequently modified by replacing the hydraulic driving force with a variable speed AC motor coupled to a slider crank mechanism, (Fig. 3. 7). More recently a pressure scanning system, manufactured by the Scanivalve Co., San Diego, California has been installed. The unit is basically a rotary version of the previous scanners, which couples a single transducer to as many as 48 pressure sources through a rotating port.

The output of the transducers is recorded on a recording oscillograph. To record the absolute pressure at each port would result in

reduced resolution. Therefore, only the pressure difference about a fixed point is recorded. Thus 40 psi rather than 200 psi is full-scale deflection on the recorder. The above technique is accomplished by several methods depending upon the type of transducer employed in the scanner. Using a piezoelectric, crystal transducer, the crystal is grounded until the starting transient has been completed. The pressure on the transducer diaphragm at the instant that the ground connection is broken corresponds to zero output. Therefore, the subsequent output of the transducer is proportional to the difference between the pressure being measured and the pressure on the transducer when the ground connection was broken. To determine the absolute pressure at each port, from the records of the gradients, requires a measurement of the absolute pressure at one point in the chamber.

Experimental data on wave shape behavior is obtained with three high frequency-response, flush-mounted, water-cooled pressure transducers (Photocon model no. 352) spaced axially along the chamber. Data are recorded on a frequency modulated magnetic tape recorder-reproducer at 60 ips. The data is played at 1 ips into a recording oscillograph with a paper speed of 25 ips. The final data record thus has an expanded time scale of 1500 ips. Frequency-spectrum analysis of the waves can be accomplished by connecting the output of the tape recorder playback amplifiers to a Panoramic Model LP-1a audio-frequency spectrum analyzer.

A continuous record is made of fuel and oxidizer flow rates during

the test firing. A turbine-type flowmeter is installed in each of the propellant feed lines. The output of the flow transducers is an AC signal whose frequency is proportional to the propellant flow rate. The sinusoidal signal is converted to a pulse signal of equal frequency which is then applied through a stylus to an electrosensitive paper recorder. A 60 cps calibration signal is simutaneously recorded for reference purposes.

SECTION IV

EXPERIMENTAL RESULTS

A. Scope of the Program

An experimental program was conducted in order to obtain steady state and wave propagation data in a liquid propellant rocket system. Steady state experiments serve to examine the validity of spray combustion models as well as provide a source for empirical data on droplet size distributions. In addition, boundary and initial conditions for theoretical and experimental wave propagation studies are obtained. The wave propagation experiments are for the purpose of determing the parameters which influence energy coupling to the wave, wave coalescence, and the effect of velocity and pressure gradients on wave attenuation.

B. Steady State

In the design of liquid propellant rocket combustors it is desired to have complete burning take place within the combustion chamber. In addition, the liquid and gasdynamic flow fields should be inherently stable. Recent investigations[4, 34] and Section II of this report, resulted in methods to determine the minimum chamber length required to insure complete combustion and the flow fields response to input disturbances. The theoretical analysis predicted mass liberation schedules, gas and droplet velocity histories, and axial pressure histories. It was found that increases in the mass liberation rate are accompanied by attendant increases in the magnitude of the pressure gradient with a corresponding increase in the velocity gradient.

Initial experiments designed to measure axial pressure gradients were in good agreement with the theory for a given set of injection parameters,[4]. In order to obtain correlation, it was necessary to assume a drop size distribution and a droplet formation distance, i.e., the required distance from the injector face for the injected ligaments to form a discrete droplet distribution. The analysis distinctly indicated that energy (mass) liberation gradients can be deduced from pressure gradient measurements. Thus, the chamber length for optimum propellant utilization and thrust production is related to the axial pressure gradient. In a motor whose geometry and propellant mass flow rate are fixed, this gradient is almost entirely dependent on the nature of the injection process.

In addition, the behavior of an input pressure disturbance is dependent on the gasdynamic velocity field through which the disturbance propagates. Thus, the characteristic gradients or signatures produced by various injectors are important parameters in determining the stability or instability of a thrust chamber system. Therefore, an experimental program was initiated in order to determine the pressure gradient characteristics of various injector configurations.

The 500 lbf nominal thrust rocket engine system described in Section III was used for this investigation. The chamber length was varied between 8 and 24 in., although all of the data reported here are for 17 in. chambers except where noted. The chamber and nozzle throat diameters are 2 and 1.65 in., respectively, resulting in a contraction ratio of 1.47. The propellants are JP-5A and liquid oxygen.

All of the injectors used in this investigation contain 16 fuel and 16 oxidizer orifices. The oxidizer orifice is maintained constant at 0.0595 in. diameter, and the fuel orifices are 0.042 in. diameter, except in the S3 showerhead injector, which has m ltisized orifices in order to obtain a greate: distribution of fuel droplet sizes. All impinging injectors are of the unlike impinging stream pattern type, i.e., fuel on oxidizer. Drawings of the various injector configuration are presented in Fig. 4.1. A summary of the above injectors is tabulated in Fig. 4.2.

In order to eliminate the effects of injection velocity on the dro[illegible] ballistics and subsequent evaporation history, the total liquid propel[illegible] mass flow, oxidizer-fuel ratio, and total injection area of both JP[illegible] liquid oxygen are held constant throughout the series of tests present[illegible] reported. JP-5A injection velocity is 85 fps. The average total propellant flow is 2.35 lbm/sec at an O/F ratio of 2.62. A 5% variation from the average flow rate is allowed for inclusion in the test results.

The data for the injectors tested are presented both as pressure vs. axial distance and pressure gradient ($\Delta P/\Delta x$) vs. the average axial distance over which the gradient was computed. It should be noted that later tests included a static pressure tap at the injector face. Consequently, the more recent data presented includes a pressure measurement at this point.

Figure 4.3 shows the data for two showerhead injectors and one impinging injector. The two showerheads both contain four alternating rings of fuel and oxidizer, but differ in fuel orifice diameter. The S2

injector contains sixteen 0.042-in.-diameter orifices whereas the S3 has eight 0.035-in.-, four 0.043-in.-, and four 0.052-in.-diameter orifices. The impinging injector was designed for an impingement distance (x_i) of 0.28 in. The data indicate a much steeper gradient and, hence, a more localized region of evaporation and combustion for the impinging injector than for either of the showerheads. The use of multisized orifices results in a more uniform pressure gradient and hence a spreading of the evaporation and combustion zone.

Data for a radial sheet and tangential sheet impinging injector with the same design impingement distance are shown in Fig. 4.4. Both injectors contain the same number and size of orifices. The tangential sheet injector contains a single ring of doublets, whereas the radial sheet injector contains two rings of doublets. The latter injector increases mixing and atomization of the fuel and oxidizer and results in more rapid utilization of the propellants. Thus, the maximum point on the pressure gradient curve for the radial sheet injector is closer to the injector face than the corresponding point for the tangential sheet injector. This indicates that the main evaporation and combustion zone has been shifted upstream with the I2 injector and implies that a shorter chamber would be required to obtain maximum propellant evaporation.

The results obtained with two additional impinging injectors, each of which contains three impingement distances, are shown in Fig. 4.5 together with the single impingement point, I6 injector. As the impingement point is moved downstream, the degree of mixing decreases and the

evaporation and combustion zone is spread out over a greater axial distance. The high amplitude and thin width of the pressure gradient peak for the I6 injector indicate a zone of high evaporation and combustion approximately 4 in. from the injector face. The injector with impingement distances less than 1 in. has a peak in the pressure gradient curve 6 in. from the injector face, whereas the pressure gradient for the last injector indicates a peak near the nozzle entrance. This implies a high degree of evaporation and gas generation in the downstrean portions of the chamber.

Data have been obtained from three tangential sheet impinging injectors with design impingement points greater than 1 in., Fig. 4.6. Although it cannot be readily determined whether or not impingement takes place at such large distances from the face, the data indicate that, as the intended impingement point is moved downstream, the rate of pressure drop decreases. At the maximum impingement distance tested, the effect of poorer mixing and low propellant utilization is evidenced by the decrease in over-all chamber pressure, despite a somewhat higher propellant flow rate.

The performance with this last injector (I9) is inferior to that obtained with the showerhead S2 injector discussed previously. Aside from the obvious differences between the two injectors, the showerhead contains four alternating rings of fuel and oxidizer, whereas the impinging injector contains a single ring of doublets. It appears then that distribution of the propellant over a greater portion of the chamber cross section enhances

mixing and atomization and promotes the evaporation process. Tests conducted with a two-ring showerhead indicate that a chamber length of 21 in. is required for optimum performance, whereas the four-ring injector only required 14 in.

The three injectors just discussed are equipped with pressure taps in the injector face. The data show that the point of maximum chamber pressure is downstream from the injector face, and the pressure gradient near the face is positive. This is indicated by a negative value of $-(\Delta P/\Delta x)$. This suggests the existence of a recirculation zone or negative velocity gradient in the region near the injector face.

Variations in injector configuration produce variations in axial pressure history in a constant area liquid propellant rocket motor. These pressure variations are due to changes in the mixing and shattering characteristics of different injectors and are concurrent with unique evaporation and mass liberation profiles. For an injector that promotes rapid droplet breakup and intimate mixing of propellants, such as the I6 used in these experiments, the chamber pressure has a maximum gradient close to the injector face with a correspondingly high gas acceleration. This action exerts additional gasdynamic effects on the unconsumed droplets, enhancing propellant consumption.

Since the attenuation or amplification of a pressure wave is dependent on the gasdynamic field through which it propagates, the inherent stability of an injector-chamber system is keyed to the pressure-velocity gradient produced.

In addition, the data can be used to establish design criteria for steady-state operation and to predict critical conditions that can exist because of large pressure gradients that result in high heat-transfer rates to the injector face or rocket chamber wall.

C. Wave Propagation Phenomena

Longitudinal wave propagation studies were conducted in a liquid propellant rocket motor in order to observe wave deformation phenomena and to define the parameters that determine whether an input disturbance will attenuate or amplify. Since combustion instability is a measure of the relative amounts of energy accumulation in a cavity in contradistinction to the energy dissipation from the cavity, the mechanisms that allow such behavior should be analyzed in detail. Particular emphasis must be placed upon the interaction of pressure waves and the fluid dynamic field in accordance with remarks made in the introduction, which are repeated here for completeness.

Energy coupling between the propagating wave and the combustion process is dependent upon the relative magnitudes of characteristic times associated with the source and sink. If the relaxation time of a significant transport process in the conversion of liquid propellants to gaseous products is less than or equal to the wave residence time in a volume element, coupling can occur with resultant unstable operation. The leading edge of a passing wave in a reacting droplet system can increase the rate of evaporation, which couples as a mass source to the trailing edge of the passing wave, thus producing amplification. It can further be seen that,

for a long relaxation time, the mass source can generate wavelets that coalesce as they propagate and ultimately overtake the initial wave that caused the disturbance, again causing amplification. In addition as a wave propagates in a gas, it deforms. The manner and extent of the deformation is dependent on the type of wave, compression or expansion, and the velocity gradient of the gas through which it propagates. Therefore, as a wave moves in a rocket motor it changes its geometry and residence time in a volume element, which in turn affect the nature of the energy or mass coupling to the propagating wave and the ultimate stability of the system.

Initial wave propagation experiments were conducted in a 2-in.-diameter, 500-lbf nominal thrust, JP-5A liquid oxygen rocket motor. The injector is of the shower-head type with 16 fuel and 16 oxidizer orifices, similar to the S2 injector described previously. The data discussed below is obtained with a total propellant flow of 2.37 lbm/sec at an oxidizer-fuel ratio of 2.79. The chamber length is 22.5 in. measured from the injector face to the start of the converging nozzle. The nozzle contraction ratio is 1.47; resulting in a high Mach number profile through the chamber. High frequency-response pressure transducers are flush-mounted in the chamber at 3, 13, and 21 in. from the injector face. Approximately six seconds after startup (steady-state chamber pressure is 165 psia measured 3 in. from the injector face), the wave generator tube diaphragm is ruptured, and a wave propagates into the rocket motor thrust chamber. The wave generator is actually a modified shock driver tube mounted axially through the injector manifold and utilizing the rocket motor combustor as the driven

tube. The transition piece between the shock driver tube and the combustor shapes the input wave. The diaphragm is in a plane parallel to the injector face. Diaphragm rupture is accomplished with a solenoid actuated needle. The wave generator tube driver pressure is 725 psia.

Initially, the diaphragm was mounted within one quarter of an inch of the injector face (Fig. 4.7). The diaphragms were fabricated from stainless steel or brass shim stock in a variety of thickness ranging from 0.005 in. to 0.020 in. The close proximity to the combustion gases often caused failure of the diaphragm during the rocket motor starting transient. At best, the high thermal load imposed resulted in a severely stressed diaphragm which did not petal upon bursting. As a result the input wave was not reproducible. Modifications to the system resulted in moving the diaphragm upstream of the injector, and using a transition piece between the driver tube and injector face to shape the wave. A schematic of the thrust chamber-wave generator system is shown in Fig. 4.8. A typical injector, modified to accept the wave generator transition piece is shown in Fig. 4.9.

The pressure time data of a typical run is shown in Fig. 4.10. The three traces correspond to pressure recordings taken 3, 13, and 21 inches from the injector face. The data separates into two parts. One part consists of the input wave from the wave generator which oscillates axially in the chamber. This is shown in the upper part of the figure. The second part is a spontaneous oscillation which occurs soon after the first wave group attenuates. This is shown in the lower part of the picture. These latter waves are discussed first.

The output of all transducers indicates a periodic disturbance propagating longitudinally in the thrust chamber (Fig. 4.10b). The wave is initiated at the injector face, propagates downstream, reflects from the sonic plane of the nozzle throat, and propagates upstream. At the injector face, the wave is reflected once more and travels toward the nozzle. The period of the disturbance (defined as the time between two successive waves traveling in the same direction) is 1.37 msec. The amplitude of the over-pressure is approximately 100 psi with a rise time of 0.05 msec. The pressure decays behind each incident wave to the steady-state chamber pressure before the time of arrival of the reflected wave. The frequency of the disturbance is 730 cps. With a chamber length, measured from the injector face to the sonic plane, equal to 2 ft, the equivalent wavelength would appear to be 4 ft. Therefore, the expected wave velocity relative to the gas would be 2920 fps. This is below the expected speed of sound for liquid oxygen-JP-5A combustion products and is less than the propagation velocity as determined from the transducer outputs in the following manner.

Velocities of wave propagation relative to a stationary observer are determined by dividing the distance between adjacent transducers by the time required for the wave to travel between transducers. The average value of the upstream and downstream velocities of propagation yields the propagation velocity relative to the gas which, in this case, is 3350 fps. Previous analytical work[4] has shown that the droplet and gas ballistics are consistent with a chamber temperature of 5500°R and a sonic velocity of 3580 fps. Since the temperature and speed of sound are decreasing through the converging

portion of the nozzle, the average sonic velocity relative to the gas would be less than 3580 fps.

The apparent anomaly between the wave velocity as determined from the frequency and equivalent wavelength (2920 fps) and the velocity as determined from the upstream and downstream averaging (3350 fps) can be explained by work done previously at the Polytechnic Institute of Brooklyn,[35]. It was shown that the resonant frequency for a duct containing a gas flow at some finite Mach number M is given by

$$f_r = c(1 - M^2) / 2\ell$$

or the equivalent wavelength is

$$\lambda = [2\ell/(1 - M^2)]$$

where ℓ is the geometrical length of the duct, c is the average wave velocity realtive to the gas, and the duct is assumed to behave as a half-wave resonator. Therefore, the product of the measured frequency and twice the duct length does not yield the average wave velocity, but rather this latter quantity multiplied by a factor of $(1 - M^2)$. For a resonant frequency of 730 cps, a duct length of 2 ft, and an average wave velocity of 3350 fps, the Mach number as determined from the previous equations is 0.367. Since the nozzle entrance Mach number on the motors used in these tests is 0.45, and the duct length includes the convergent portion of the nozzle, the average Mach number as determined from the resonant frequency appears to be reasonable.

The method described above for calculating average wave velocities is also used to calculate average gas velocities which in turn yields the

average Mach number. These calculations are shown in Fig. 4.11. This latter Mach number was compared to values obtained above from frequency measurements and it is seen that the values agree very well, (e.g., 0.367 vs. 0.363). However, these localized measurements bring out another significant feature. If the local sonic velocity is used to indicate the local gas temperature, then, during this type of oscillation, it is seen that the gases in the injector end of the motor are cooler than those at the nozzle end. In other words, there is a variable stagnation temperature in the chamber due to different evaporation rates of the propellants and consequent variable O/F ratio during combustion. In any detailed wave analysis, both the fuel and droplet ballistics must be considered to give accurate wave behavior.

It is obvious that for low Mach numbers and large contraction ratios the effect on the resonant frequency is small, but as the Mach number increases, the reduction in natural or resonant frequency increases. If one has a beforehand knowledge of the wave velocity relative to the gas, say 3350 fps, and uses simple acoustic theory (M = 0), the resonant frequency for a 2-ft chamber would be 840 cps. As the Mach number is increased to 0.367, a 13% decrease in resonant frequency is noted.

An important conclusion to be derived from the foregoing discussion is that acoustic theories will not give accurate quantitative results of the analysis of wave oscillations in rocket motors, especially those having small contraction ratios with resultant high Mach number profiles.

Now consider the initial part of the wave train, (Fig. 4.10a). A

diagram showing the time of arrival of the wave at the various transducer locations is shown in Fig. 4.12, along with the tabulation of various parameters. The initial wave is generated with a wave slope of 32 psi/in. As the wave propagates through the combustion zone, i.e., between 3 and 10 in. from the injector face, where large longitudinal pressure and velocity gradients are present, it is seen to broaden. Actual transducer outputs from the 3- and 13-in. locations reveal a train of secondary wavelets following behind the initial input wave (Fig. 4.10a). The pressure history at the 21-in. transducer indicates that all of the secondary waves have coalesced with the initial wave to form a single steepening wave. The secondary wavelets have a frequency below that expected for a radial mode and are not characteristic of tangential modes. They are presumed to be due to the interaction of the axial wave with the evaporation zone, resulting in a shattering of drops with an attendant increase in over-all evaporation and combustion rates. Since the steady-state work has previously shown the evaporation and combustion zone to be limited to the first 10 to 12 in. of chamber for the injector currently in use, it would not be expected that combustion waves be produced in the latter half of the chamber. It is interesting to note, however, that the secondary or combustion waves produced in the upstream portion of the chamber coalesce into the incident wave before arrival at the 21-in. transducer.

The wave that is reflected upstream from the nozzle end is initially attenuated. However, as it propagates upstream, it steepens considerably (from 17 to 105 psi/in.). An extrapolation of the wave diagram for the

incident and reflected wave indicates that the equivalent reflecting surface is exactly coincident with the sonic plane at the nozzle throat. Further analysis of the reflected wave reveals that the overpressure, (ΔP), increases from 60 psi to 193 psi. This is measured from a base pressure of about 310 psia. Thus, the new "steady state" pressure increased from 165 to 310 psia and the overpressure from 60 to 193 or by 130 psi. Put another way, the instantaneous chamber pressure increased from 165 to 503 psia. This behavior can only come about by increased mass/energy accumulation in the rocket combustion chamber. Thus, the experiments indicate that increased propellant evaporation and subsequent burning is the mechanism by which the gasdynamic flow-field drives the waves.

At the injector face, the wave is reflected and starts a second traverse of the chamber. In all, three complete cycles are required before the steady-state component of the pressure is reduced to the prewave value.

Another item of interest is the following. The local speed of sound of the initial wave referenced to the gas is given in column 1 of Fig. 4.13. The data presented was obtained from four separate tests, the first three of which resulted in spontaneous instability (Fig. 4.10b). The wave is propagating into a highly oxidant rich combustion gas whose temperature is significantly below the adiabatic flame temperature for the injected O/F ratio. The wave velocity progressively increases as it proceeds downstream and this behavior is expected as a result of increased temperature in the axial direction. However, and more important, the wave continues to accelerate as it reflects from the sonic plane of the nozzle and propagates toward

the injector. This indicates that the temperature of the gases in the region near the injector face has increased. It is felt that this behavior can be explained by the increased turbulence of the gases behind the wave which induced increased mixing, and subsequent combustion. This is based on the fact that the temperature increase produced by the overpressure due to the compressional effect of the wave is about 3% and this value is too small to account for the increased wave velocity. In test 4, no instability occurred and no increase in velocity was observed.

Now consider the existence of possible relaxation times. It is noted in Fig. 4.10 that a characteristic time of about 80 microseconds appears both in the wave produced by the wave generator and in the spontaneously generated wave. This time corresponds to the period of the first tangential mode of oscillation. If, however, the first tangential mode was excited, then it would propagate axially with the particle velocity. This is clearly not the case in both wave groups. These waves propagate at the local speed of sound. Cold tests were made on the chamber with instrumentation for longitudinal and tangential and radial oscillatory behavior. These data did not contain this significant time value. The pressure transducer and their mounts were investigated to determine if the oscillations could be attributed to a mechanical or electrical origin. The transducers were dynamically calibrated in a shock tube both for amplitude response and the existence of "ring". In addition, hot firings were conducted with transducers mounted in blind holes. The results indicated that the 80 microsecond signal was not due to electrical noise, a hard mount, or a faulty transducer, but rather

occurs in the combustion gases. Since this time is greater than the expected chemical relaxation times and less than the normal sized droplet diffusion times through the film boundaries, the origin of the signal is in question. It is suggested however, that a non steady droplet evaporation-diffusion analysis be initiated to determine fuel vapor diffusion times of various sized droplets in films of various concentrations.

The previous wave propagation experiments were conducted primarily for observation of the phenomena and to deduce any mechanisms that could couple to the wave and cause sustained oscillations. The next phase of the program was to conduct a systematic investigation to determine the conditions under which input disturbances attenuate or amplify in liquid propellant rocket motors.

Previous work has demonstrated the importance of the physical processes of atomization, mixing and evaporation, droplet heat transfer and chemical reaction in determining the stability of a thrust chamber. If any of the previous processes are sensitive to pressure waves, then it is possible that coupling occurs with the result that oscillations are sustained and amplified. These processes are not distributed throughout the entire chamber, but are localized in extent. However, the longitudinal pressure waves propagate between the injector face and the sonic plane of the nozzle. Since it is possible for the wave to be distorted in regions of the chamber containing little or no sensitive processes, a complete understanding of wave attenuation phenomena requires particular emphasis upon the interaction of pressure waves and the entire thrust motor fluid dynamic field.

The experiments reported in this section were conducted in 2 in. diameter 500 lbf. nominal thrust, JP-5A-LOX rocket motor. The injectors are of the showerhead type or unlike impinging type with 16 fuel, (0.042-in. diam.) and 16 oxidizer, (0.0595-in. diam.) orifices. The average total propellant flow is 2.45 lbm/sec at an O/F ratio of 2.65. A 5% variation from the average flow rate is allowed for inclusion in the test results. The chamber length can be varied between 8 and 25 inches. The chamber and nozzle throat diameters are 2 and 1.65 in., respectively, resulting in a contraction ratio of 1.47.

After the start up transient has been completed, and steady state data obtained, the wave generator tube diaphragm is ruptured, and a wave propagates into the rocket motor thrust chamber. The wave generator tube is described previously in this section.

Three high frequency-response pressure transducers (Photocon model no. 352) are flush mounted in the chamber. They are located 2 in. from the injector face, 1 in. from the start of the nozzle contour, and midway between the injector and nozzle. Data are recorded on magnetic tape at 60 ips and played back at 1 ips into a recording oscillograph with a paper speed of 25 ips. Steady state pressure gradients are obtained before the wave input by connecting twelve axially spaced chamber pressure ports to a single transducer through a commutating system.

The data for the motors tested was reduced to obtain wave slope histories; $\frac{\partial p}{\partial t}$. The wave slope is defined as the ratio of wave pressure amplitude to wave rise time. The independent parameter selected for presentation of the results is the maximum value of the steady state axial

pressure gradient, $(\frac{\Delta P}{\Delta X})$ max. This latter parameter is the maximum slope on the steady state pressure versus axial distance curve obtained from the commutator system. It was chosen because it readily describes the type of fluid dynamic field through which the wave propagates. Variations in the magnitude of $(\frac{\Delta P}{\Delta X})$max were obtained by employing various combinations of injector configurations and chamber length.

Figure 4.14 shows the wave slope versus maximum pressure gradient for the incident wave at the injector (a), the incident wave at the nozzle (b), and the reflected wave at the injector (c). The shock driver tube pressure was 1300 psi and the steady state combustion chamber pressure was approximately 180 psi for all tests. Therefore the incident wave slope measured near the injector face is constant for most of the pressure gradients tested. At the highest values of pressure gradient considered the incident wave slope decreases rapidly. Since the higher values of $(\frac{\Delta P}{\Delta X})$ are produced closer to the injector face, wave slope-gas dynamic interactions have already caused a wave broadening effect at the first transducer location. The slope of the incident wave measured at the nozzle entrance, (Fig. 4.14b), decreases with an increase in the maximum slope of the axial pressure profile. Similar results are obtained for the slope of the nozzle reflected wave measured near the injector face; Fig. 4.14c.

More meaningful results can be seen by normalizing the latter two wave slopes with respect to the slope of the incident wave at the injector. Figure 4.15a indicates that the downstream propagating wave steepens at the lowest values of the pressure gradient and broadens at the higher values.

It should be noted at this point that all maximum pressure gradients less than 3 psi/in. were obtained with showerhead injectors and all values greater than 3 psi/in. were obtained with impinging injectors. Normalization of the slope of the nozzle reflected wave measured at the injector, Fig. 4.15b, shows that wave steepening is obtained with showerhead injectors and wave broadening is obtained with impinging injectors.

The ratio of the ordinates of Fig. 4.15b to Fig. 4.15a were calculated to determine the behavior of the nozzle reflected wave propagating from the nozzle to the injector. The ratio of the wave slope at the injector to the wave slope at the nozzle is always greater than unity, indicating wave steepening for all waves propagating upstream against an accelerating gas flow.

The occurence of wavelets behind the initial wave, and the subsequent coalescence of these wavelets to produce a smooth fronted wave near the nozzle entrance has been verified previously, Fig. 4.10. It is assumed that these wavelets occur due to the increased evaporation rate and subsequent combustion of the fuel in an oxidant rich environment. Some of the additional mass-energy is used to drive the wave, and part is available to increase the chamber base pressure. Figure 4.16 shows the ratio of base pressure at the injector at the arrival of the nozzle reflected wave to the pressure at that point prior to the incident wave. The data indicates that pressure amplification is inversely proportional to the chamber length and maximum slope of the steady state pressure curve. The amount of wave initiated evaporation, coalescence, and subsequent increase in chamber base pressure is greater with showerhead injectors than impinging injectors.

This may be related to the fuel drop size in the chamber. In the impinging injector motors, the fuel drop size is smaller and the conversion of liquid propellants to gaseous products is more rapid than in the showerhead injector motors. Therefore, there is less mass and energy available to drive the waves or increase the base pressure in the impinging injector motors.

For all injectors tested, the input waves tend to be completely attenuated and the base pressure assumes its pre-wave value after three traverses of the chamber. At this point, however, a second train of longitudinal waves occur in engines using showerhead injectors. These waves all have rise times of 50 microseconds, independent of the chamber length. The frequency of the disturbance (defined as the reciprocal of the time between two successive waves traveling in the same direction) corresponds to the fundamental longitudinal Mach number compensated mode. The presence of secondary oscillations is not found with impinging injector motors.

In conclusion, it appears that wave steepening and pressure amplification are strongly coupled to the steady state gas dynamic flow field through which the wave must propagate. Those injector-chamber configurations which result in rapid propellant utilization and high pressure gradients tend to inhibit wave growth. Less rapid conversion to gaseous products, with an attendant low pressure gradient, provides an energy and mass source to drive the wave and amplify the base pressure.

SECTION V

CONCLUSIONS

The purpose of this investigation is to develop an analytical spray combustion model for a liquid bi-propellant rocket motor. Concomitant experimental investigations of the non-oscillatory steady-state gas-dynamic behavior and longitudinal wave propagation phenomena are pursued.

A two-component spray combustion analysis is formulated. The model considers separate evaporation of both fuel and oxidizer. In addition, combustion gas properties are determined at the local O/F ratio from chemical equilibrium considerations. The analysis has been successfully programmed for the I. B. M. 7040. By removing the restrictive assumption of proportional evaporation used in previous investigations[4, 34] a more accurate description of the aerothermochemical phenomena is obtained.

The presently reported spray combustion model is of immediate use to the designer of stable rocket motor configurations. It can also provide well defined initial conditions for future analyses of combustion instability. The accuracy of the model is dependent upon the accuracy of the assumptions used in formulating the analysis. Therefore, more detailed studies of injection processes, i. e., jet fragmentation, break-up, droplet distributions and droplet shattering are recommended as a result of the present effort.

The results of the non-oscillatory steady state experiments indicate that variations in injector configuration produce variations in axial pressure history in a constant area liquid propellant rocket motor. These pressure

variations are due to changes in the mixing and shattering characteristics of different injectors and are concurrent with unique evaporation and mass liberation profiles. For an injector that promotes rapid droplet breakup and intimate mixing of propellants, the chamber pressure has a maximum gradient close to the injector face with a correspondingly high gas acceleration.

The wave propagation experiments subsequently proved that wave steepening and pressure amplification are strongly coupled to the steady state gas dynamic flow field through which the wave propagates. Those injector-chamber configurations which result in rapid propellant utilization and high pressure gradients tend to inhibit wave growth. Less rapid conversion to gaseous products, with an attendant low pressure gradient, provides an energy and mass source to drive the wave and amplify the base pressure.

SECTION VI

REFERENCES

1. Miesse, C. C., Industrial and Engineering Chemistry, Vol. 50, no. 9, pp. 1303-4, (1958).

2. Bittker, D. A. and Brokaw, R. S., Journal of the American Rocket Society, Vol. 30, no. 2, pp. 179-185, (1960).

3. Lambiris, S. and Combs, L. P., "Steady State Combustion Measurements in a LOX/RP-1 Rocket Chamber and Related Spray Burning Analysis", in Progress in Astronautics and Rocketry-Vol. 6: Detonation and Two Phase Flow, Academic Press, New York, (1962).

4. Burstein, S. F., Hammer, S. S. and Agosta, V. D., "A Spray Combustion Model with Droplet Breakup, Analytical and Experimental Results", in ibid.

5. Torda, T. P., "Aerothermochemistry of Liquid Propellant Rocket Combustion Chambers", Polytechnic Institute of Brooklyn, PRL TN 59-3, (1959).

6. Priem, R. J. and Heidmann, M. F., "Propellant Vaporization as a Design Criterion for Rocket Engine Combustion Chambers", NASA TR R-67, (1960).

7. Mayer, E., Journal of the American Rocket Society, Vol. 29, no. 7, p. 505, (1959).

8. Goldsmith, M. and Penner, S. S., ibid., Vol. 24, p. 245, (1954).

9. Spalding, D. B., "A One-Dimensional Theory of Liquid Fuel Rocket Combustion", Aeronautical Research Council A. R. C. 20, p. 175, London, England (1958).

10. Williams, F. A., Progress in Astronautics and Rocketry, Vol 2: Liquid Rockets and Propellants, pp. 229-264, Academic Press, New York, (1960).

11. Rabin, E., Schallenmuller, A.R. and Lawhead, R. B., "Displacement and Shattering of Propellant Droplets", United States Air Force Office of Scientific Research, AFOSR TR 60-75, March 1960.

12. Lane, W. R., Industrial and Engineering Chemistry Vol. 43, no. 6, p. 1312, (1951).

13. Ingebo, R. D., "Drop Size Distribution for Impinging-Jet Break-up in Airstreams Simulating the Velocity Conditions in Rocket Combustors", NACA TN 4222, (1958).

14. Putnam, A. A., Thomas, R. E. (editors) and the staff of Batelle Memorial Institute, "Injection and Combustion of Liquid Fuels", WADC Technical Report 56-344, Wright Air Development Center, Ohio, (1957).

15. Gunder, D. F. and Friant, D. R., Journal of Applied Mechanics, Vol. 17, p. 327, (1950).

16. Summerfield, M., Journal of the American Rocket Society, Vol. 21, p. 108, (1951).

17. Crocco, L., ibid., Vol. 21, p. 163, (1951); Vol. 22, p. 7, (1952).

18. Barrère, M. and Moutet, A., ibid., Vol. 26, p. 9, (1956).

19. Lee, Y. C., Gore, M. R. and Ross, C. C., ibid. Vol. 23, p. 75, (1953).

20. Marble, F. D. and Cox, D. W., Jr., ibid., Vol. 23, p. 33, (1953).

21. Levine, R. S. and Lawhead, R. W., "A Survey of Combustion Instability in Liquid Propellant Rocket Motors", ARS Paper 63-52, 1952.

22. Heidmann, M. F. and Priem, R. J., "Application of an Electro-Optical Two Color Pyrometer to Measurement of Flame Temperatures for Liquid Oxygen-Hydrocarbon Propellant Combustion", NACA TN 3033, (1953).

23. Berman, K. and Logan, S., Journal of the American Rocket Society, Vol. 22, no. 2, pp. 78-85, (1952).

24. Berman, K. and Cheney, S., ibid. Vol. 23, no. 2 (1953).

25. Ellis, H., Odgers, I., Stosick, A. J., Vander Verg, N. and Wick, R. S., "Experimental Investigation of Combustion Instability in Rocket Motors". Fourth Symposium on Combustion, pp. 880-895, Williams and Wilkens Co., Baltimore, Md., (1953).

26. Crocco, L. and Cheng, S. I., "Theory of Combustion Instability in Liquid Propellant Rocket Motors." AGARD Monograph no. 8, Butterworths Scientific Pub., Ltd., London, (1956).

27. Crocco, L., Grey, J. and Harrje, D. T., Journal of the American Rocket Society, Vol. 30, no. 2, pp. 159-168, (1960).

28. Tischler, A. O., Massa, R. V. and Mantler, R. L., "An Investigation of High Frequency Combustion Oscillations in Liquid Propellant Rocket Engines." NACA RM E53 B27, (1953).

29. Feiler, C. E., "Effect of Fuel Drop Size and Injector Configuration on Screaming in a 200 Pound Thrust Rocket Engine Using Liquid Oxygen and Heptane," NACA RM E58 A20a, (1958).

30. Bailey, C. R., "Performance and Stability of Rocket Engine Injectors Using LOX/RP-1 Propellants," NASA TM-X-53126, (1964).

31. Zucrow, M. J. and Osborn, J. R., Journal of the American Rocket Society, Vol. 28, no. 10, p. 654, (1958).

32. Lambiris, S., Combs, L. P. and Levine, R. S., "Stable Combustion in Liquid Propellant Rocket Engines," in Combustion and Propulsion-Fifth Agard Colloqium on High Temperature Phenomena, (1962).

33. Levine, R. S., "A Model of Liquid Propellant Rocket Engine Combustion", Report R-2077, Rocketdyne, a division of North American Aviation, Inc. Canoga Park, Calif., (1960).

34. Burstein, S. F. and Agosta, V. D., "Combustion Instability: Nonlinear Analysis of Wave Propagation in a Liquid Propellant Rocket Motor," Polytechnic Institute of Brooklyn, Propulsion Research Laboratory Report 62-15 AD 282970 (1962).

35. Agosta, V. D. and Mazzitelli, D. A., "A Theoretical Study of the Vibratory Forcing Functions in Axial Flow Turbo-Jet Engines Due to Flow Pulsations," Wright Air Development Center TR 56-74 (1956).

36. Ranz, W. E. and Marshall, W. R., Jr., "Evaporation from Drops", Part I. Chemical Engineering Progress, March 1952, Vol. 48, pp. 141-146.

37. Bird, R. B., Stewart, W. E. and Lightfoot, E. N., "Transport Pheromena", John Wiley and Sons, Inc., (1960).

38. Ingebo, R.D., "Vaporization Rates and Drag Coefficients for Isooctane Sprays in Turbulent Air Streams," NACA TN 3265, 1954.

39. Barber, L. and Hersch, M., Personal Communications, "Theoretical Performance of JP-5A and Liquid Oxygen Assuming Equilibrium Composition. NASA Lewis Research Laboratories, Nov. 1964.

APPENDIX A

SPRAY COMBUSTION COMPUTER PROGRAM

The program is written for the I. B. M. 7040 digital computer, using the Fortran IV language. The computational procedure is controlled by a MAIN program which, in turn, controls a number of subroutines. Only the MAIN program and those subroutines which form the core of the computational scheme are appended to this discussion. The following is a terse explanation of the entire program.

MAIN PROGRAM

READ - This routine reads in input data for one case. This data includes the following.

CHAMBL - length of combustion chamber.

CONOZL - length of converging nozzle.

FDSHNO - fuel drop shatter number; which represents the number of drops of total equivalent mass that are used to replace a single drop that has exceeded the Weber number criteria.

FJFLOI - injected mass flow rate of fuel.

FJVELI - fuel jet injection velocity.

FWTMOL - fuel molecular weight.

VARMAX - convergence criteria.

WEBCR - critical Weber number.

NOFDRS - number of different size fuel drops used to represent the spray.

NOITRS - maximum number of allowable iterations.

NOPNTS - number of points into which the rocket motor is divided.

The next five quantities are read in for each of the classes of fuel drops ranging from I = 1, NOFDRS.

FDCONB(I) = concentration or percent of total injected fuel flow represented by the I^{th} class.

FDPOSB(I) = axial position at which drops form.

FDRADB(I) = initial fuel drop radius.

FDTEMB(I) = initial fuel drop temperature.

FDVELB(I) = initial fuel drop velocity.

All of the above quantities which relate to the boundary conditions on the injected fuel, (those containing F in the symbol), are also read in for the injected oxidizer. The READ routine also controls the initial guess on the values of gas pressure (PA), gas velocity (VA), combusted gas O/F ratio (EA) and gas temperature (TA) at the injector. The READ routine then calls CGGUESS which uses appropriate functions to assume a value for each of the last four parameters at every point in the chamber-nozzle.

RDWRIT - This routine writes out the data that was previously read and documents it. The initial combusted gas profile calculated in CGGUESS is also documented.

DO 400 - This statement controls the number of iterations to be made between the liquid and gas systems.

COMSET - The last set of combustion gas parameters, pressure,

temperature, velocity, density, are stored prior to the start of the next iteration.

TITLE - This routine documents the start of an iteration.

FBSET - The method of computation involves calculating the history of a single drop of each of the drop classes and then summing over all of the drops of all of the classes to determine the bulk fuel parameters, prior to starting the combustion gas caculations. Since the bulk quantities are determined from a summation procedure, the bulk fuel properties at every point must be set equal to zero prior to a new calculation of droplet histories. FBSET performs this operation.

DO 200 KLASS = 1, NOFDR(- This do loop controls calculation of fuel droplet histories for each of the classes of fuel drops.

FDHIST - This subroutine calculates the history of a single drop of one of the drop classes from the point at which droplets are formed to the point at which the drop radius is zero. The actual solution of the drop Eqs. (9, 10, 11) is performed in FDADV. The equations are numerically integrated over a small distance such that the drop temperature does not change by more than 10^{o}F. The combustion gas properties required to perform the calculations are determined at each point by interpolation of the parameters between the bracketing major points. If the critical Weber number is exceeded, the drop population, which is initially unity, is multiplied by the fuel drop shatter number (FDSHNO). In addition, the drop radius is divided by the cube root of the shatter number. FDADV also calculates the energy of the vaporized fuel above the datum level, (FDHES), as

explained in Section II, Eq. (26).

FDWRIT writes the results of the fuel drop calculations.

FMACRO calculates the macro parameters for a drop class by multiplying the force on a single drop (FDFOR), the work done by a single drop (FDFOV), the heat transferred to a single drop (FDHET) and the energy above the datum level (FDHES) by the number of drops of the I^{th} class per unit length. In addition, the flow rate of a class of drops (lbm/sec) is calculated at each point by multiplying the mass of a single drop by the number of drops per second.

FMWRIT writes the results of the macro calculations

FBSUM adds up the results of the macro calculations from each class of drops at every point. The following quantities are obtained.

FBFLO - the total liquid fuel flow per second.

FBFOR - the force on all of the liquid drops per unit length.

FBFOV - the work done on the liquid drops per unit length per unit time.

FBHET - the heat transferred to the drops per unit length per unit time.

FBHES - the total energy of the evaporated fuel above the datum level per unit length per unit time.

FBWRIT writes the results of FBSUM after all of the fuel drop classes have been calculated.

The next nine statements in the MAIN PROGRAM, from OBSET to

OBWRIT control the calculation of oxidizer histories.

CGPROP - This routine controls solution of the gas system Eqs. (12, 14, 19, 23). It determines the ratio of evaporated oxidizer to evaporated fuel within each interval, (EDRAT, referred to as ELOF in Eq. (25)), by calculating the ratio of the decrease in OBFLO to the decrease in FBFLO. The combusted gas O/F ratio at each point is calculated according to Eq. (24) of Section II. The DO 200 loop within CGPROP calculates the combusted gas flow at each point by subtracting the bulk oxidizer and fuel flows from the injected flow rates. This DO loop also determines the boundary condition on gas velocity by solving the continuity equation using values assigned to PA, TA and EA in CGGUESS and the previously calculated gas flow rate. The DO 400 loop controls calculation of gas properties from the point at which the first drops form to the nozzle throat. The actual solution of the equations in performed in CGADV.

CGADV uses the results of the bulk liquid calculations to numerically integrate the gas system equations. Values of the energy coupling terms, i.e., BFOR, BHET, BHES, and BFOV as well as the combusted gas flow (FLO) are determined at each minor subdivision by interpolating between the major points. The number of minor subdivisions within each major segment is increased from 8 to 200 in the first four segments and from 8 to 50 throughout the converging portion of the nozzle. This procedure, in the region where large changes in gas properties are probable, has assured slowly changing integrands. However, provisions have been made in the routine for inserting a test on the magnitude of the change in a

variable, with subsequent step size reduction.

The Mach number of the gas flow is calculated after convergence is obtained within the minor subdivision. If the Mach number is greater than one, the routine (CGPROP) resets itself, interpolates a new pressure boundary condition and repeats the gas calculation.

Prior to returning to the MAIN PROGRAM, CGPROP will call MAKWON after the DO 400 loop has been completed. This latter subroutine calculates the Mach number at the throat and compares it with prescribed limits. If the throat Mach number is out of range, a new pressure boundary condition is interpolated and transfer is made to the DO 200 loop within CGPROP. The range of limits chosen for the throat Mach number is; $0.97 < M < 1.03$. The apparent 3% deviation from the boundary condition of $M = 1$ is solely in the interest of reducing computation time. Once a pressure boundary condition has been found that is consistent with the Mach number at the throat boundary condition, transfer is made to MAIN PROGRAM.

CGWRIT documents the results of the last gas profile computation.

COMPRE determines the maximum deviation (VAR) of the gas variables between successive iterations.

The IF (N9. LT. 0) statement forces a return to the drop calculations if the pressure boundary condition has been changed since the last drop calculations.

The IF (VARMAX-VAR) statement tests for convergence to a solution. If convergence has not been attained, the drop calculations are entered using information obtained from the last gas profile calculations. When the

convergence criteria is satisfied, the program leaves the major DO 400 loop.

MAKWON - This routine has been described previously. Calling it at this point in the program is actually redundant since the Mach number at the throat has previously been tested prior to exit from CGPROP.

GO TO 100 - This statement permits the calculations to be repeated if more than one set of droplet boundary conditions were initially specified.

The following list of function subroutines are required.

CHAREA - cross-sectional area as a function of axial distance.

FDENS - fuel density as a function of temperature.

FHEVAP - fuel heat of vaporization as a function of temperature.

FLSPH - liquid fuel specific heat as a function of temperature.

FSTEN - fuel surface tension as a function of temperature.

FVPRE - fuel vapor pressure (lbf/ft^2) as a function of temperature.

FVSPH - fuel vapor specific heat as a function of temperature.

A similar set of property subroutines must be specified for the oxidizer. These are titled and called in the program by replacing F with O. The data may be given as an equation or it may be specified in tabular form, with the value of the property determined by an interpolation subroutine (TERP). An example of the former case (OVPRE), and the latter (FHEVAP) are given in the sample listings.

The diffusivity D_V, defined in Section II, is given for the fuel (FDIFUS) and the oxidizer (ODIFUS) as a function subroutine. The arguments are gas temperature and pressure. Diffusivity was included as a separate

subroutine, rather than in the FDADV routine, since it is a function of the particular propellants being analyzed.

CGWMOL - combustion gas molecular weight as a function of temperature and O/F ratio

CGSPHT - combustion gas specific heat as a function of temperature and O/F ratio

CGVISC - combustion gas viscosity as a function of temperature and O/F ratio

CGENTS - heat of reaction of the propellant combination per pound of products, measured at the base temperature as a function of O/F ratio.

In addition to the above data, information must be available concerning the enthalpy, temperature and O/F ratio of the combusted gas. The base level for enthalpy must of course be consistent with that used in CGENTS. In the present analysis enthalpy-temperature relations are tabulated for various O/F ratios ranging from zero to 100. A double interpolation routine (DP) determines either enthalpy or temperature whenever the O/F ratio and either of the preceding variables is specified. The arguments associated with DP are O/F ratio, enthalpy and temperature, in that order. If for example, T and O/F are known, and enthalpy is to be determined, the following instructions are required, (see CGADV listing).

```
HH = 0
CALL DP(OF, HH, T)
```

The enthalpy will be interpolated and stored in HH. In general, the argument to be interpolated, is set equal to zero prior to calling DP.

```
0486M  DIAMOND - HAMMER  **TW                    FORTRAN SOURCE LIST
       ISN        SOURCE STATEMENT

         0 $IBFTC BOB      DECK
         1        DIMENSION CGDEN(129),CGFLO(129),CGPOS(129),CGPRE(129),CGTEM(129),
                 1   CGVEL(129),CGWMO(129)
         2        DIMENSION FDRAT(129),EIRAT(129)
         3        DIMENSION FBFLO(129),FBFOR(129),FBFOV(129),FBHES(129),FBHET(129),
                 1   FBPOP(129),FBVEL(129),
                 2   FDFOR(129),FDFCV(129),FDHES(129),FDHET(129),FDPOP(129),
                 3   FDPOS(129),FDRAD(129),FDTEM(129),FDTIM(129),FDVEL(129),
                 4   FMFLO(129),FMFCR(129),FMFOV(129),FMHES(129),FMHET(129),
                 5   FMPOP(129)
         4        DIMENSION FDCONB(33),FDPOSB(33),FDRADB(33),FDTEMB(33),FDVELB(33)
         5        DIMENSION OBFLO(129),OBFOR(129),OBFOV(129),OBHES(129),OBHET(129),
                 1   OBPOP(129),OBVEL(129),
                 2   ODFOR(129),ODFCV(129),ODHES(129),ODHET(129),ODPOP(129),
                 3   ODPOS(129),ODRAD(129),ODTEM(129),ODTIM(129),ODVEL(129),
                 4   OMFLO(129),OMFCR(129),OMFOV(129),OMHES(129),OMHET(129),
                 5   OMPOP(129)
         6        DIMENSION ODCONB(33),ODPOSB(33),ODRADB(33),ODTEMB(33),ODVELB(33)
         7        DIMENSION PAGETI(12),PROGTI(12)
        10        DIMENSION SCGDEN(129),SCGFLO(129),SCGPRE(129),SCGTEM(129),
                 1   SCGVEL(129)
        11        COMMON CGDEN,CGFLO,CGPOS,CGPRE,CGTEM,CGVEL,CGWMO
        12        COMMON EDRAT,EIRAT
        13        COMMON FBFLO,FBFOR,FBFOV,FBHES,FBHET,FBPOP,FBVEL,
                 1   FDFOR,FDFCV,FDHES,FDHET,FDPOP,FDPOS,FDRAD,FDTEM,FDTIM,FDVEL,
                 2   FMFLO,FMFCR,FMFCV,FMHES,FMHET,FMPOP
        14        COMMON FDCONB,FDPOSB,FDRADB,FDTEMB,FDVELB
        15        COMMON OBFLO,OBFOR,OBFCV,OBHES,OBHET,OBPOP,OBVEL,
                 1   ODFOR,ODFCV,ODHES,ODHET,ODPOP,ODPOS,ODRAD,ODTEM,ODTIM,ODVEL,
                 2   OMFLO,OMFCR,OMFCV,OMHES,OMHET,OMPOP
        16        COMMON ODCONB,ODPOSB,ODRADB,ODTEMB,ODVELB
        17        COMMON PAGETI,PROGTI
        20        COMMON SCGDEN,SCGFLO,SCGPRE,SCGTEM,SCGVEL
        21        COMMON CHAMBL,CONOZL,DINOZL,FDSHNO,FJFLOI,FJVELI,FWTMOL,GENTHS,
                 1   GWTMOL,ODSHNO,OJFLOI,OJVELI,OWTMOL,VARMAX,WEBRCR
        22         COMMON NOFDRS,NOITRS,NOODRS,NOPTS
        23        COMMON LTIN,LTOUT
        24        EQUIVALENCE (NOFPTS,NOGPTS,NOOPTS,NOPNTS)
        25         COMMON/CLASS/KLASS
        26         COMMON/FORCE/N9
        27        LTIN=5
        30        LTOUT=6
        31   100  CONTINUE
        32        CALL READ
        33        CALL RDWRIT
        34         COMMON/BOUDRY/ PA,TA,VA,ELM,EA
        35         COMMON/TEST/ NA,NB,PMIN,PMAX
        36        DO 400 IT=1,NOITRS
        37         IF(IT.GT.2) GO TO 101
        42         PMIN=PA
        43         PMAX=PA
        44         NA=0
        45         NB=0
        46   101   CONTINUE
        47        CALL COMSET
```

```
:048M  DIAMOND - HAMMER  **Tw                    FORTRAN SOURCE LIST BOB
       ISN       SOURCE STATEMENT

        50       CALL TITLE(IT)
        51       CALL FBSET
        52       DO 200 KLASS=1,NOFCRS
        53       CALL FDHIST(KLASS)
        54       CALL FDWRIT(KLASS)
        55       CALL FMACRO(KLASS)
        56       CALL FMWRIT(KLASS)
        57       CALL FBSUM(KLASS)
        60   200 CONTINUE
        62       CALL FBWRIT
        63        CALL OBSET
        64       DO 300 KLASS =1,NOOORS
        65       CALL ODHIST(KLASS)
        66       CALL ODWRIT(KLASS)
        67       CALL OMACRO(KLASS)
        70       CALL OMWRIT(KLASS)
        71       CALL OBSUM(KLASS)
        72   300 CONTINUE
        74       CALL OBWRIT
        75 20002  CALL CGPROP
        76       CALL CGWRIT
        77       CALL COMPRE(VAR)
       100        IF(N9.LT.0)GOTO400
       103       IF(VARMAX-VAR) 400,400,500
       104   400  N9=1
       106   500 CONTINUE
       107        CALL MAKWON(CGVEL(NOPNTS),CGTEM(NOPNTS),N9)
       110        IF(N9.LT.0)GOTO20002
       113       GO TO 100
       114       END
```

```
$IBFTC FDHIST  DECK
      SUBROUTINE FDHIST(KLASS)
       COMMON/FHEAT/SHINT
      DIMENSION CGDEN(129),CGFLO(129),CGPOS(129),CGPRE(129),CGTEM(129),
     1    CGVEL(129),CGWMO(129)
      DIMENSION EDRAT(129),EIRAT(129)
      DIMENSION FBFLO(129),FBFOR(129),FBFOV(129),FBHES(129),FBHET(129),
     1    FBPOP(129),FBVEL(129),
     2    FDFOR(129),FDFOV(129),FDHES(129),FDHET(129),FDPOP(129),
     3    FDPOS(129),FDRAD(129),FDTEM(129),FDTIM(129),FDVEL(129),
     4    FMFLO(129),FMFOR(129),FMFOV(129),FMHES(129),FMHET(129),
     5    FMPOP(129)
      DIMENSION FDCONB(33),FDPOSB(33),FDRADB(33),FDTEMB(33),FDVELB(33)
      DIMENSION OBFLO(129),OBFOR(129),OBFOV(129),OBHES(129),OBHET(129),
     1    OBPOP(129),OBVEL(129),
     2    ODFOR(129),ODFOV(129),ODHES(129),ODHET(129),ODPOP(129),
     3    ODPOS(129),ODRAD(129),ODTEM(129),ODTIM(129),ODVEL(129),
     4    OMFLO(129),OMFOR(129),OMFOV(129),OMHES(129),OMHET(129),
     5    OMPOP(129)
      DIMENSION ODCONB(33),ODPOSB(33),ODRADB(33),ODTEMB(33),ODVELB(33)
      DIMENSION PAGETI(12),PROGTI(12)
      DIMENSION SCGDEN(129),SCGFLO(129),SCGPRE(129),SCGTEM(129),
     1    SCGVEL(129)
      COMMON CGDEN,CGFLO,CGPOS,CGPRE,CGTEM,CGVEL,CGWMO
      COMMON EDRAT,EIRAT
      COMMON FBFLO,FBFOR,FBFOV,FBHES,FBHET,FBPOP,FBVEL,
     1    FDFOR,FDFOV,FDHES,FDHET,FDPOP,FDPOS,FDRAD,FDTEM,FDTIM,FDVEL,
     2    FMFLO,FMFOR,FMFOV,FMHES,FMHET,FMPOP
      COMMON FDCONB,FDPOSB,FDRADB,FDTEMB,FDVELB
      COMMON OBFLO,OBFOR,OBFOV,OBHES,OBHET,OBPOP,OBVEL,
     1    ODFOR,ODFOV,ODHES,ODHET,ODPOP,ODPOS,ODRAD,ODTEM,ODTIM,ODVEL,
     2    OMFLO,OMFOR,OMFOV,OMHES,OMHET,OMPOP
      COMMON ODCONB,ODPOSB,ODRADB,ODTEMB,ODVELB
      COMMON PAGETI,PROGTI
      COMMON SCGDEN,SCGFLO,SCGPRE,SCGTEM,SCGVEL
      COMMON CHAMBL,CONOZL,DINOZL,FDSHNO,FJFLOI,FJVELI,FWTMOL,GENTHS,
     1    GWTMOL,ODSHNO,OJFLOI,OJVELI,OWTMOL,VARMAX,WEBRCR
       COMMON NOFDRS,NOITRS,NOODRS,NOOPTS
      COMMON LTIN,LTOUT
      EQUIVALENCE (NOFPTS,NOGPTS,NOOPTS,NOPNTS)
      IFJLO=1
      IFJHI=1
      DO 300 I=1,NOPNTS
      IF(FDPOS(I)-FDPOSB(KLASS)) 200,300,300
  200 CONTINUE
      IFJHI=I
  300 CONTINUE
      IFDLO=IFJHI+1
      IFDHI=NOPNTS
      DO 400 I=IFJLO,IFJHI
      FDFOR(I)=0.
      FDFOV(I)=0.
      FDHES(I)=0.
      FDHET(I)=0.
      FDPOP(I)=0.
```

```
      FDRAD(I)=0.
      FDTEM(I)=0.
      FDTIM(I)=FDPOS(I)/FJVELI
      FDVEL(I)=0.
  400 CONTINUE
      POP=1.
       POS=FDPOS(IFJHI)
      RAD=FDRADB(KLASS)
      TEM=FDTEMB(KLASS)
      TIM=FDTIM(IFJHI)+(POS-FDPOS(IFJHI))/FJVELI
      VEL=FDVELB(KLASS)
      SHINT=0.
      DO 800 I=IFDLO,IFDHI
      IF(RAD) 500,500,600
  500 CONTINUE
      FDFOR(I)=0.
      FDFOV(I)=0.
      FDHES(I)=0.
      FDHET(I)=0.
      FDPOP(I)=0.
      FDRAD(I)=0.
      FDTEM(I)=0.
      FDTIM(I)=0.
      FDVEL(I)=0.
      GO TO 800
  600 CONTINUE
      POS=FDPOS(I-1)
      CALL FDADV(I,POP,POS,RAD,TEM,TIM,VEL)
  800 CONTINUE
```

```
$IBFTC FDADV   DECK
       SUBROUTINE FDADV (NXTPT,POP,POS,RAD,TEM,TIM,VEL)
       COMMON/CLASS/KLASS
       COMMON/FHEAT/ SHINT
      DIMENSION CGDEN(129),CGFLO(129),CGPOS(129),CGPRE(129),CGTEM(129),
     1   CGVEL(129),CGWMO(129)
      DIMENSION EDRAT(129),EIRAT(129)
      DIMENSION FBFLO(129),FBFOR(129),FBFOV(129),FBHES(129),FBHET(129),
     1   FBPOP(129),FBVEL(129),
     2   FDFOR(129),FDFOV(129),FDHES(129),FDHET(129),FDPOP(129),
     3   FDPOS(129),FDRAD(129),FDTEM(129),FDTIM(129),FDVEL(129),
     4   FMFLO(129),FMFOR(129),FMFOV(129),FMHES(129),FMHET(129),
     5   FMPOP(129)
      DIMENSION FDCONB(33),FDPOSB(33),FDRADB(33),FDTEMB(33),FDVELB(33)
      DIMENSION OBFLO(129),OBFOR(129),OBFOV(129),OBHES(129),OBHET(129),
     1   OBPOP(129),OBVEL(129),
     2   ODFOR(129),ODFOV(129),ODHES(129),ODHET(129),ODPOP(129),
     3   ODPOS(129),ODRAD(129),ODTEM(129),ODTIM(129),ODVEL(129),
     4   OMFLO(129),OMFOR(129),OMFOV(129),OMHES(129),OMHET(129),
     5   OMPOP(129)
      DIMENSION ODCONB(33),ODPOSB(33),ODRADB(33),ODTEMB(33),ODVELB(33)
      DIMENSION PAGETI(12),PROGTI(12)
      DIMENSION SCGDEN(129),SCGFLO(129),SCGPRE(129),SCGTEM(129),
     1   SCGVEL(129)
      COMMON CGDEN,CGFLO,CGPOS,CGPRE,CGTEM,CGVEL,CGWMO
      COMMON FDRAT,EIRAT
      COMMON FBFLO,FBFOR,FBFOV,FBHES,FBHET,FBPOP,FBVEL,
     1   FDFOR,FDFOV,FDHES,FDHET,FDPOP,FDPOS,FDRAD,FDTEM,FDTIM,FDVEL,
     2   FMFLO,FMFOR,FMFOV,FMHES,FMHET,FMPOP
      COMMON FDCONB,FDPOSB,FDRADB,FDTEMB,FDVELB
      COMMON OBFLO,OBFOR,OBFOV,OBHES,OBHET,OBPOP,OBVEL,
     1   ODFOR,ODFOV,ODHES,ODHET,ODPOP,ODPOS,ODRAD,ODTEM,ODTIM,ODVEL,
     2   OMFLO,OMFOR,OMFOV,OMHES,OMHET,OMPOP
      COMMON ODCONB,ODPOSB,ODRADB,ODTEMB,ODVELB
      COMMON PAGETI,PROGTI
      COMMON SCGDEN,SCGFLO,SCGPRE,SCGTEM,SCGVEL
      COMMON CHAMBL,CONOZL,DINOZL,FDSHNO,FJFLOI,FJVELI,FWTMOL,GENTHS,
     1   GWTMOL,ODSHNO,OJFLOI,OJVELI,OWTMOL,VARMAX,WEBRCR
       COMMON NOFDRS,NOITRS,NOODRS,NOOPTS
      COMMON LTIN,LTOUT
      EQUIVALENCE (NOFPTS,NOGPTS,NOOPTS,NOPNTS)
      GRCON=32.2
      UGCON=1545.
       NSUBDV=8
       NN=1
  126  DO 1000 J=NN,NSUBDV
       DLPOS=(FDPOS(NXTPT)-FDPOS(NXTPT-1))/FLOAT(NSUBDV)
       IF(RAD.LT.FDRADB(KLASS)/(10.*POP**.33333)) GO TO 700
      FRACT=(POS-FDPOS(NXTPT-1))/(FDPOS(NXTPT)-FDPOS(NXTPT-1))
      GEIR=EIRAT(NXTPT-1)+FRACT*(EIRAT(NXTPT)-EIRAT(NXTPT-1))
      GPRE=CGPRE(NXTPT-1)+FRACT*(CGPRE(NXTPT)-CGPRE(NXTPT-1))
      GTEM=CGTEM(NXTPT-1)+FRACT*(CGTEM(NXTPT)-CGTEM(NXTPT-1))
      GVEL=CGVEL(NXTPT-1)+FRACT*(CGVEL(NXTPT)-CGVEL(NXTPT-1))
      GWTM=CGWMO(NXTPT-1)+FRACT*(CGWMO(NXTPT)-CGWMO(NXTPT-1))
      TEMBAR=(TEM+GTEM)/2.
```

```
      GSPH=CGSPHT(TEMBAR,GEIR)
      GVIS=CGVISC(TEMBAR,GWTM)
      REYNUM=2.*RAD*ABS(GVEL-VEL)*GPRE*GWTM
     X    /(UGCON*TEMBAR*GVIS)
      SCHNUM=GVIS/(FDIFUS(TEMBAR,GPRE)*GPRE*GWTM
     X    /(UGCON*TEMBAR))
      COMAST=(2.+0.6*SCHNUM**(1./3.)*REYNUM**(1./2.)
     X    *FDIFUS(TEMBAR,GPRE)*FWTMOL/(UGCON*2.*RAD*TEMBAR)
      DAREA=4.*3.1415926*RAD**2
      DLTIM=DLPOS/VEL
       XDDMDT=DDMDT
       IF(TEM.EQ.0.) GO TO 700
       IF(GPRE.LT.FVPRE(TEM) ) GO TO 90
      DDMDT=DAREA*COMAST*GPRE*ALOG(ABS(GPRE/(GPRE-FVPRE(TEM))))
       OMEGA=AMAX1(DDMDT,XDDMDT)
       GO TO 98
 90    CONTINUE
       LOGICAL BOING
       BOING=DLTEM.NE.0.
       IF(BOING.AND.NSUBDV.LT.200) GO TO 99
       DDMDT=OMEGA
       GO TO 600
 98    CONTINUE
      H=(2.+0.525*SQRT(REYNUM))*GSPH*GVIS/(1.34*RAD)
      Z=DDMDT*FVSPH(TEMBAR)/(H*DAREA)
      IF(Z-1.E-4) 200,300,300
  200 CONTINUE
      Z=1.E-4
      GO TO 500
  300 CONTINUE
      IF(25.-Z) 400,500,500
  400 CONTINUE
      Z=25.
  500 CONTINUE
      HDNET=H*DAREA*(GTEM-TEM)*Z/(EXP(Z)-1.)
      HD=HDNET-DDMDT*FHEVAP(TEM)
      DVOL=4./3.*3.1415926*RAD**3
      HCAPD=FDENS(TEM)*DVOL*FLSPH(TEM)
      DLTEM=(HD/HCAPD)*DLTIM
       IF(ABS(DLTEM).GE.10.) GO TO 100
      IF(TEM+DLTEM) 700,700,601
  600   DLTEM=0.
  601 CONTINUE
      CODRAG=27./REYNUM**(0.84)
      ACCEL=(3./8.)*CODRAG*(GVEL-VEL)*ABS(GVEL-VEL)
     X    *(GWTM*GPRE/(UGCON*TEMBAR))/(FDENS(TEM)*RAD)
      DLVEL=ACCEL*DLTIM
      IF(VEL+DLVEL) 700,700,602
  602 CONTINUE
      DLRAD=-DDMDT*DLTIM/(DAREA*FDENS(TEM))
     X    -RAD*(FDENS(TEM+DLTEM)-FDENS(TEM))/(3.*FDENS(TEM))
      IF(RAD+DLRAD) 700,700,603
  603 CONTINUE
      GO TO 750
  700 CONTINUE
```

```
      DDMDT=0.
      XDDMDT=0.
     POP=0.
     RAD=0.
     DLRAD=0.
     TEM=0.
     DLTEM=0.
     TIM=0.
     DLTIM=0.
     VEL=0.
     DLVEL=0.
  750 CONTINUE
  900 CONTINUE
      XHEP=HEP
      XSHINT=SHINT
      XPOS=POS
      XPOP=POP
      XRAD=RAD
      XTEM=TEM
      XTIM=TIM
      XVEL=VEL
      XX=FDENS(TEM)*RAD**3
     POS=POS+DLPOS
     RAD=RAD+DLRAD
     TEM=TEM+DLTEM
     TIM=TIM+DLTIM
     VEL=VEL+DLVEL
      YY=FDENS(TEM)*RAD **3
      SHINT=SHINT+FLSPH(TEM)* DLTEM
      DT=DLTIM
      HEP=HEP+(SHINT+FHEVAP(TEM))*1.33333*3.14159*ABS(XX-YY)*POP/DT
     1  *1./FLOAT(NSUBDV)
     WBNUM=GWTM*GPRE*(GVEL-VEL       )**2*2.*(RAD       )
     X   /(UGCON*TEMBAR*FSTEN(TEM))
      IF(WEBRCR-WBNUM) 800,800,1000
  800 CONTINUE
      RAD=RAD/FDSHNO**.3333333
     POP=POP*FDSHNO
      OMEGA=RAD**2/XRAD**2*OMEGA
      DDMDT=OMEGA
 1000 CONTINUE
 1001     CONTINUE
      FDHES(NXTPT)=HEP
      HEP=0
     FDFOR(NXTPT)=DVOL*FDENS(TEM)*DLVEL/(DLTIM*GRCON)
     FDFOV(NXTPT)=FDFOR(NXTPT)*VEL
     FDHET(NXTPT)=HDNET
     FDPOP(NXTPT)=POP
     FDRAD(NXTPT)=RAD
     FDTEM(NXTPT)=TEM
     FDTIM(NXTPT)=TIM
     FDVEL(NXTPT)=VEL
     RETURN
   99  IF(J.EQ.1)TEM=TEM-ABS(DLTEM)
  100  NN=J*2-3
```

```
      DLPOS=DLPOS/2.
      NSUBDV=NSUBDV*2
      IF(NN.LT.0) GO TO 113
      POS=XPOS
      POP=XPOP
      RAD=XRAD
      TEM=XTEM
      TIM=XTIM
      VEL=XVEL
      HEP=XHEP
      SHINT=XSHINT
      GO TO 126
  113 NN=1
      GO TO 126
      END
$IBFTC ODADV   DBCK
      SUBROUTINEODADV(NXTPT,POP,POS,RAD,TEM,TIM,VEL)
      COMMON/CLASS/KLASS
      COMMON/FHEAT/ SHINT
      DIMENSION CGDEN(129),CGFLO(129),CGPOS(129),CGPRE(129),CGTEM(129),
     1   CGVEL(129),CGWMO(129)
      DIMENSION EDRAT(129),EIRAT(129)
      DIMENSION FBFLO(129),FBFOR(129),FBFOV(129),FBHES(129),FBHET(129),
     1   FBPOP(129),FBVEL(129),
     2   FDFOR(129),FDFOV(129),FDHES(129),FDHET(129),FDPOP(129),
     3   FDPOS(129),FDRAD(129),FDTEM(129),FDTIM(129),FDVEL(129),
     4   FMFLO(129),FMFOR(129),FMFOV(129),FMHES(129),FMHET(129),
     5   FMPOP(129)
      DIMENSION FDCONB(33),FDPOSB(33),FDRADB(33),FDTEMB(33),FDVELB(33)
      DIMENSION OBFLO(129),OBFOR(129),OBFOV(129),OBHES(129),OBHET(129),
     1   OBPOP(129),OBVEL(129),
     2   ODFOR(129),ODFOV(129),ODHES(129),ODHET(129),ODPOP(129),
     3   ODPOS(129),ODRAD(129),ODTEM(129),ODTIM(129),ODVEL(129),
     4   OMFLO(129),OMFOR(129),OMFOV(129),OMHES(129),OMHET(129),
     5   OMPOP(129)
      DIMENSION ODCONB(33),ODPOSB(33),ODRADB(33),ODTEMB(33),ODVELB(33)
      DIMENSION PAGETI(12),PROGTI(12)
      DIMENSION SCGDEN(129),SCGFLO(129),SCGPRE(129),SCGTEM(129),
     1   SCGVEL(129)
      COMMON CGDEN,CGFLO,CGPOS,CGPRE,CGTEM,CGVEL,CGWMO
      COMMON EDRAT,EIRAT
      COMMON FBFLO,FBFOR,FBFOV,FBHES,FBHET,FBPOP,FBVEL,
     1   FDFOR,FDFOV,FDHES,FDHET,FDPOP,FDPOS,FDRAD,FDTEM,FDTIM,FDVEL,
     2   FMFLO,FMFOR,FMFOV,FMHES,FMHET,FMPOP
      COMMON FDCONB,FDPOSB,FDRADB,FDTEMB,FDVELB
      COMMON OBFLO,OBFOR,OBFOV,OBHES,OBHET,OBPOP,OBVEL,
     1   ODFOR,ODFOV,ODHES,ODHET,ODPOP,ODPOS,ODRAD,ODTEM,ODTIM,ODVEL,
     2   OMFLO,OMFOR,OMFOV,OMHES,OMHET,OMPOP
      COMMON ODCONB,ODPOSB,ODRADB,ODTEMB,ODVELB
      COMMON PAGETI,PROGTI
      COMMON SCGDEN,SCGFLO,SCGPRE,SCGTEM,SCGVEL
      COMMON CHAMBL,CONOZL,DINOZL,FDSHNO,FJFLOI,FJVELI,FWTMOL,GENTHS,
     1   GWTMOL,ODSHNO,OJFLOI,OJVELI,OWTMOL,VARMAX,WEDRCR
      COMMON NOFDRS,NOITRS,NOODRS,NOOPTS
      COMMON LTIN,LTOUT
```

```
      EQUIVALENCE (NOEPTS,NOGPTS,NOOPTS,NOPNTS)
      GRCON=32.2
      UGCON=1545.
       NSUBDV=2
       NN=1
126    DO 1000 J=NN,NSUBDV
       DLPOS=(EDPOS(NXTPT)-EDPOS(NXTPT-1))/FLOAT(NSUBDV)
       IF(RAD.LT.ODRADS(KLASS)/(10.*POP**.33333)) GO TO 700
      FRACT=(POS-ODPOS(NXTPT-1))/(ODPOS(NXTPT)-ODPOS(NXTPT-1))
      GEIR=EIRAT(NXTPT-1)+FRACT*(EIRAT(NXTPT)-EIRAT(NXTPT-1))
      GPRE=CGPRE(NXTPT-1)+FRACT*(CGPRE(NXTPT)-CGPRE(NXTPT-1))
      GTEM=CGTEM(NXTPT-1)+FRACT*(CGTEM(NXTPT)-CGTEM(NXTPT-1))
      GVEL=CGVEL(NXTPT-1)+FRACT*(CGVEL(NXTPT)-CGVEL(NXTPT-1))
      GWTM=CGWMO(NXTPT-1)+FRACT*(CGWMO(NXTPT)-CGWMO(NXTPT-1))
      TEMBAR=(TEM+GTEM)/2.
      GSPH=CGSPHT(TEMBAR,GEIR)
      GVIS=CGVISC(TEMBAR,GWTM)
       REYNUM=2.*RAD*ABS(GVEL-VEL)*GPRE*GWTM
     X    /(UGCON*TEMBAR*GVIS)
       SCHNUM=GVIS/(ODIFUS(TEMBAR,GPRE)*GPRE*GWTM
     X    /(UGCON*TEMBAR))
       COMAST=(2.+0.6*SCHNUM**(1./3.)*REYNUM**(1./2.))
     X    *ODIFUS(TEMBAR,GPRE)*OWTMOL/(UGCON*2.*RAD*TEMBAR)
       DAREA=4.*3.1415926*RAD**2
           XDDMDT=DDMDT
        IF(TEM.EQ.0.) GO TO 700
        IF(GPRE.LT.OVPRE(TEM) ) GO TO 90
       DDMDT=DAREA*COMAST*GPRE*ALOG(ABS(GPRE/(GPRE-OVPRE(TEM))))
        OMEGA=AMAX1(DDMDT,XDDMDT)
        GO TO 98
90     CONTINUE
       LOGICAL BOING
       BOING=DLTEM.NE.0.
       IF(BOING.AND.NSUBDV.LT.200) GO TO 99
       DDMDT=OMEGA
       GO TO 600
98     CONTINUE
      H=(2.+0.525*SQRT(REYNUM))*GSPH*GVIS/(1.34*RAD)
      Z=DDMDT*OVSPH(TEMBAR)/(H*DAREA)
      IF(Z-1.E-4) 200,300,300
 200 CONTINUE
      Z=1.E-4
      GO TO 500
 300 CONTINUE
      IF(25.-Z) 400,500,500
 400 CONTINUE
      Z=25.
 500 CONTINUE
      HDNET=H*DAREA*(GTEM-TEM)*Z/(EXP(Z)-1.)
      HD=HDNET-DDMDT*OHEVAP(TEM)
      DVOL=4./3.*3.1415926*RAD**3
      HCAPD=ODENS(TEM)*DVOL*OLSPH(TEM)
      DLTIM=DLPOS/VEL
      DLTEM=(HD/HCAPD)*DLTIM
      IF(TEM+DLTEM) 700,700,601
```

```
600    DLTEM=0.
 601 CONTINUE
      DLTIM=DLPOS/VEL
     CODRAG=27./REYNUM**(0.84)
     ACCEL=(3./8.)*CODRAG*(GVEL-VEL)*ABS(GVEL-VEL)
    X    *(GWTM*GPRE/(UGCON*TEMBAR))/(ODENS(TEM)*RAD)
     DLVEL=ACCEL*DLTIM
     IF(VEL+DLVEL) 700,700,602
 602 CONTINUE
     DLRAD=-DDMDT*DLTIM/(DAREA*ODENS(TEM))
    X    -RAD*(ODENS(TEM+DLTEM)-ODENS(TEM))/(3.*ODENS(TEM))
     IF(RAD+DLRAD) 700,700,603
 603 CONTINUE
605    CONTINUE
      IF(ABS(DLTEM).GE.10.) GO TO 100
     GO TO 750
 700 CONTINUE
     POP=0.
     RAD=0.
     DLRAD=0.
     TEM=0.
     DLTEM=0.
     TIM=0.
     DLTIM=0.
      XDDMDT=0.
      DDMDT=0.
     VEL=0.
     DLVEL=0.
 750 CONTINUE
      XPOS=POS
      XHEP=HEP
      XSHINT=SHINT
      XPOP=POP
      XRAD=RAD
      XTEM=TEM
      XTIM=TIM
      XVEL=VEL
      FX=ODENS(TEM)*RAD**3
     RAD=RAD+DLRAD
     TEM=TEM+DLTEM
      FY=ODENS(TEM)*RAD**3
     TIM=TIM+DLTIM
     POS=POS+DLPOS
     VEL=VEL+DLVEL
     SHINT=SHINT+OLSPH(TEM)*DLTEM
      DT=DLTIM
      HEP=HEP+(SHINT+OHEVAP(TEM))*1.33333*3.14159*ABS(FX-FY)*POP/DT
    1*1./FLOAT(NSUBDV)
     WBNUM=GWTM*GPRE*(GVEL-VEL       )**2*2.*(RAD       )
    X    /(UGCON*TEMBAR*OSTEN(TEM))
      IF(WEBRCR-WBNUM) 800,800,1000
 800 CONTINUE
      RAD=RAD/FDSHNO**.333333
     POP=POP*ODSHNO
      OMEGA=RAD**2/XRAD**2*OMEGA
```

```
      DDMDT=OMEGA
1000  CONTINUE
1001      CONTINUE
      WRITE(6,2222)      NXTPT,NSUBDV
2222  FORMAT (1X2I8)
      ODFOR(NXTPT)=DVOL*ODENS(TEM)*DLVEL/(DLTIM*GRCON)
      ODFOV(NXTPT)=ODFOR(NXTPT)*VEL
      ODHES(NXTPT)=HEP
      HEP=0.
      ODHET(NXTPT)=HDNET
      ODPOP(NXTPT)=POP
      ODRAD(NXTPT)=RAD
      ODTEM(NXTPT)=TEM
      ODTIM(NXTPT)=TIM
      ODVEL(NXTPT)=VEL
      RETURN
99    IF(J.EQ.1) TEM=TEM-ABS(DLTEM)
 100  NN=J*2-3
      DLPOS=DLPOS/2.0
      NSUBDV=NSUBDV*2
      IF(NN.LT.0) GO TO 113
      POS=XPOS
      POP=XPOP
      RAD=XRAD
      TEM=XTEM
      TIM=XTIM
      VEL=XVEL
      HEP=XHEP
      SHINT=XSHINT
      GO TO 126
113   NN=1
      GO TO 126
      END
```

```
$IBFTC CGPROP  DECK
      SUBROUTINE CGPROP
      DIMENSION CGDEN(129),CGFLO(129),CGPOS(129),CGPRE(129),CGTEM(129),
     1   CGVEL(129),CGWMO(129)
      DIMENSION EDRAT(129),EIRAT(129)
      DIMENSION FBFLO(129),FBFOR(129),FBFOV(129),FBHES(129),FBHET(129),
     1   FBPOP(129),FBVEL(129),
     2   FDFOR(129),FDFOV(129),FDHES(129),FDHET(129),FDPOP(129),
     3   FDPOS(129),FDRAD(129),FDTEM(129),FDTIM(129),FDVEL(129),
     4   FMFLO(129),FMFOR(129),FMFOV(129),FMHES(129),FMHET(129),
     5   FMPOP(129)
      DIMENSION FDCONB(33),FDPOSB(33),FDRADB(33),FDTEMB(33),FDVELB(33)
      DIMENSION OBFLO(129),OBFOR(129),OBFOV(129),OBHES(129),OBHET(129),
     1   OBPOP(129),OBVEL(129),
     2   ODFOR(129),ODFOV(129),ODHES(129),ODHET(129),ODPOP(129),
     3   ODPOS(129),ODRAD(129),ODTEM(129),ODTIM(129),ODVEL(129),
     4   OMFLO(129),OMFOR(129),OMFOV(129),OMHES(129),OMHET(129),
     5   OMPOP(129)
      DIMENSION ODCONB(33),ODPOSB(33),ODRADB(33),ODTEMB(33),ODVELB(33)
      DIMENSION PAGETI(12),PROGTI(12)
      DIMENSION SCGDEN(129),SCGFLO(129),SCGPRE(129),SCGTEM(129),
     1   SCGVEL(129)
      COMMON CGDEN,CGFLO,CGPOS,CGPRE,CGTEM,CGVEL,CGWMO
      COMMON EDRAT,EIRAT
      COMMON FBFLO,FBFOR,FBFOV,FBHES,FBHET,FBPOP,FBVEL,
     1   FDFOR,FDFOV,FDHES,FDHET,FDPOP,FDPOS,FDRAD,FDTEM,FDTIM,FDVEL,
     2   FMFLO,FMFOR,FMFOV,FMHES,FMHET,FMPOP
      COMMON FDCONB,FDPOSB,FDRADB,FDTEMB,FDVELB
      COMMON OBFLO,OBFOR,OBFOV,OBHES,OBHET,OBPOP,OBVEL,
     1   ODFOR,ODFOV,ODHES,ODHET,ODPOP,ODPOS,ODRAD,ODTEM,ODTIM,ODVEL,
     2   OMFLO,OMFOR,OMFOV,OMHES,OMHET,OMPOP
      COMMON ODCONB,ODPOSB,ODRADB,ODTEMB,ODVELB
      COMMON PAGETI,PROGTI
      COMMON SCGDEN,SCGFLO,SCGPRE,SCGTEM,SCGVEL
      COMMON CHAMBL,CONOZL,DINOZL,FDSHNO,FJFLOI,FJVELI,FWTMOL,GENTHS,
     1   GWTMOL,ODSHNO,OJFLOI,OJVELI,OWTMOL,VARMAX,WEBRCR
       COMMON NOFDRS,NOITRS,NOODRS,NOOPTS
      COMMON LTIN,LTOUT
      EQUIVALENCE (NOFPTS,NOGPTS,NOOPTS,NOPNTS)
      DO 230 I=3,NOPNTS
      IF(FBFLO(I)-FBFLO(I-1)) 210,220,210
  210 CONTINUE
      EDRAT(I-1)=(OBFLO(I)-OBFLO(I-2))/(FBFLO(I)-FBFLO(I-2))
      GO TO 230
  220 CONTINUE
       EDRAT(I-1)=0.
       IF(FBFLO(I).EQ.FJFLOI) EDRAT(I-1)=100.
       IF(OBFLO(I).EQ.OJFLOI) EDRAT(I)=0.
  230 CONTINUE
      EDRAT(1)=0.
      EDRAT(NOPNTS)=EDRAT(NOPNTS-1)
      DO 260 I=1,NOPNTS
      IF(FJFLOI-FBFLO(I)) 240,250,240
  240 CONTINUE
      EIRAT(I)=(OJFLOI-OBFLO(I))/(FJFLOI-FBFLO(I))
```

```
      GO TO 260
  250 CONTINUE
       EIRAT(I)=100.
       IF(OJFLOI.EQ.OBFLO(I)) EIRAT(I)=0.
  260 CONTINUE
       COMMON/BOUDRY/PA,TA,VA,INITPT ,EA
       LLL=INITPT+1
   13  DO 200 I=LLL,NOPNTS
       CGFLO(I)=AMAX1(0.,(FJFLOI-FBFLO(I)+OJFLOI-OBFLO(I)))
       SCGFLO(I)=CGFLO(I)
       CGVEL(I)=CGFLO(I)*1545.*CGTEM(I)/(CGWMOL(CGTEM(I),EIRAT(I))*
     1 CGPRE(I)*CHAREA(FDPOS(I)))
       CGDEN(I)=CGFLO(I)/(CHAREA(FDPOS(I))*CGVEL(I))
       SCGDEN(I)=CGDEN(I)
  200  CONTINUE
       KK=LLL+1
       DO 400 NXTPT=KK,NOPNTS
      DEN=CGDEN(NXTPT-1)
      POS=FDPOS(NXTPT-1)
      PRE=CGPRE(NXTPT-1)
      TEM=CGTEM(NXTPT-1)
      VEL=CGVEL(NXTPT-1)
      CALL CGADV(NXTPT,DEN,POS,PRE,TEM,VEL)
  400 CONTINUE
       CALL MAKWON(CUD,DUM,N9)
       IF (N9.LT.0) GO TO 13
      DO 500 I=1,NOPNTS
      CGWMO(I)=CGWMOL(CGTEM(I),EIRAT(I))
  500 CONTINUE
      RETURN
       END
```

```
$IBFTC CGADV   DECK
      SUBROUTINE CGADV(NXTPT,DEN,POS,PRE,TEM,VEL)
      DIMENSION CGDEN(129),CGFLO(129),CGPOS(129),CGPRE(129),CGTEM(129),
     1   CGVEL(129),CGWMO(129)
      DIMENSION EDRAT(129),EIRAT(129)
      DIMENSION FBFLO(129),FBFOR(129),FBFOV(129),FBHES(129),FBHET(129),
     1   FBPOP(129),FBVEL(129),
     2   FDFOR(129),FDFOV(129),FDHES(129),FDHET(129),FDPOP(129),
     3   FDPOS(129),FDRAD(129),FDTEM(129),FDTIM(129),FDVEL(129),
     4   FMFLO(129),FMFOR(129),FMFOV(129),FMHES(129),FMHET(129),
     5   FMPOP(129)
      DIMENSION FDCONB(33),FDPOSB(33),FDRADB(33),FDTEMB(33),FDVELB(33)
      DIMENSION OBFLO(129),OBFOR(129),OBFOV(129),OBHES(129),OBHET(129),
     1   OBPOP(129),OBVEL(129),
     2   ODFOR(129),ODFOV(129),ODHES(129),ODHET(129),ODPOP(129),
     3   ODPOS(129),ODRAD(129),ODTEM(129),ODTIM(129),ODVEL(129),
     4   OMFLO(129),OMFOR(129),OMFOV(129),OMHES(129),OMHET(129),
     5   OMPOP(129)
      DIMENSION ODCONB(33),ODPOSB(33),ODRADB(33),ODTEMB(33),ODVELB(33)
      DIMENSION PAGETI(12),PROGTI(12)
      DIMENSION SCGDEN(129),SCGFLO(129),SCGPRE(129),SCGTEM(129),
     1   SCGVEL(129)
      COMMON CGDEN,CGFLO,CGPOS,CGPRE,CGTEM,CGVEL,CGWMO
      COMMON EDRAT,EIRAT
      COMMON FBFLO,FBFOR,FBFOV,FBHES,FBHET,FBPOP,FBVEL,
     1   FDFOR,FDFOV,FDHES,FDHET,FDPOP,FDPOS,FDRAD,FDTEM,FDTIM,FDVEL,
     2   FMFLO,FMFOR,FMFOV,FMHES,FMHET,FMPOP
      COMMON FDCONB,FDPOSB,FDRADB,FDTEMB,FDVELB
      COMMON OBFLO,OBFOR,OBFOV,OBHES,OBHET,OBPOP,OBVEL,
     1   ODFOR,ODFOV,ODHES,ODHET,ODPOP,ODPOS,ODRAD,ODTEM,ODTIM,ODVEL,
     2   OMFLO,OMFOR,OMFOV,OMHES,OMHET,OMPOP
      COMMON ODCONB,ODPOSB,ODRADB,ODTEMB,ODVELB
      COMMON PAGETI,PROGTI
      COMMON SCGDEN,SCGFLO,SCGPRE,SCGTEM,SCGVEL
      COMMON CHAMBL,CONOZL,DINOZL,FDSHNO,FJFLOI,FJVELI,FWTMOL,GENTHS,
     1   GWTMOL,ODSHNO,OJFLOI,OJVELI,OWTMOL,VARMAX,WEBRCR
       COMMON NOFDRS,NOITRS,NOODRS,NOOPTS
      COMMON LTIN,LTOUT
      EQUIVALENCE (NOFPTS,NOGPTS,NOOPTS,NOPNTS)
       COMMON/TEST/NA,NB,PMIN,PMAX
       COMMON/MAK/AMACH(129)
       COMMON/FORCE/N9
       COMMON/BOUDRY/PA,TA,VA,INITPT ,EA
      NSUBD=8
      GRCON=32.2
      HETME=778.
      UGCON=1545.
      SDEN=DEN
      SPOS=POS
      SPRE=PRE
      STEM=TEM
      SVEL=VEL
       KZ1=KZ1+1
```

```
      IF(FLOX.LE.1.E-10 .AND.FDPOS(NXTPT).LT.CHAMBL) NSUBD=1
      IF(KZ1.LE.NOPNTS/30) NSUBD =6000/NOPNTS
      IF( KZ1.GE.NOPNTS-INITPT-2-NOPNTS/30) NSUBD=6000/NOPNTS
      IF(NXTPT.EQ.NOPNTS) KZ1=0
  100 CONTINUE
      DEN=SDEN
      POS=SPOS
      PRE=SPRE
      TEM=STEM
      VEL=SVEL
      DLPOS=(FDPOS(NXTPT)-POS)/FLOAT(NSUBD)
      DO 1000 J=1,NSUBD
       IF(NTEST.EQ.1)GO TO 13
       XDEN=DEN
       XPRF=PRE
       XEMACH=EMACH
       XTEM=TEM
       XVEL=VEL
      FRAC1=(POS-FDPOS(NXTPT-1))/(FDPOS(NXTPT)-FDPOS(NXTPT-1))
      FRAC2=((POS+DLPOS)-FDPOS(NXTPT-1))/(FDPOS(NXTPT)-FDPOS(NXTPT-1))
      FLO=SCGFLO(NXTPT-1)+FRAC1*(SCGFLO(NXTPT)-SCGFLO(NXTPT-1))
      FLOX=(SCGFLO(NXTPT)-SCGFLO(NXTPT-1))/(FDPOS(NXTPT)-FDPOS(NXTPT-1))
      FFLOX=-(FBFLO(NXTPT)-FBFLO(NXTPT-1))/(FDPOS(NXTPT)-FDPOS(NXTPT-1))
      OFLOX=-(OBFLO(NXTPT)-OBFLO(NXTPT-1))/(ODPOS(NXTPT)-ODPOS(NXTPT-1))
      BFOR=(1.-FRAC2)*(FBFOR(NXTPT-1)+OBFOR(NXTPT-1)) +
     X    FRAC2*(FBFOR(NXTPT)+OBFOR(NXTPT))
      BFOV=(1.-FRAC2)*(FBFOV(NXTPT-1)+OBFOV(NXTPT-1)) +
     X    FRAC2*(FBFOV(NXTPT)+OBFOV(NXTPT))
       BHES=FBHES(NXTPT)+OBHES(NXTPT)
      BH_T=(1.-FRAC2)*(FBHET(NXTPT-1)+OBHET(NXTPT-1)) +
     X    FRAC2*(FBHET(NXTPT)+OBHET(NXTPT))
      BFVEL=(1.-FRAC2)*FBVEL(NXTPT-1) +FRAC2*FBVEL(NXTPT)
      BOVEL=(1.-FRAC2)*OBVEL(NXTPT-1) +FRAC2*OBVEL(NXTPT)
      AREA1=CHAREA(POS)
      AREA2=CHAREA(POS+DLPOS)
      FLOW1=FLO
       IF(FLOW1)110,150,110
  110  CONTINUE
      FLOW2=FLO+FLOX*DLPOS
      EIR1=(1.-FRAC1)*EIRAT(NXTPT-1)+FRAC1*EIRAT(NXTPT)
      EIR2=(1.-FRAC2)*EIRAT(NXTPT-1)+FRAC2*EIRAT(NXTPT)
       ENTS1=CGENTS(FLOX,FFLOX,OFLOX)
      D=DEN
      V=FLOW2/(AREA2*D)
       P=PRE-D*V*(V-VEL)/GRCON-(BFOR/AREA2)*DLPOS
      T=TEM
       HH=0.
       CALL DP(EIR1,HH,TEM)
       XX1=FLOW1       *(HH+VEL*VEL/(2.*GRCON*HETME))
       XX2= (BHES-BHET+ENTS1*FLOX)        *DLPOS
       XX=(XX1+XX2)/FLOW2
      DO 400 K=1,50
      SAVED=D
      SAVEP=P
      SAVET=T
```

```
      SAVEV=V
      V=FLOW2/(AREA2*SAVED)
       GGENTH=XX-SAVEV**2/(2.0*GRCON*HETME)
       TT=0.
       CALL DP(EIR2,GGENTH,TT)
       T=TT
  300 CONTINUE
       P=PRE-SAVED*SAVEV*(SAVEV-VEL)/GRCON-(BFOR/AREA2)*DLPOS
      D=SAVEP*CGWMOL(SAVET,EIR2)/(SAVET*UGCON)
       KQ=K
       IF(KQ.EQ.1) GOTO400
      DEVD=ABS((D-SAVED)/SAVED)
      DEVP=ABS((P-SAVEP)/SAVEP)
      DEVV=ABS((V-SAVEV)/SAVEV)
      DEVMX=AMAX1(DEVD,AMAX1(DEVP,AMAX1(DEVT,DEVV)))
       IF(1.0E-3.GE.DEVMX) GO TO 500
  400 CONTINUE
  500 CONTINUE
       OLDM=EMACH
       IF(NXTPT.LT.NOPNTS/3)OLDM=0.
       EMACH=V/SQRT(CGSPHT(T,EIR2)*GRCON*1545.*T/(CGSPHT(T,EIR2)*CGWMOL(
     1 T,EIR2)-1.958))
       DLMAK=EMACH-OLDM
       LOGICAL POINT
       POINT=FDPOS(NXTPT-1).GT.CHAMBL
       IF(EMACH.LE.1.0.AND.(DLMAK.GE.0..OR..NOT.POINT))GO TO 900
       IF(NXTPT.GE.NOPNTS) GO TO 1025
       WRITE(6,1) OLDM,EMACH,NXTPT,J
 1     FORMAT(10X9HOLD MACH= F6.3,5X5HMACH= F6.3,5X6HNXTPT=I4,5H   S=I3)
       NA=1
       IF(NB.EQ.1)GOTO135
       PA=PA*1.05
       GOTO7
 135   PMIN=PA
       PA=(PMIN+PMAX)/2.0
 7     CGPRE(INITPT)=PA
       CGPRE(INITPT+1)=PA
       KZ1=0
       N9=-1
       EXTERNAL CGPROP
       CALL SNEAKY(CGPROP)
 651   CONTINUE
  900 CONTINUE
      DEN=D
      PRE=P
      TEM=T
      VEL=V
      POS=POS+DLPOS
C IF IT IS DESIRED TO INSERT A SUBSTEP HALVING OPTION INTO THIS
C SUBROUTINE, JUST INSERT THE TEST, AND IF THE SUBSTEP LENGTH IS
C CHANGED, MAKE A SUBSEQUENT TRANSFER TO 100.  OTHERWISE GO ON AS USUAL.
C THIS IS A GOOD PLACE TO INSERT THE TEST IF ONE IS NEEDED.
 1000 CONTINUE
      CGDEN(NXTPT)=DEN
      CGPRE(NXTPT)=PRE
```

```
      CGTEM(NXTPT)=TEM
       H=GGENTH
      CGVEL(NXTPT)=VEL
       AMACH(NXTPT)=EMACH
       HO=H+V**2/50100.
       TO=0.
       CALL DP(EIR2,HO,TO)
       COMMON/TOHO/CGTO(129),CGHO(129)
       CGTO(NXTPT)=TO
       CP=CGSPHT(T,EIR2)
       GAMMA=CP/(CP-(1.986/CGWMOL(T,EIR2)))
       PEX=GAMMA/(GAMMA-1.)
       PO=P*(TO/T)**PEX
       CGHO(NXTPT)=PO
       WRITE(6,881)NXTPT,P,V,T,FLO,EIR1,GGENTH,EMACH
  6    FORMAT(1X,3I4,5E16.8)
      RETURN
1025  NTEST =0
       IF(NXTPT.NE.NOPNTS)NTEST=1
       WRITE(6,6)NXTPT,NSUBD,J,XTEM,XPRE,XDEN,XVEL,XEMACH
881    FORMAT(1XI4,7E15.8)
       DO 5 N=NXTPT,NOPNTS
       CGDEN(N)=XDEN
       CGTEM(N)=XTEM
       CGPRE(N)=XPRE
       CGVEL(N)=XVEL
       AMACH(N)=XEMACH
  5    CONTINUE
       RETURN
150    D=DEN
       P=PRE
       V=VEL
       T=TEM
       GO TO 900
13    NTEST=0
       RETURN
       END
```

```
$IBFTC MAKWON  DECK
       SUBROUTINE MAKWON(VEL,TEM,N9)
      DIMENSION CGDEN(129),CGFLO(129),CGPOS(129),CGPRE(129),CGTEM(129),
     1   CGVEL(129),CGWMO(129)
      DIMENSION EDRAT(129),EIRAT(129)
      DIMENSION FBFLO(129),FBFOR(129),FBFOV(129),FBHES(129),FBHET(129),
     1   FBPOP(129),FBVEL(129),
     2   FDFOR(129),FDFOV(129),FDHES(129),FDHET(129),FDPOP(129),
     3   FDPOS(129),FDRAD(129),FDTEM(129),FDTIM(129),FDVEL(129),
     4   FMFLO(129),FMFOR(129),FMFOV(129),FMHES(129),FMHET(129),
     5   FMPOP(129)
      DIMENSION FDCONB(33),FDPOSB(33),FDRADB(33),FDTEMB(33),FDVELB(33)
      DIMENSION OBFLO(129),OBFOR(129),OBFOV(129),OBHES(129),OBHET(129),
     1   OBPOP(129),OBVEL(129),
     2   ODFOR(129),ODFOV(129),ODHES(129),ODHET(129),ODPOP(129),
     3   ODPOS(129),ODRAD(129),ODTEM(129),ODTIM(129),ODVEL(129),
     4   OMFLO(129),OMFOR(129),OMFOV(129),OMHES(129),OMHET(129),
     5   OMPOP(129)
      DIMENSION ODCONB(33),ODPOSB(33),ODRADB(33),ODTEMB(33),ODVELB(33)
      DIMENSION PAGETI(12),PROGTI(12)
      DIMENSION SCGDEN(129),SCGFLO(129),SCGPRE(129),SCGTEM(129),
     1   SCGVEL(129)
      COMMON CGDEN,CGFLO,CGPOS,CGPRE,CGTEM,CGVEL,CGWMO
      COMMON EDRAT,EIRAT
      COMMON FBFLO,FBFOR,FBFOV,FBHES,FBHET,FBPOP,FBVEL,
     1   FDFOR,FDFOV,FDHES,FDHET,FDPOP,FDPOS,FDRAD,FDTEM,FDTIM,FDVEL,
     2   FMFLO,FMFOR,FMFOV,FMHES,FMHET,FMPOP
      COMMON FDCONB,FDPOSB,FDRADB,FDTEMB,FDVELB
      COMMON OBFLO,OBFOR,OBFOV,OBHES,OBHET,OBPOP,OBVEL,
     1   ODFOR,ODFOV,ODHES,ODHET,ODPOP,ODPOS,ODRAD,ODTEM,ODTIM,ODVEL,
     2   OMFLO,OMFOR,OMFOV,OMHES,OMHET,OMPOP
      COMMON ODCONB,ODPOSB,ODRADB,ODTEMB,ODVELB
      COMMON PAGETI,PROGTI
      COMMON SCGDEN,SCGFLO,SCGPRE,SCGTEM,SCGVEL
      COMMON CHAMBL,CONOZL,DINOZL,FDSHNO,FJFLOI,FJVELI,FWTMOL,GENTHS,
     1   GWTMOL,ODSHNO,OJFLOI,OJVELI,OWTMOL,VARMAX,WEBRCR
       COMMON NOFDRS,NOITRS,NOODRS,NOOPTS
      COMMON LTIN,LTOUT
      EQUIVALENCE (NOFPTS,NOGPTS,NOOPTS,NOPNTS)
       COMMON/TEST/NA,NB,PMIN,PMAX
       COMMON/BOUDRY/ PA,TA,VA,INITPT
       COMMON /MAK/ AMACH(129)
       REAL MACH
       MACH=AMACH(NOPNTS)
       PAD=PA
       IF(MACH.LT..97.OR.MACH.GT.1.03) GO TO 10
       N9=+1
    9  WRITE(6,20)     MACH,PAD,PA
   20  FORMAT(10X,1PE15.7,5X,E15.7,5X,E15.7)
       RETURN
   10  CONTINUE
       NB=1
       IF(NA.EQ.1) GOTO 135
       PA=MACH*PA
       GO TO 7
```

```
135   PMAX=PA
      PA=(PMIN+PMAX)/2.0
7     CGPRE(INITPT)=PA
      CGPRE(INITPT+1)=PA
      N9=-1
      GO TO 9
       END
```

```
$IBFTC DP
      SUBROUTINE DP(GOF,H,T)
      REAL M
      COMMON/GOFTH/      TABLE(8,39)
      DIMENSION SLOPE(2),CONST(2)
      DO 10 K=2,32765
 10   IF(TABLE(1,K).GE.GOF) GO TO 20
 20   K=K-1
 9    FRACT=(GOF-TABLE(1,K))/(TABLE(1,K+1)-TABLE(1,K))
      DO 50 J=1,2
      JJ=K+J-1
      SLOPE(J)=(TABLE(4,JJ)-TABLE(2,JJ))/(TABLE(5,JJ)-TABLE(3,JJ))
 50   CONST(J)=-((SLOPE(J)*TABLE(3,JJ))-TABLE(2,JJ))
      B=FRACT*(CONST(2)-CONST(1))+CONST(1)
      M=FRACT*(SLOPE(2)-SLOPE(1))+SLOPE(1)
      IF(H.EQ.0.)H=(T-B)/M
      IF(T.EQ.0.)T=M*H+B
 8    CONTINUE
      RETURN
      END


$IBFTC TERP    DECK
      FUNCTION TERP(XX,X,Y,NOXS)
      DIMENSION X(2),Y(2)
      IF(NOXS-1) 10,10,20
   10 CONTINUE
      TERP=Y(1)
      RETURN
   20 CONTINUE
      IF(XX-X(1)) 100,100,200
  100 CONTINUE
      TERP=Y(1)+((Y(2)-Y(1))/(X(2)-X(1)))*(XX-X(1))
      RETURN
  200 CONTINUE
      IF(X(NOXS)-XX) 300,300,400
  300 CONTINUE
      TERP=Y(NOXS)+((Y(NOXS)-Y(NOXS-1))/(X(NOXS)-X(NOXS-1)))
     X   *(XX-X(NOXS))
      RETURN
  400 CONTINUE
      DO 600 I=1,NOXS
      IF(X(I)-XX) 500,500,600
  500 CONTINUE
      II=I
  600 CONTINUE
      TERP=Y(II)+((Y(II+1)-Y(II))/(X(II+1)-X(II)))*(XX-X(II))
      RETURN
      END
```

```
$IBFTC FHEVAP  DECK
      FUNCTION FHEVAP(TEM)
      DIMENSION T(14),H(14)
      T(1)=540.
      T(2)=660.
      T(3)=710.
      T(4)=760.
      T(5)=810.
      T(6)=860.
      T(7)=910.
      T(8)=960.
      T(9)=1010.
      T(10)=1060.
      T(11)=1110.
      T(12)=1160.
      T(13)=1210.
      T(14)=1235.
      H(1)=150.
      H(2)=142.
      H(3)=137.
      H(4)=131.
      H(5)=125.
      H(6)=120.
      H(7)=113.
      H(8)=106.
      H(9)=98.
      H(10)=88.
      H(11)=75.
      H(12)=55.
      H(13)=25.
      H(14)=0.
      FHEVAP=TERP(1EM,T,H,14)
      RETURN
      END

$IBFTC OVPRE   DECK
      FUNCTION OVPRE(TEM)
      OVPRE=144.*EXP(11.9584-1476.4912/(TEM-3.568))
      RETURN
      END

$IBFTC CGENTS  DECK
       FUNCTION CGENTS(FLOX,FFLOX,OFLOX)
       CGENTS=1.8*(-362.97*FFLOX-96.25*OFLOX)/FLOX
       RETURN
       END
```

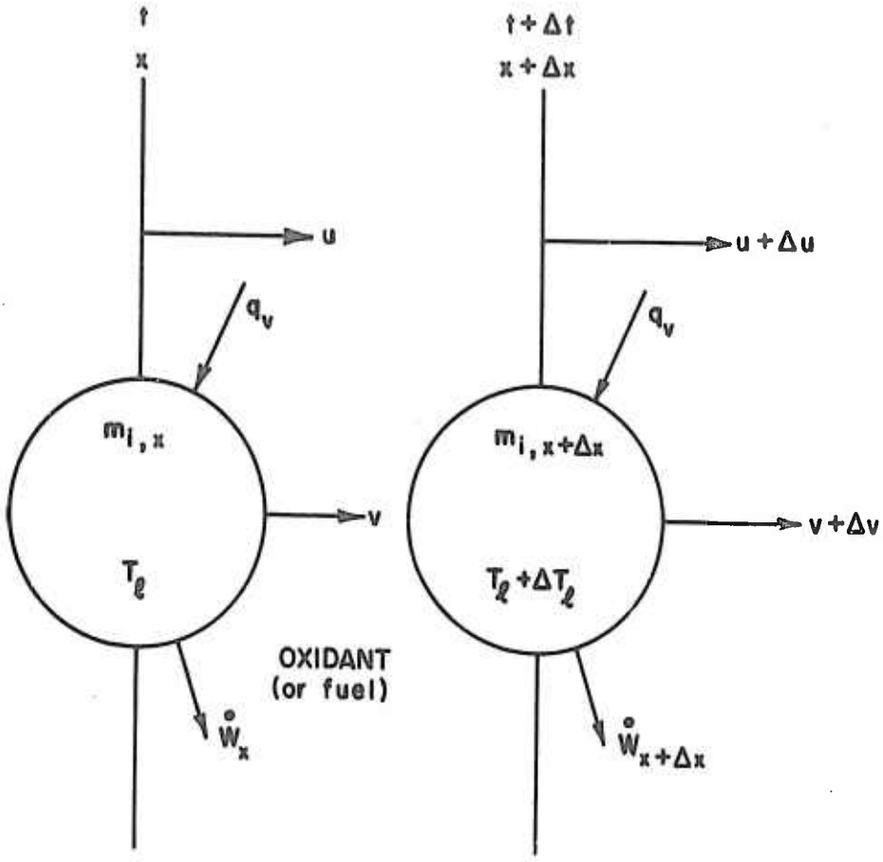

FIGURE 2.1 SCHEMATIC MODEL OF FUEL OR OXIDANT DROPS VAPORIZING IN ROCKET ENGINE

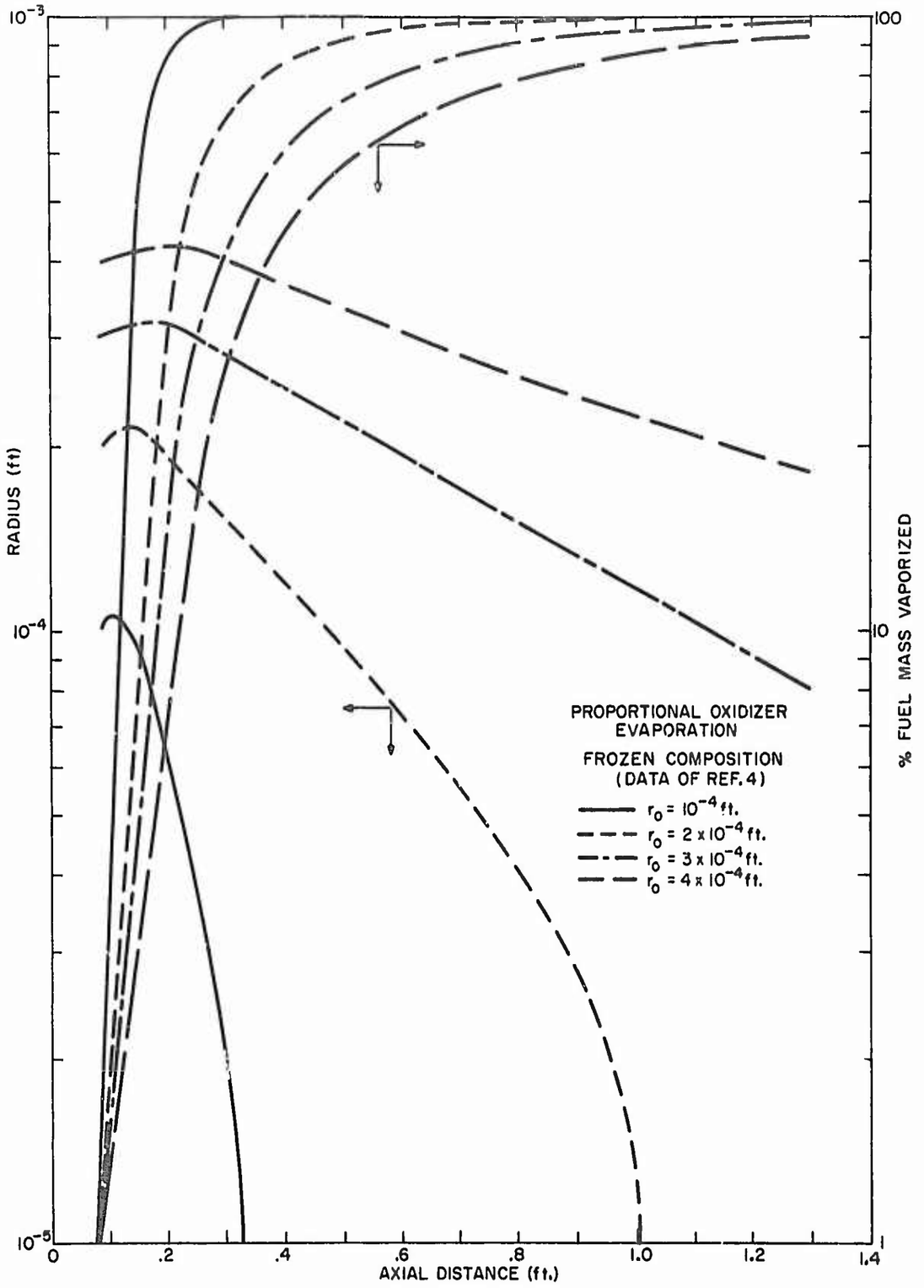

FIG. 2.2 FUEL DROP RADIUS AND % FUEL MASS VAPORIZED

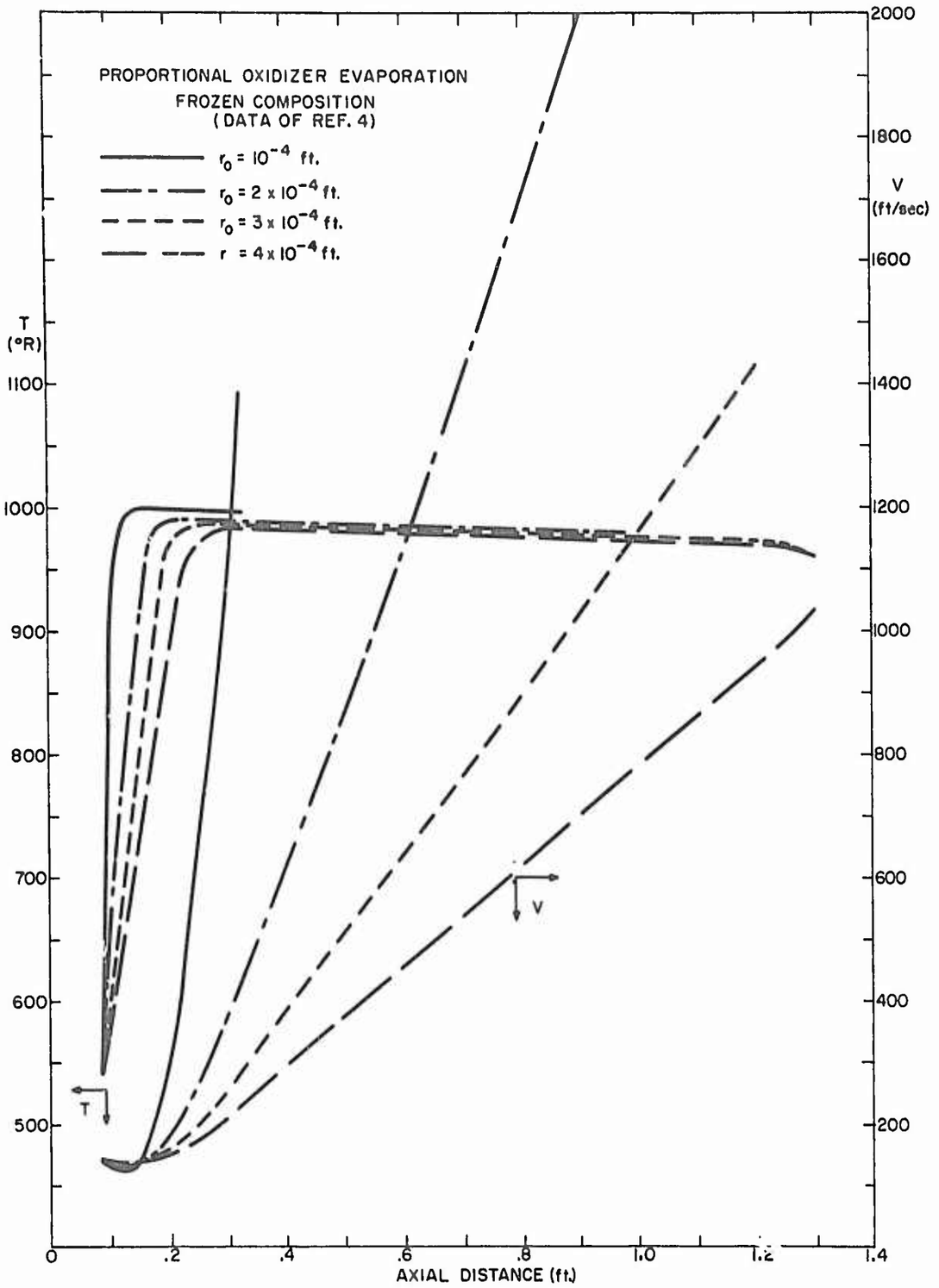

FIG. 2.3 FUEL DROP TEMPERATURE AND VELOCITY

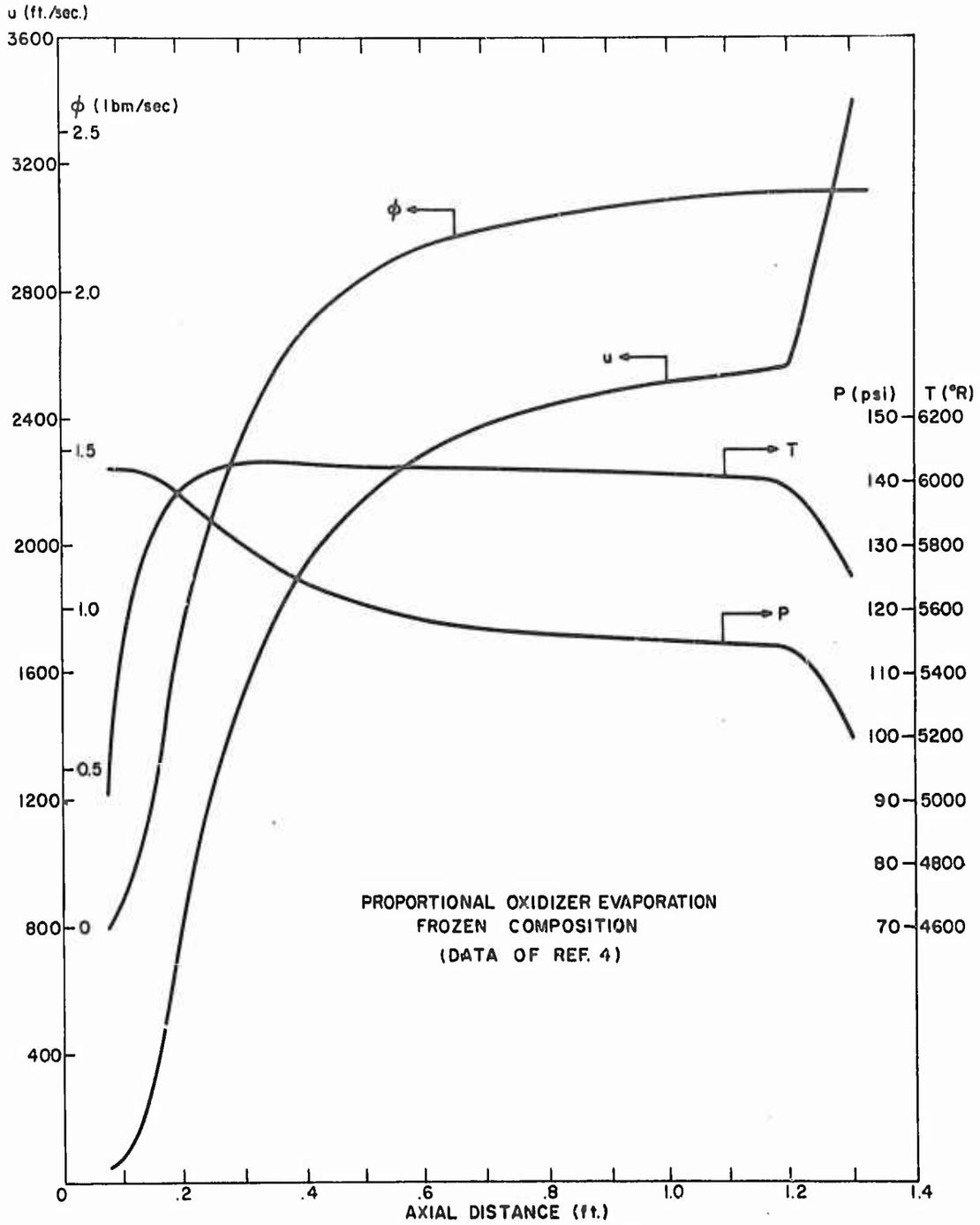

FIG. 2.4 COMBUSTION GAS PROPERTIES

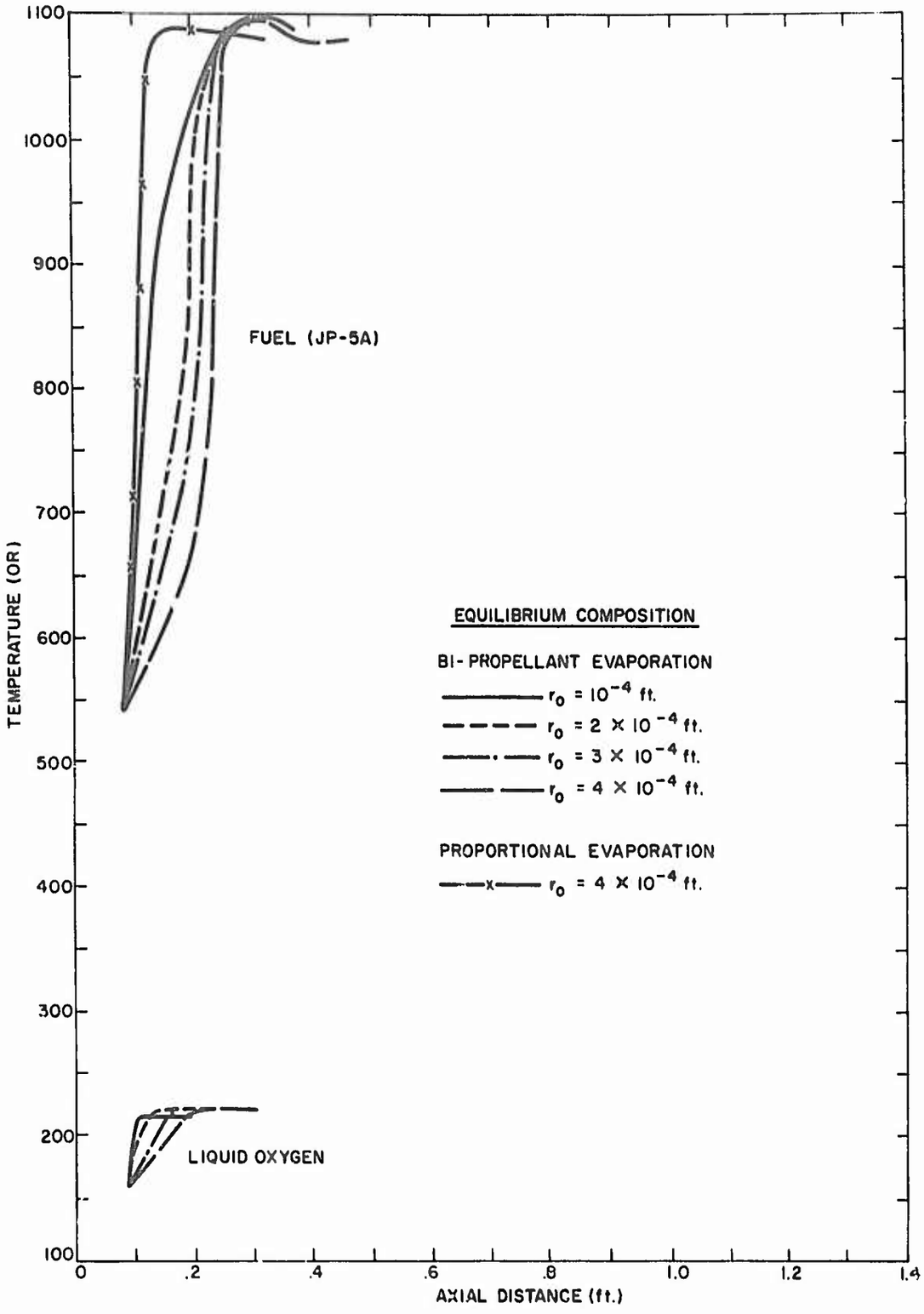

FIG. 2.5 DROP TEMPERATURE vs. DISTANCE

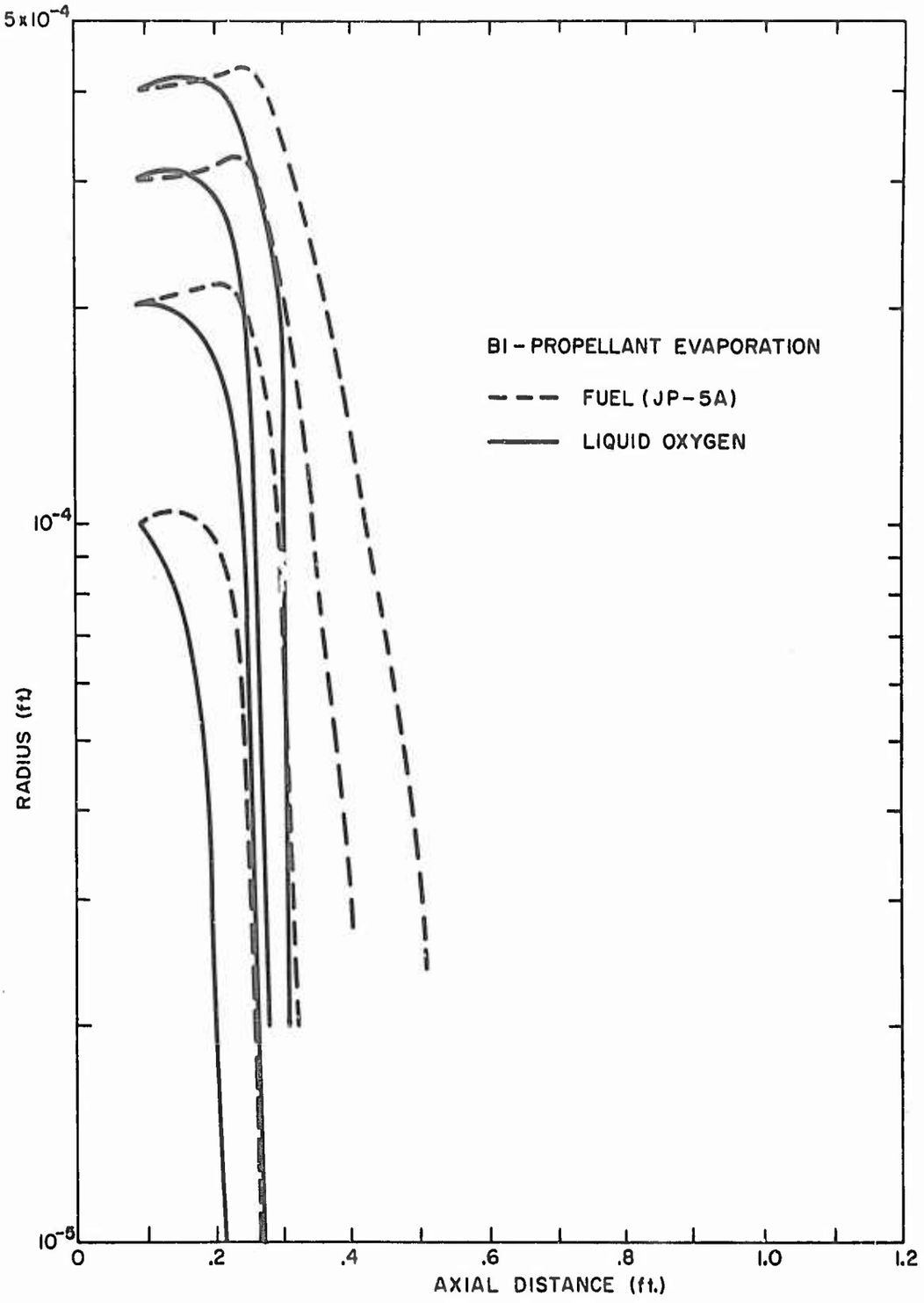

FIG.2.6 DROP RADIUS vs DISTANCE

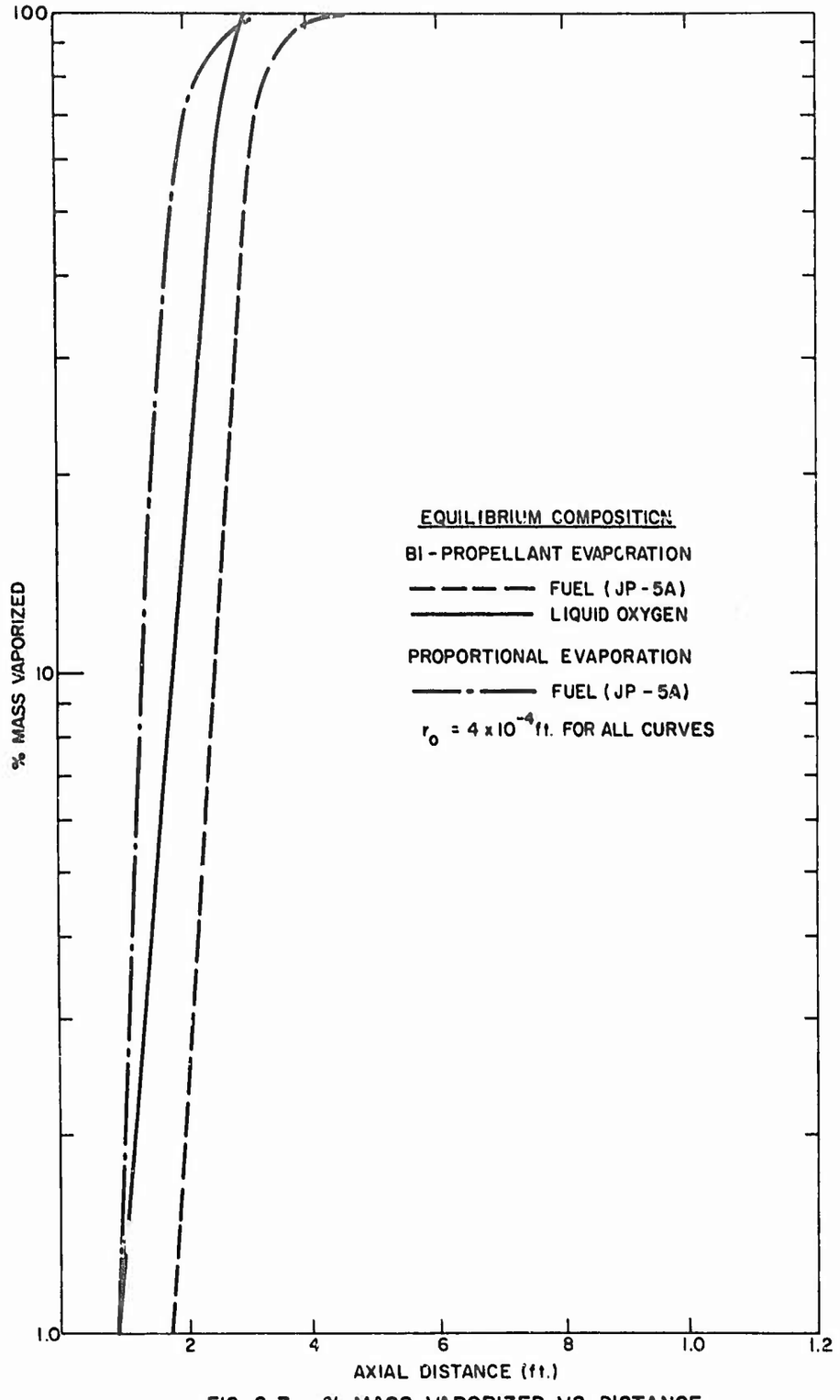

FIG. 2.7 % MASS VAPORIZED VS. DISTANCE

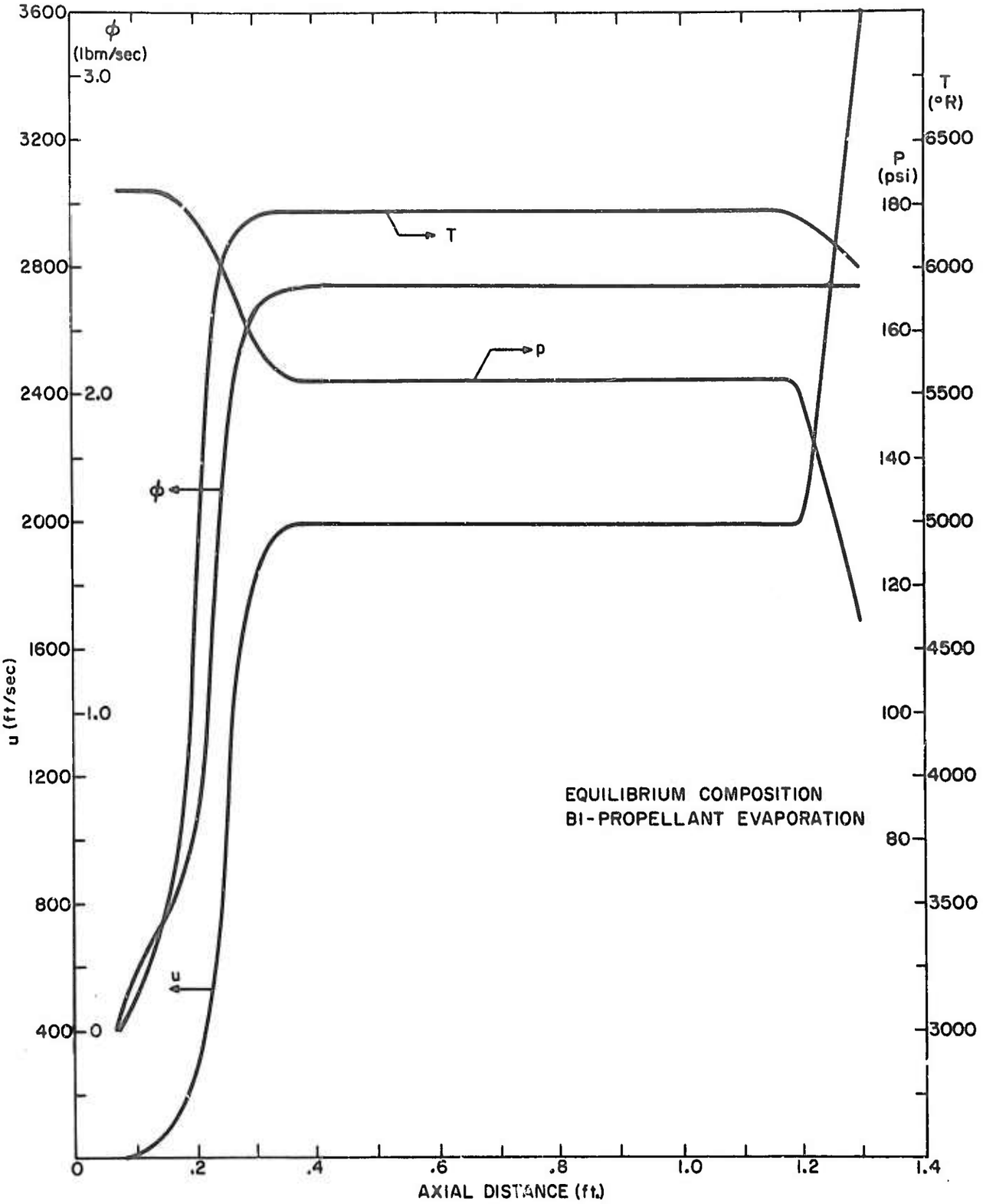

FIG. 2.8 COMBUSTION GAS PROPERTIES vs DISTANCE

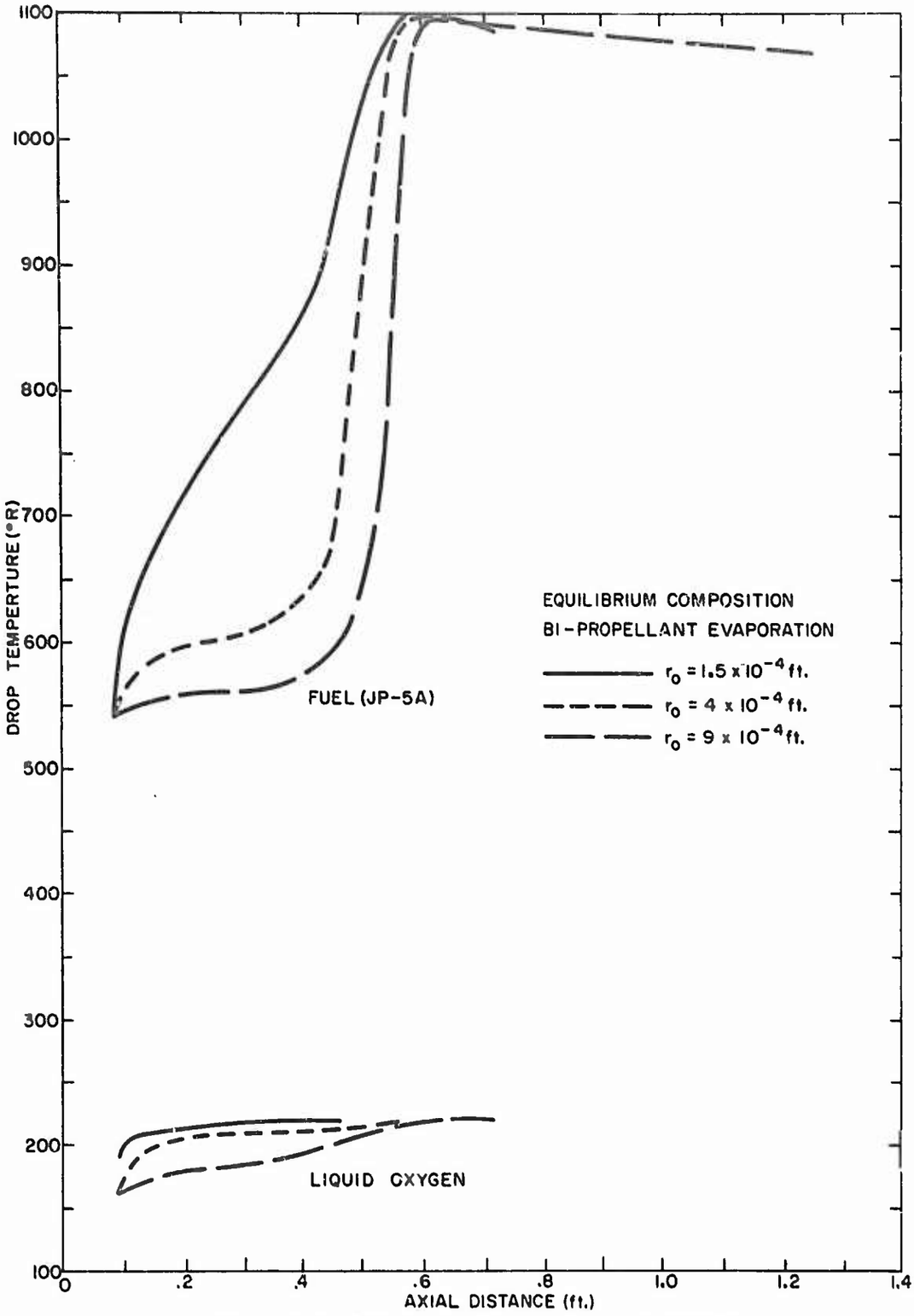

FIG.2.9 DROP TEMPERATURE vs AXIAL DISTANCE

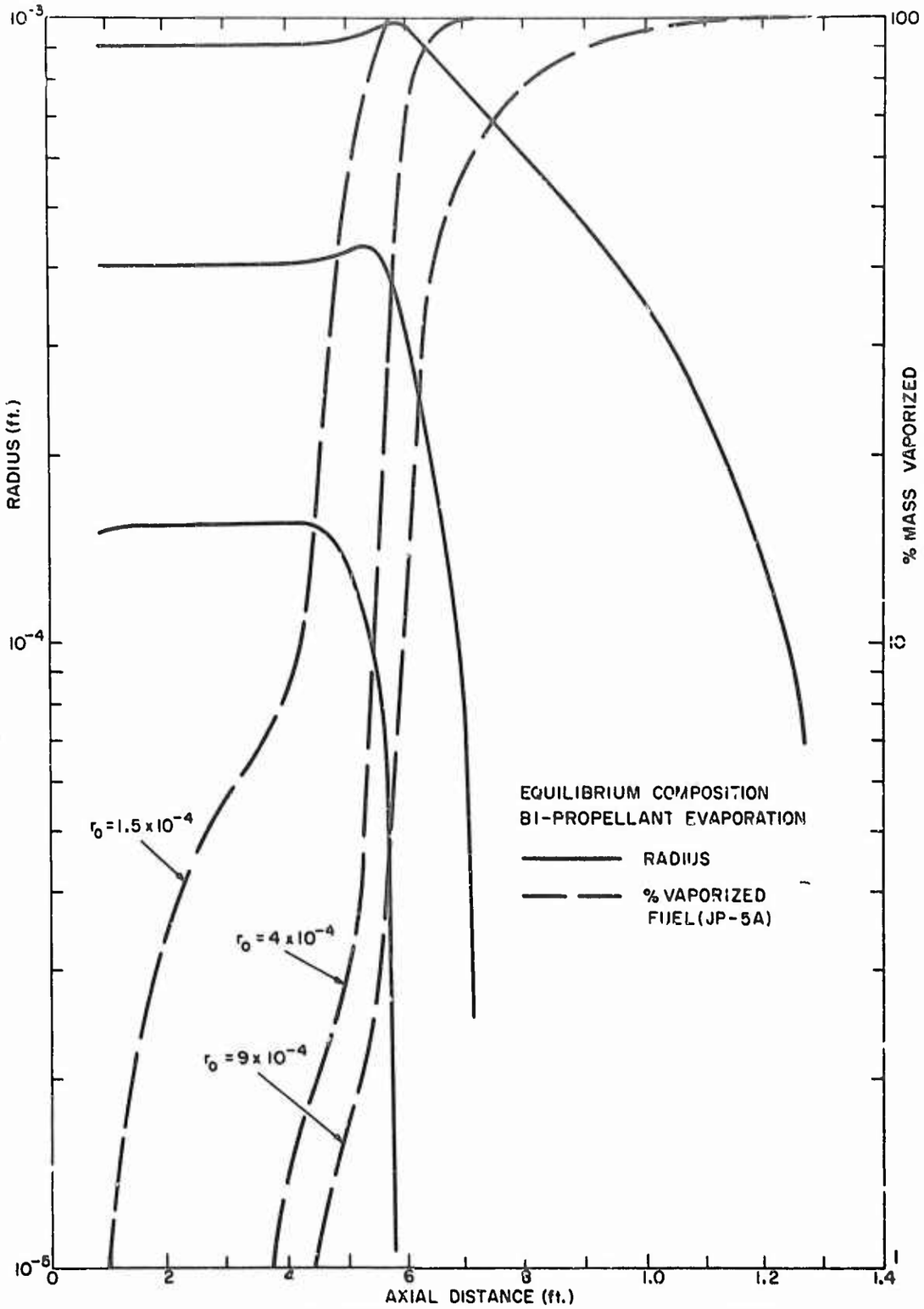

FIG. 2.10 FUEL DROP RADIUS AND PERCENT MASS VAPORIZED

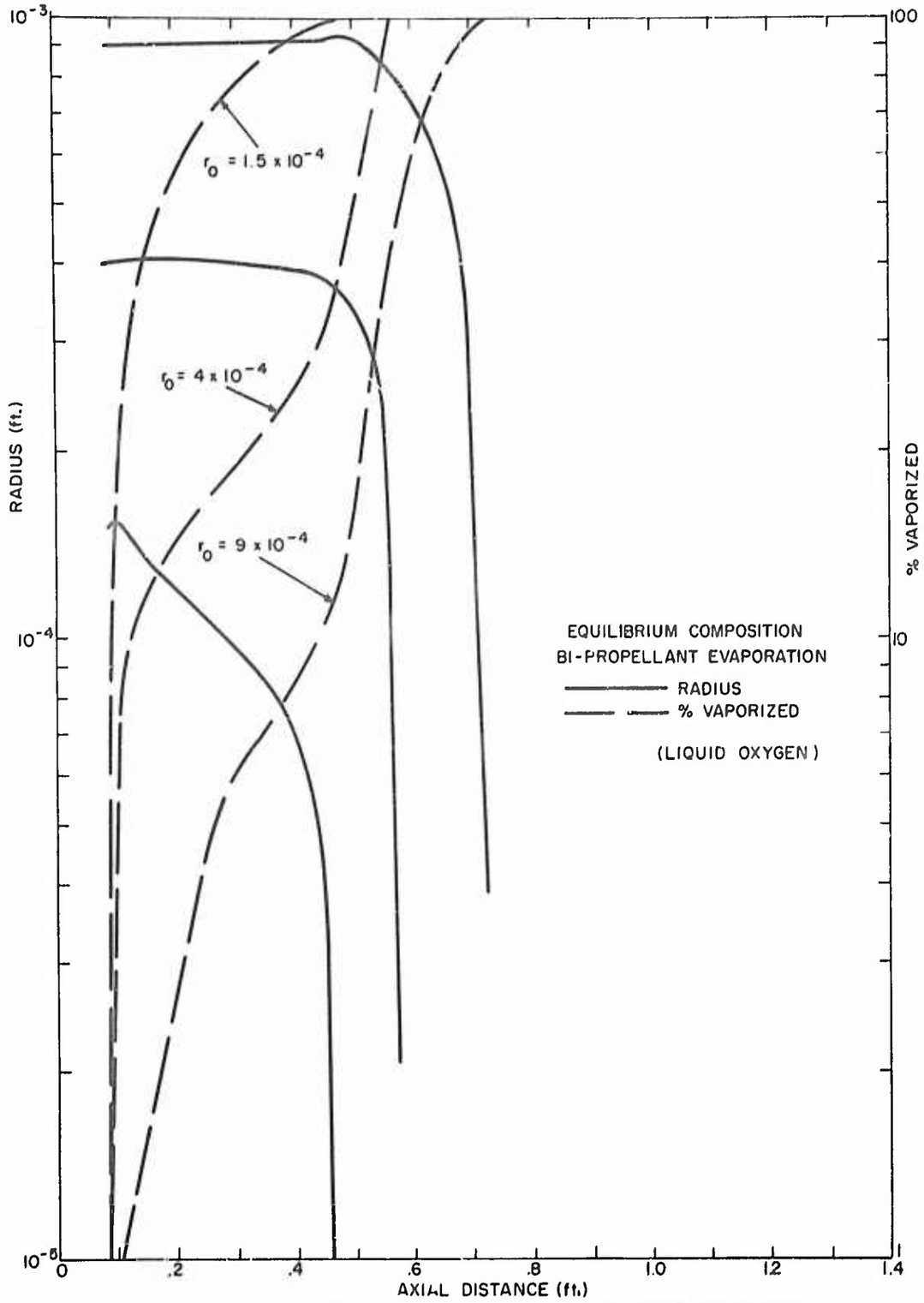

FIG. 2.11 OXIDIZER DROP RADIUS AND PERCENT VAPORIZED

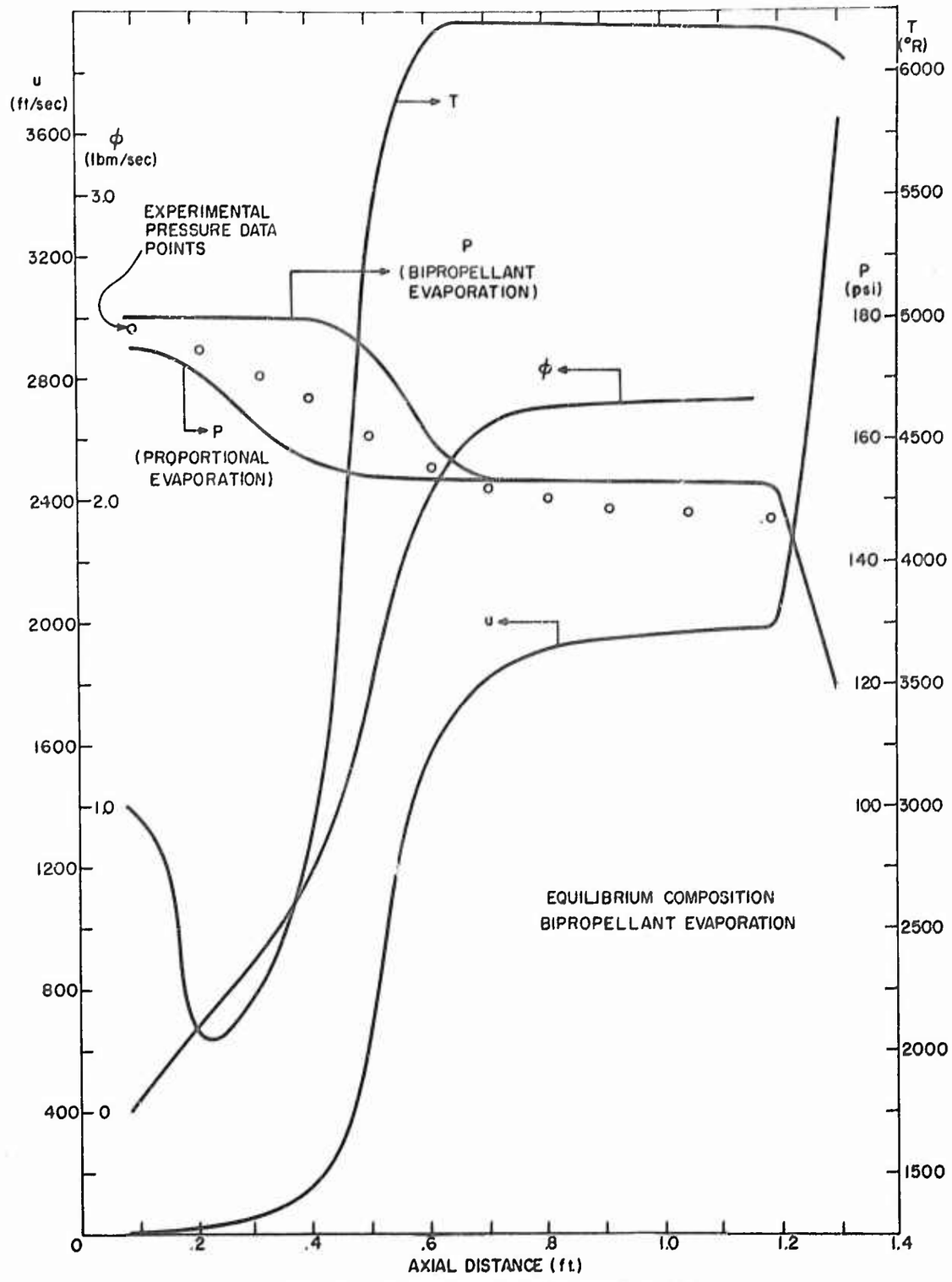

FIG. 2.12 COMBUSTION GAS PROPERTIES

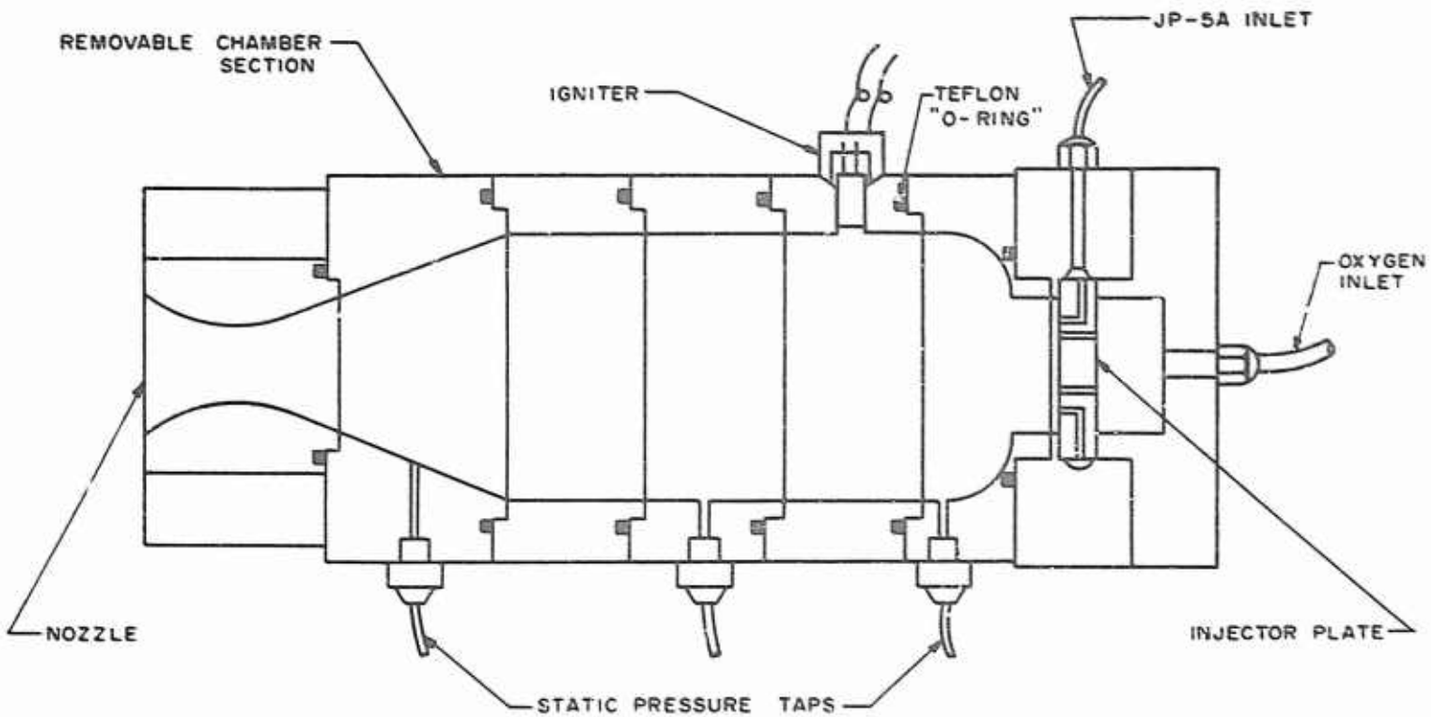

FIGURE 3.1 EXPERIMENTAL ROCKET ENGINE

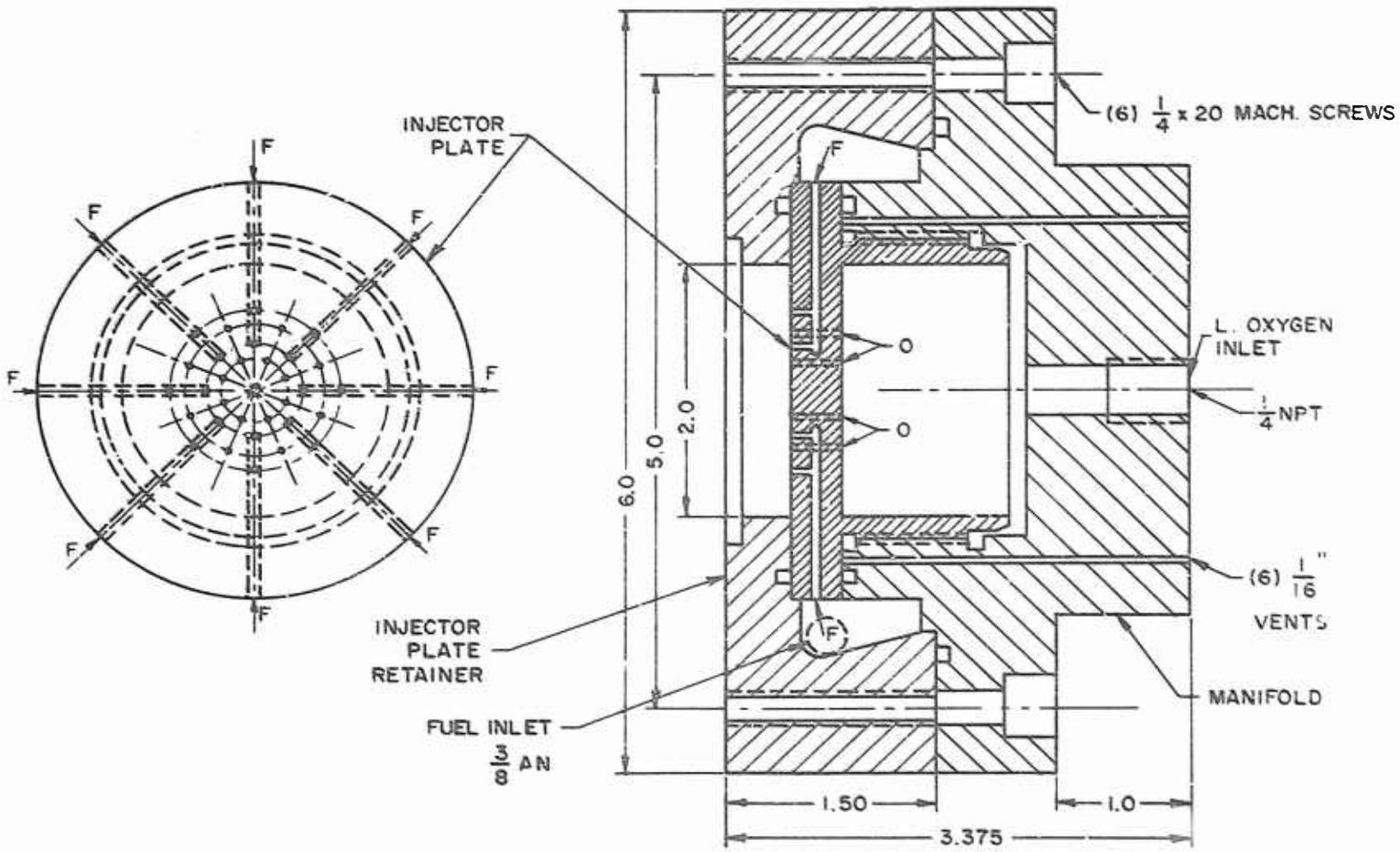

FIGURE 3.2 LIQUID PROPELLANT INJECTOR HEAD

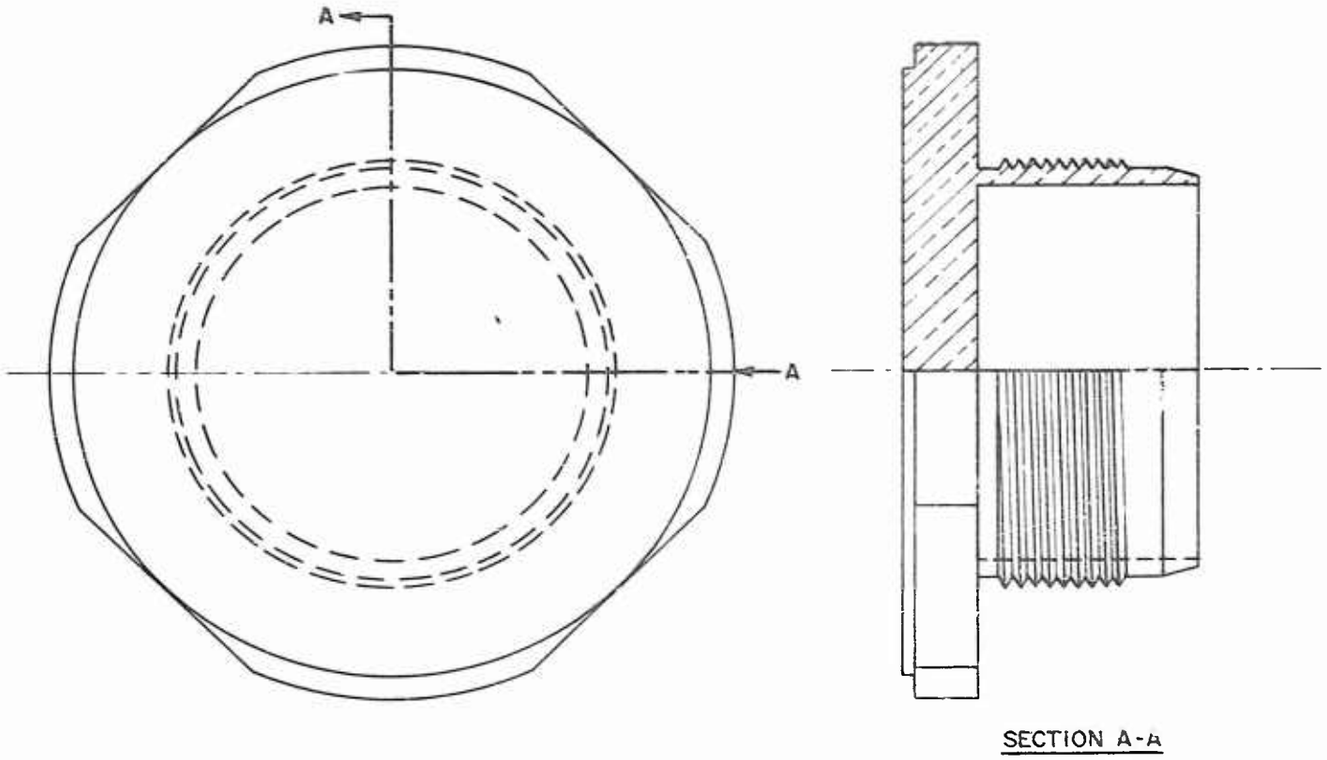

FIGURE 3.3 500 LBF INJECTOR PLATE BLANK

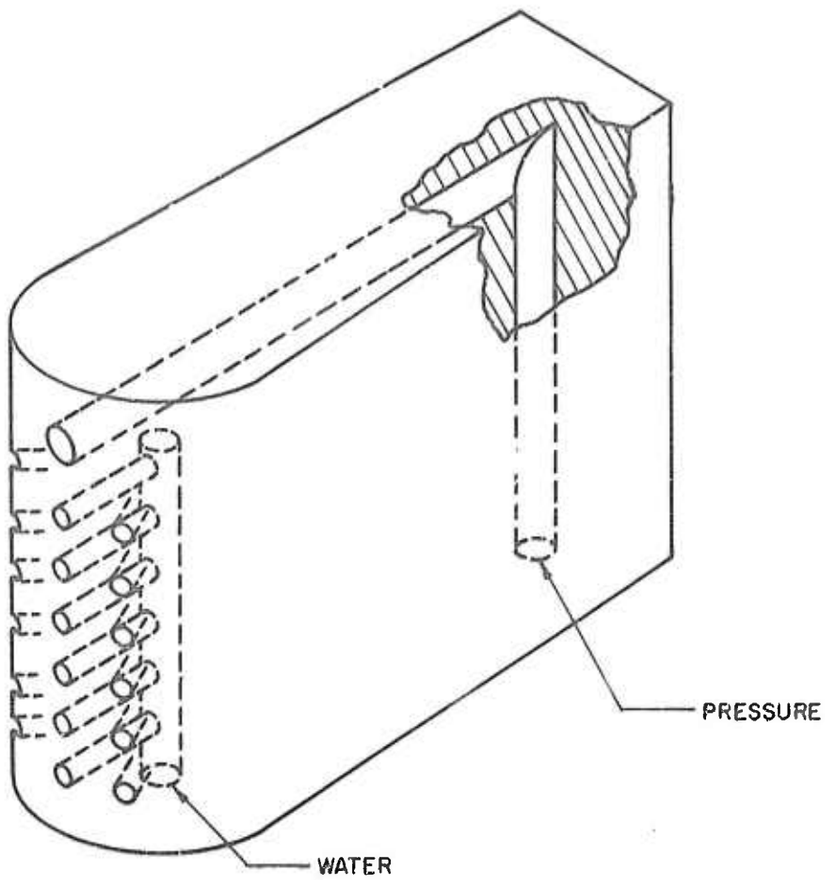

FIGURE 3.4 WATER COOLED GRAPHITE PROBE

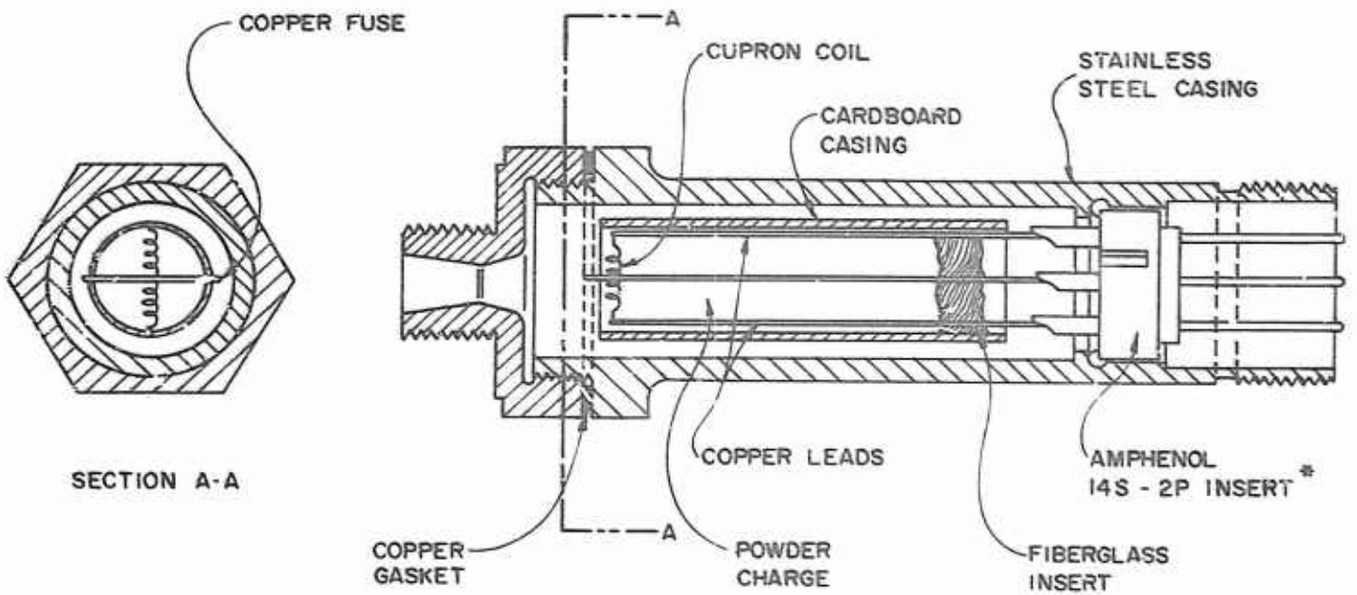

FIGURE 3.5 PYROTECHNIC IGNITER

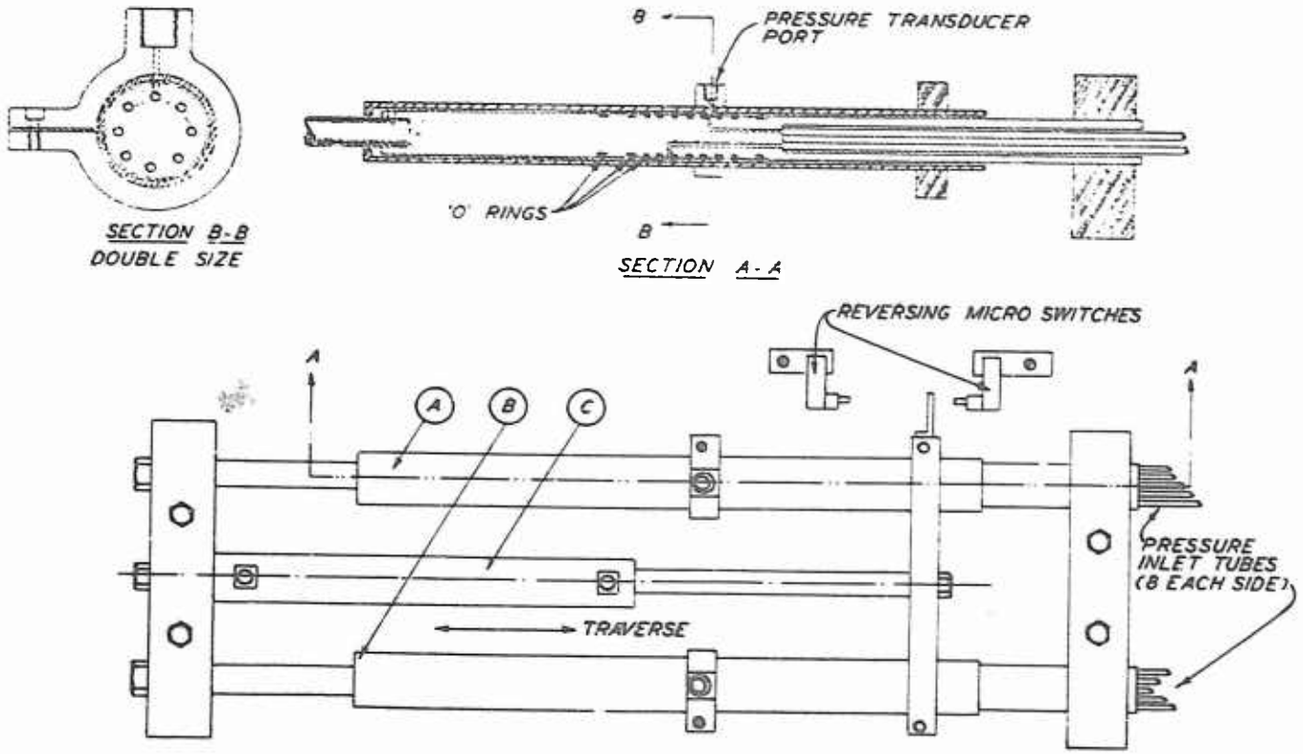

FIGURE 3.6 STATIC PRESSURE SCANNER

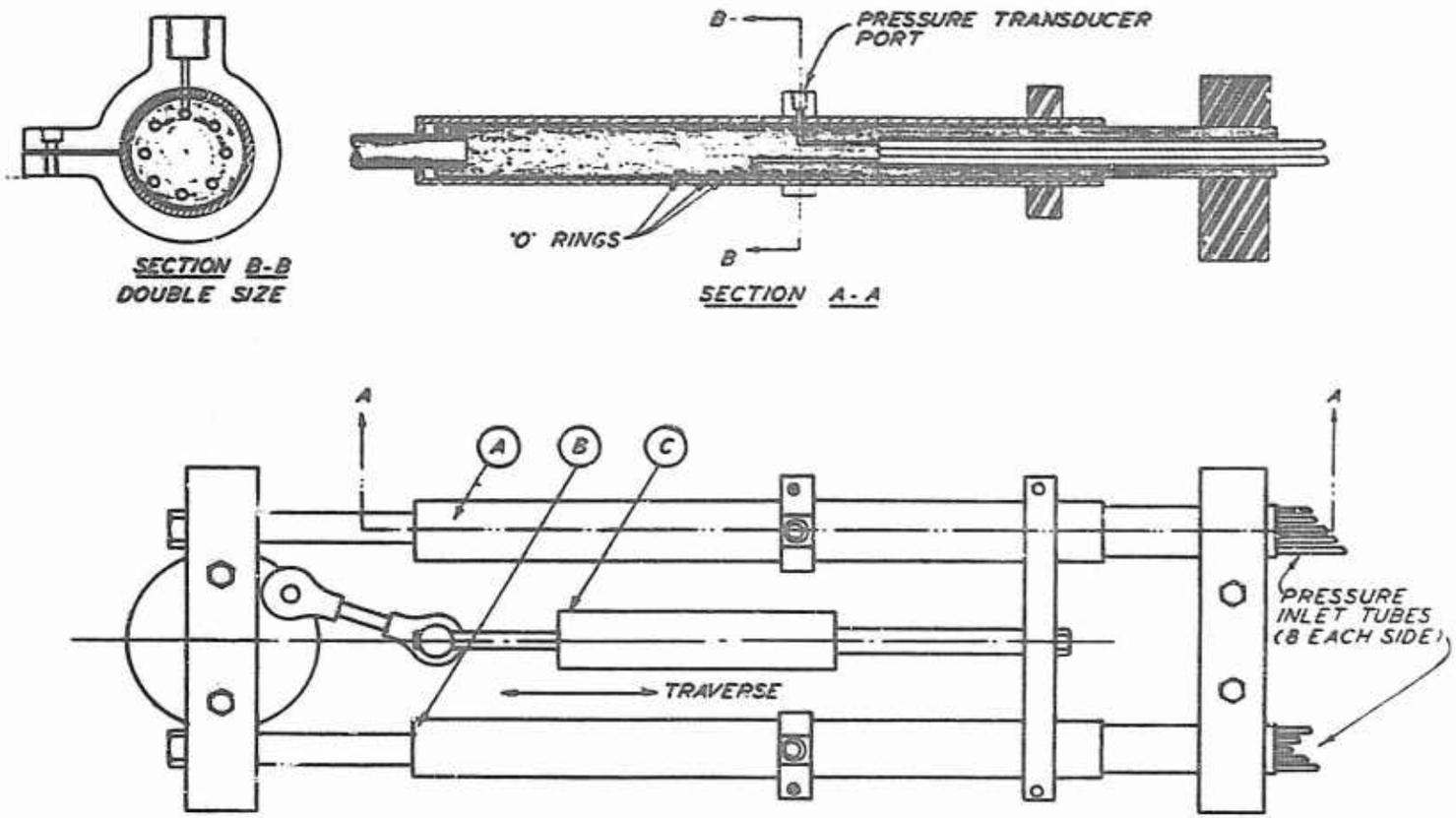

FIGURE 3.7 STATIC PRESSURE SCANNER

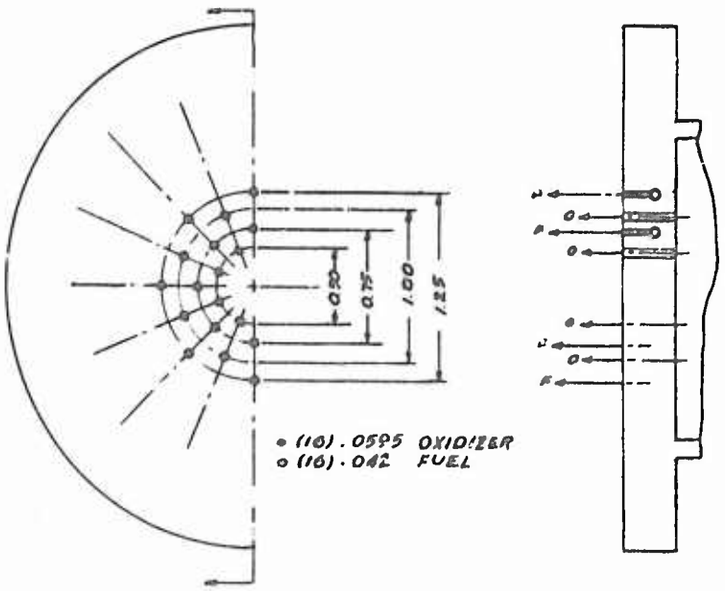

(a) INJECTOR 16/16 S(2)

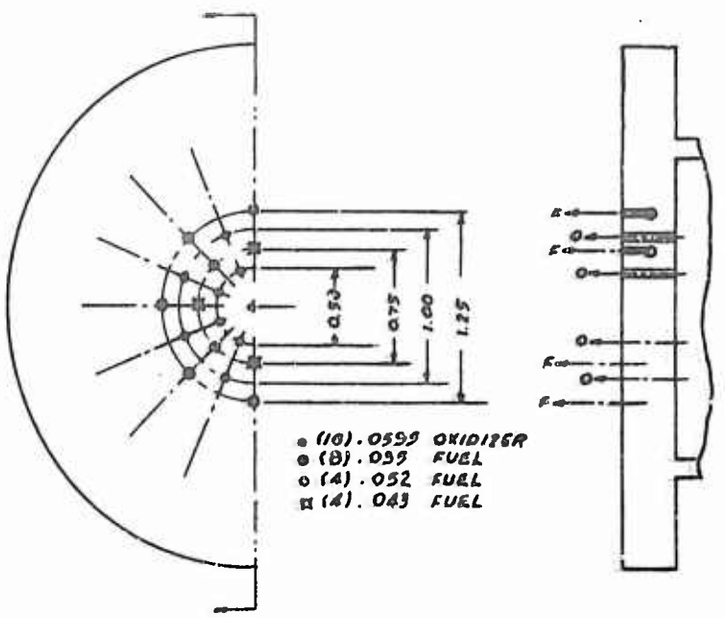

(b) INJECTOR 16/16 S(3)

FIGURE 4.1: LIQUID PROPELLANT INJECTOR CONFIGURATIONS - I

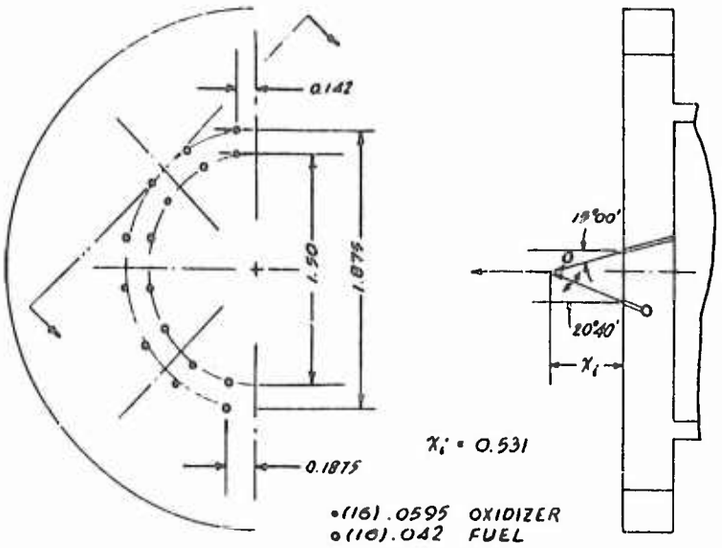

(a) INJECTOR 16/16 1(1)

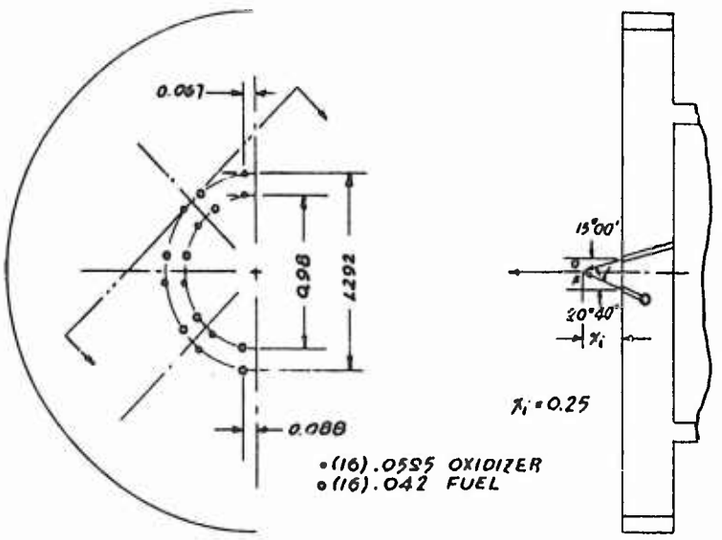

(b) INJECTOR 16/16 1(2)

FIGURE 4.1 : (cont'd) - II

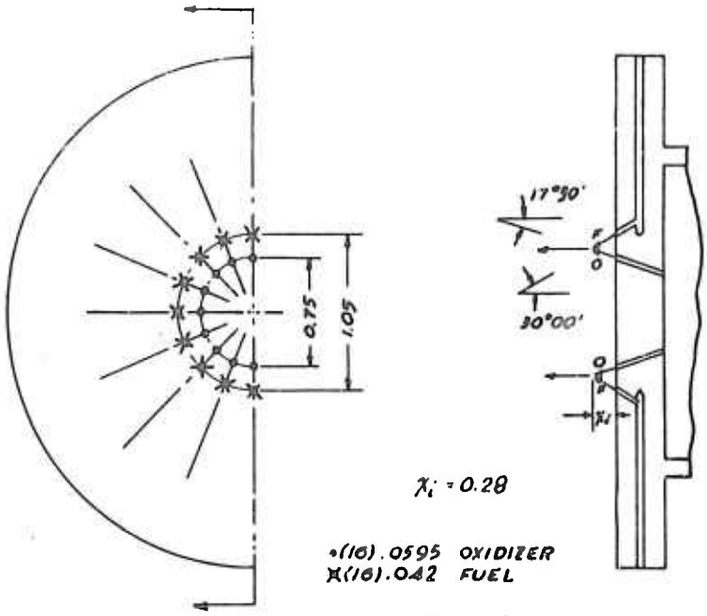

(a) INJECTOR 16/16 I (6)

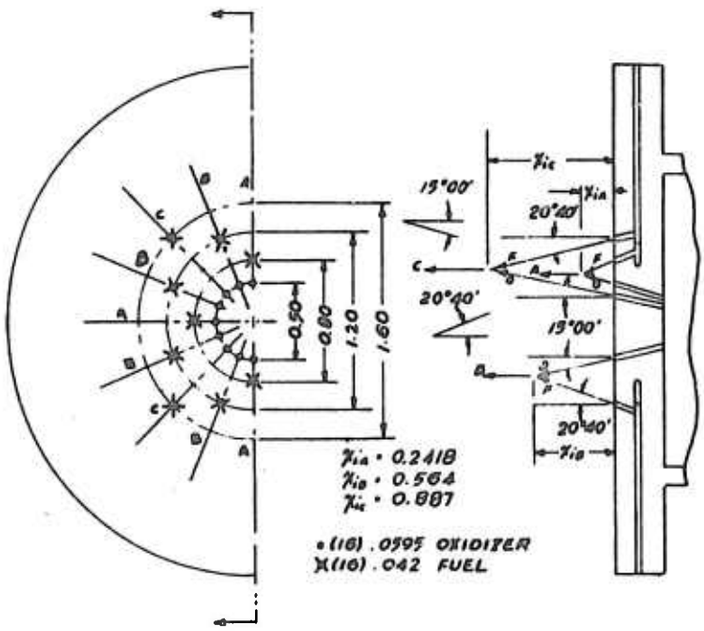

(b) INJECTOR 16/16 I (4)

FIGURE 4.1: (cont'd) - III

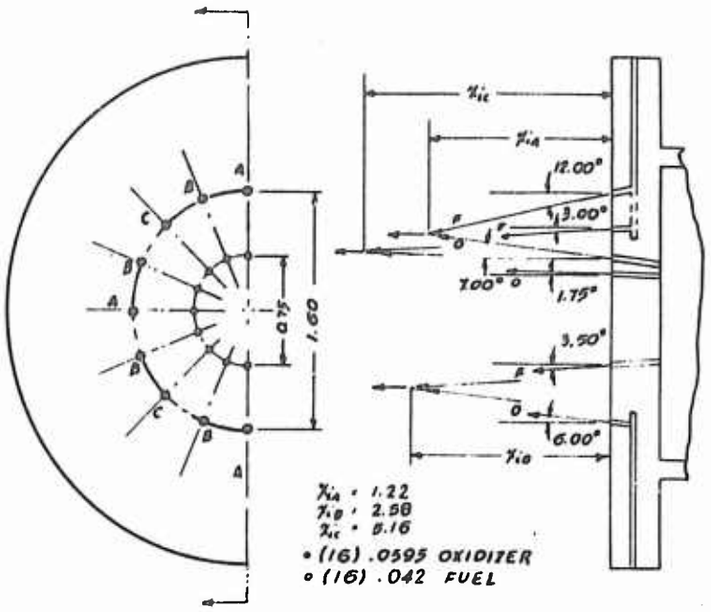

(a) INJECTOR 16/16 I (5)

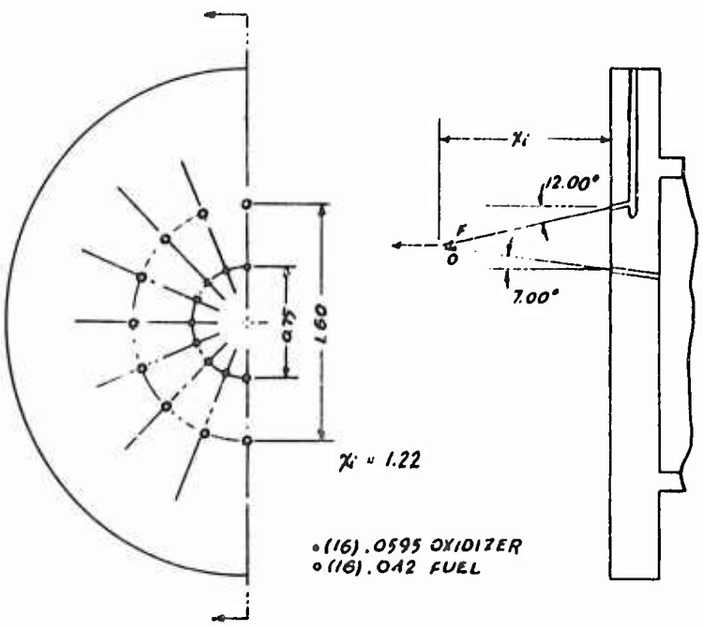

(b) INJECTOR 16/16 I (7)

FIGURE 4.1: (cont'd) - IV

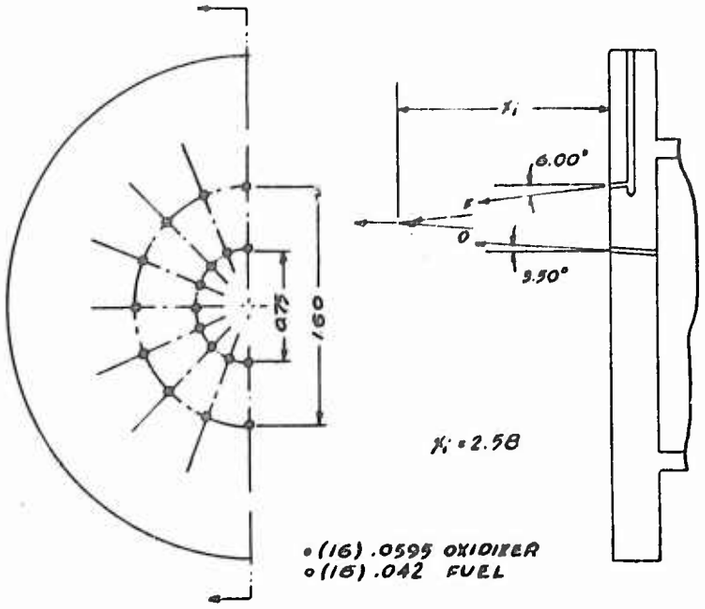

(a) INJECTOR 16/16 I (8)

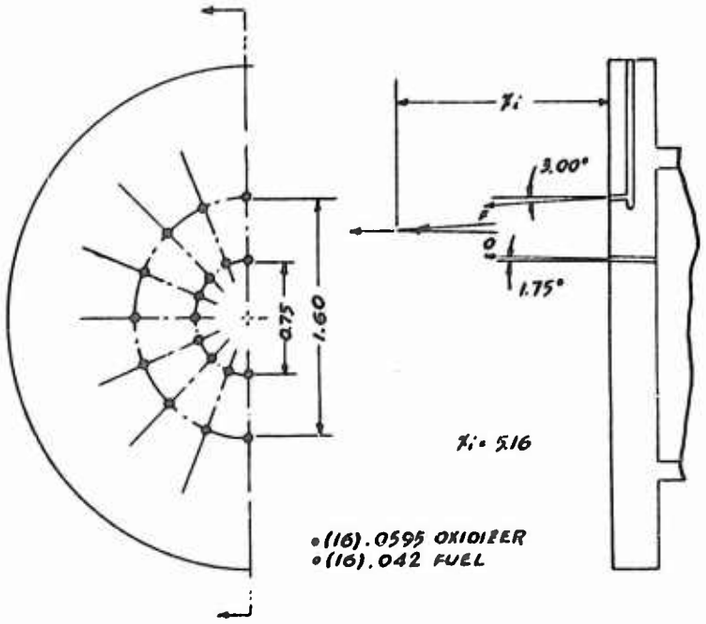

(b) INJECTOR 16/16 I (9)

FIGURE 4.1: (concl d) - V

INJECTOR NR.[1]	n_o	n_f	D_o IN.	D_f IN.	α_o[2] DEG.	α_f[2] DEG.	$(\frac{L}{D})_o$[3]	$(\frac{L}{D})_f$[3]	X_i IN.
16/16 S2	16	16	.0595	.042	0	0	6.30	4.465	∞
16/16 S3	16	8	.0595	.035	0	0	6.30	5.36	∞
		4		.052		0		3.61	
		4		.043		0		4.37	
16/16 I1	16	16	.0595	.042	15.00	20.67	6.53	4.77	0.531
16/16 I2	16	16	.0595	.042	15.00	20.67	6.53	4.77	0.25
16/16 I4	4	4	.0595	.042	15.00	20.67	6.53	4.77	0.242
	8	8	.0595	.042	15.00	20.67	6.53	4.77	0.564
	4	4	.0595	.042	15.00	20.67	6.53	4.77	0.887
16/16 I5	4	4	.0595	.042	7.00	12.00	6.35	4.57	1.22
	8	8	.0595	.042	3.50	6.00	6.32	4.49	2.58
	4	4	.0595	.042	1.75	3.00	6.303	4.47	5.16
16/16 I6	16	16	.0595	.042	17.50	30.00	6.61	5.16	0.28
16/16 I7	16	16	.0595	.042	7.00	12.00	6.35	4.57	1.22
16/16 I8	16	16	.0595	.042	3.50	6.00	6.32	4.49	2.58
16/16 I9	16	16	.0595	.042	1.75	3.00	6.303	4.47	5.16

(1) S = SHOWERHEAD ; I = IMPINGING
(2) FOR RESULTANT STREAM TO BE AXIAL.
(3) LENGTH/DIAMETER RATIO OF ORIFICE

n = NUMBER OF ORIFICES
D = ORIFICE DIAMETER
α = INJECTION ANGLE
X_i = IMPINGEMENT DISTANCE

SUBSCRIPTS:
o = OXIDIZER
f = FUEL

FIGURE 4.2 INJECTOR SUMMARY: GEOMETRY

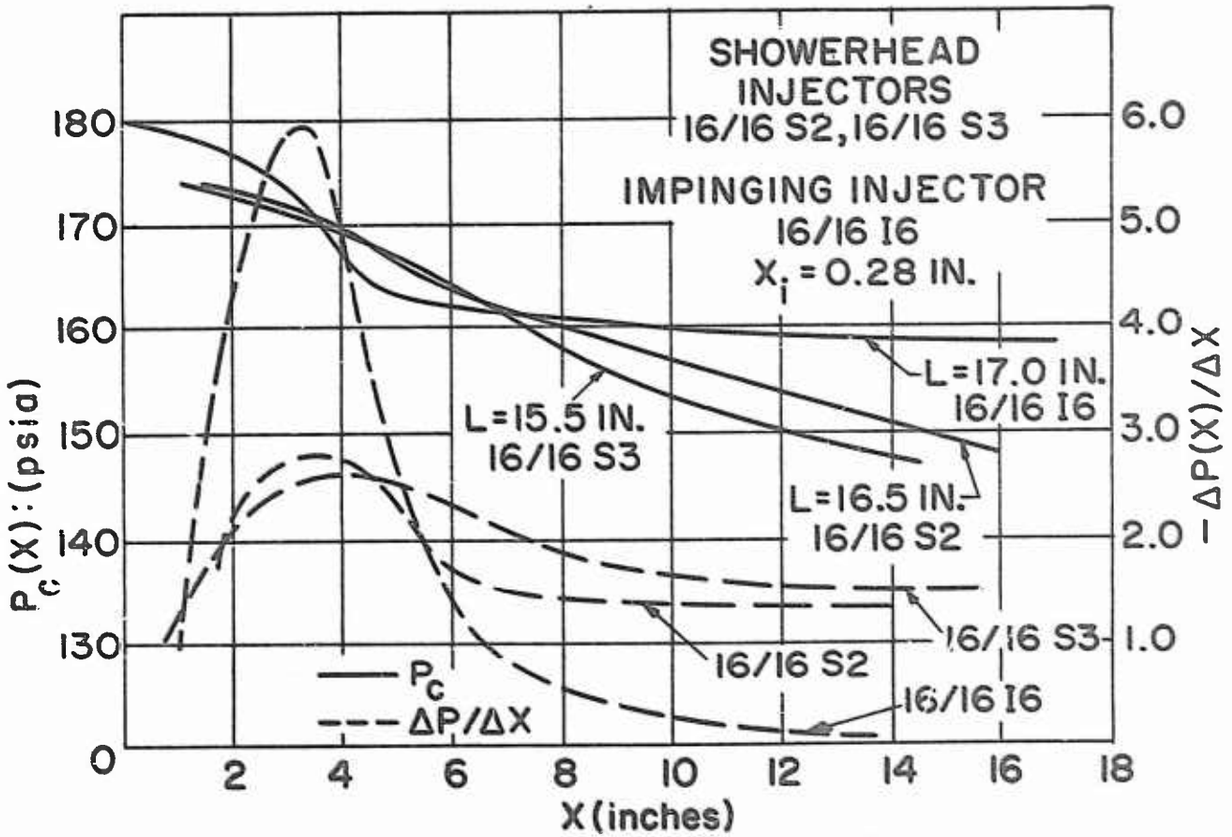

FIGURE 4.3 AXIAL PRESSURE VARIATION AND GRADIENT

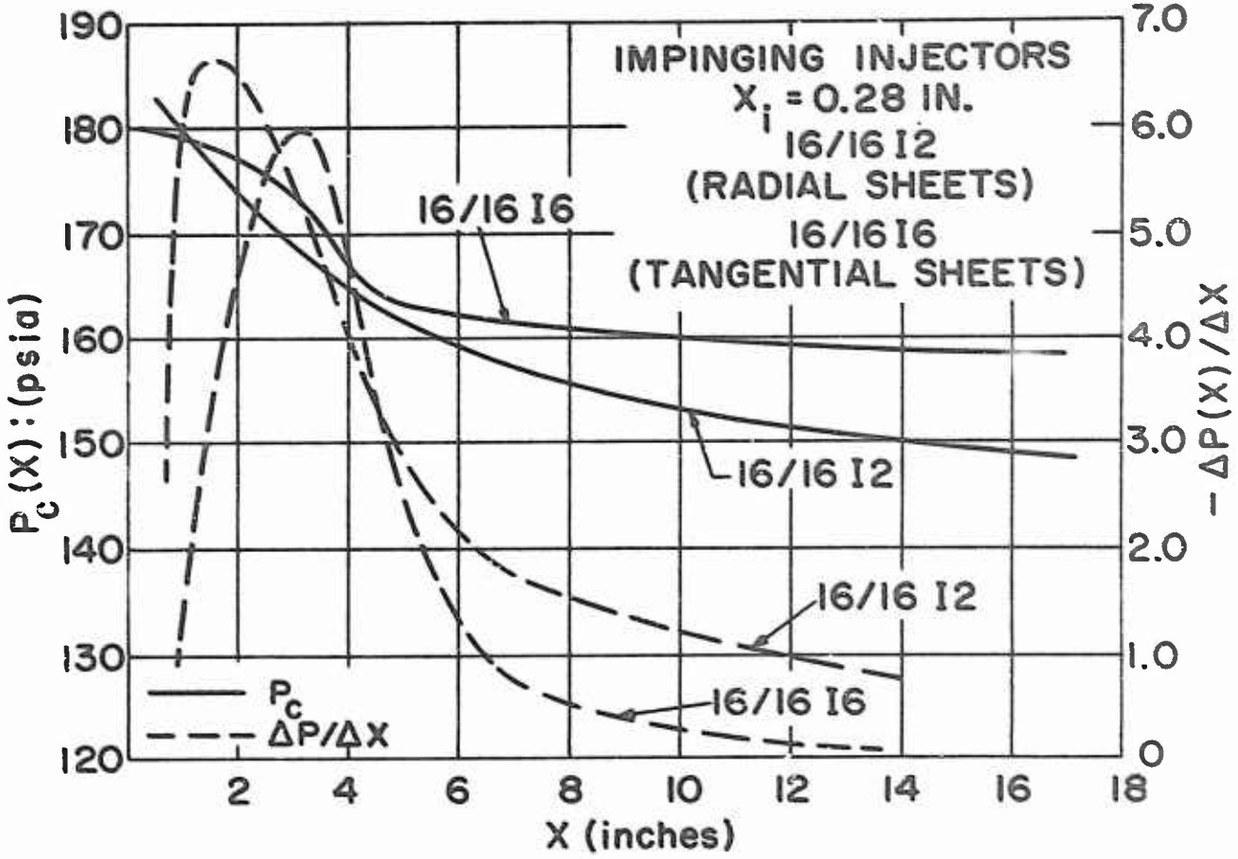

FIGURE 4.4 AXIAL PRESSURE VARIATION AND GRADIENT

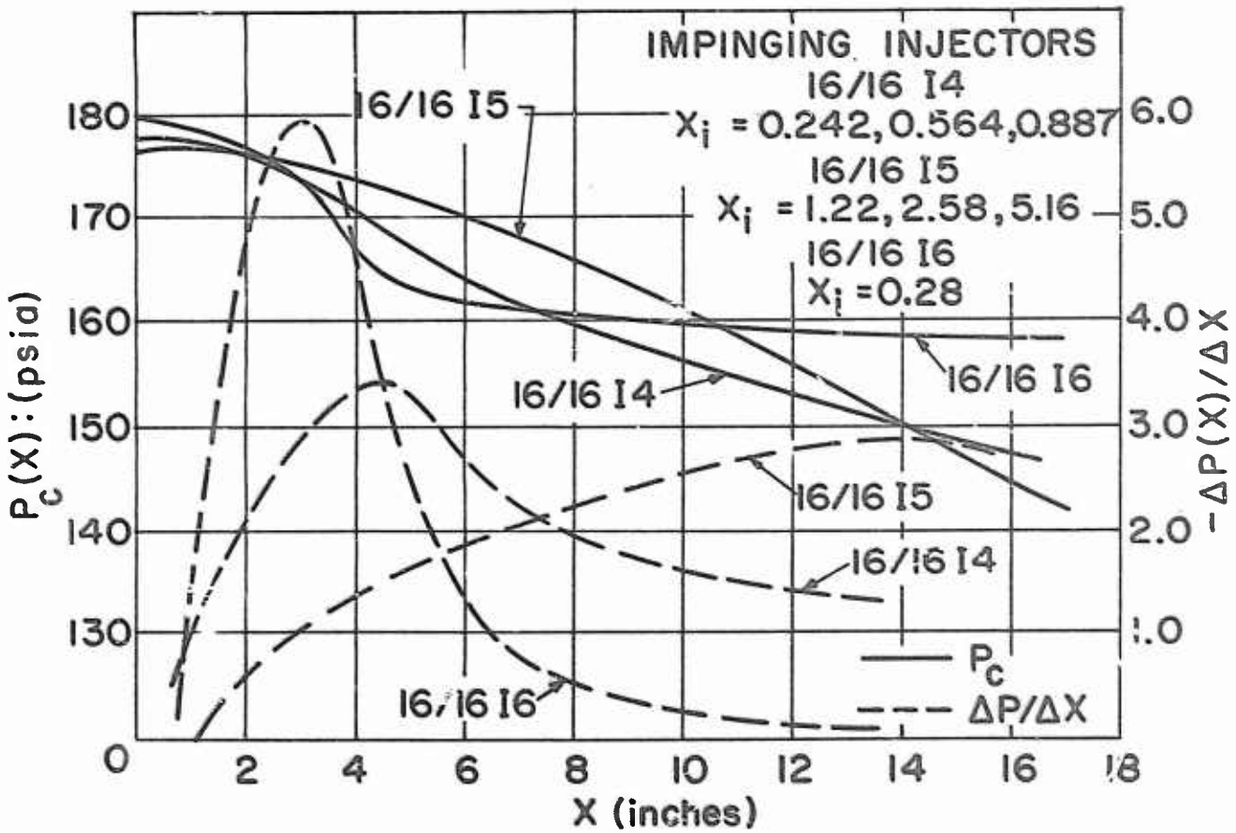

FIGURE 4.5 AXIAL PRESSURE VARIATION AND GRADIENT

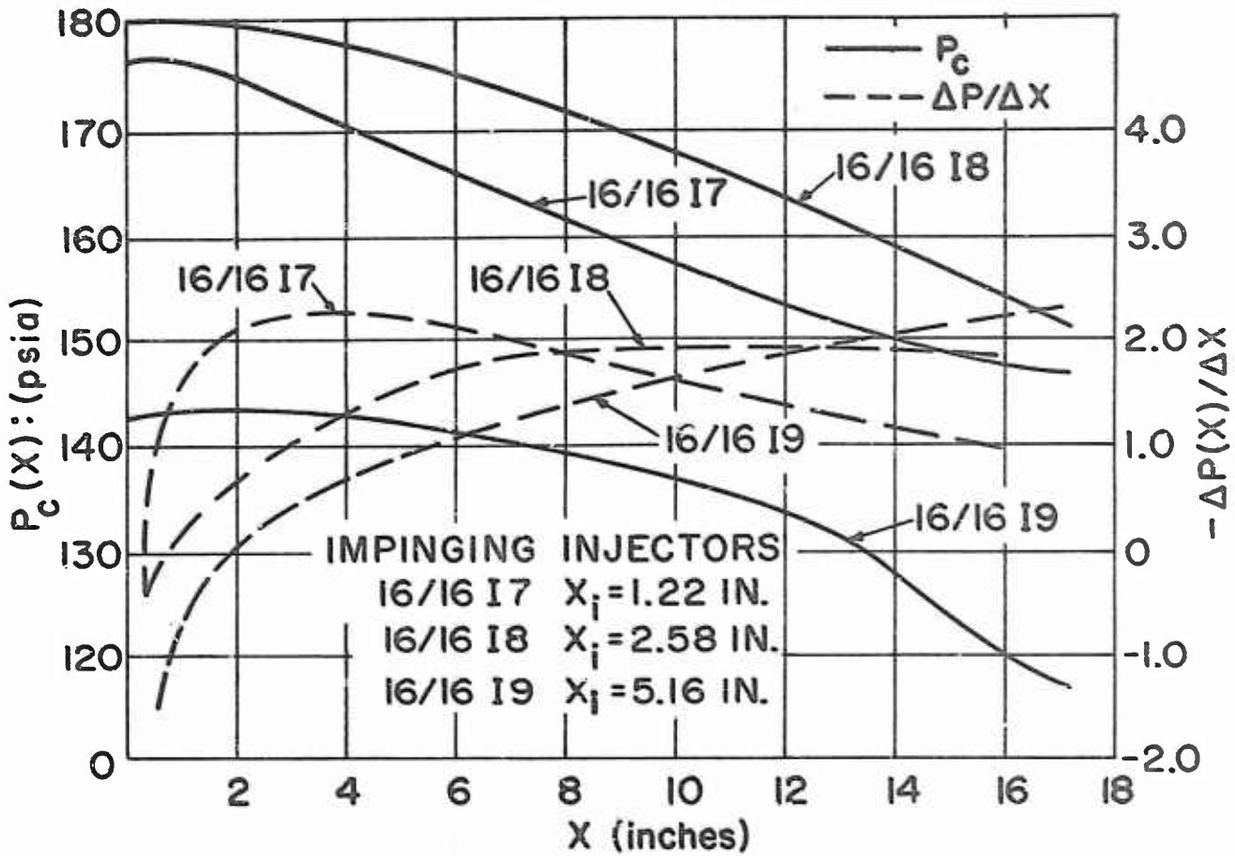

FIGURE 4.6 AXIAL PRESSURE VARIATION AND GRADIENT

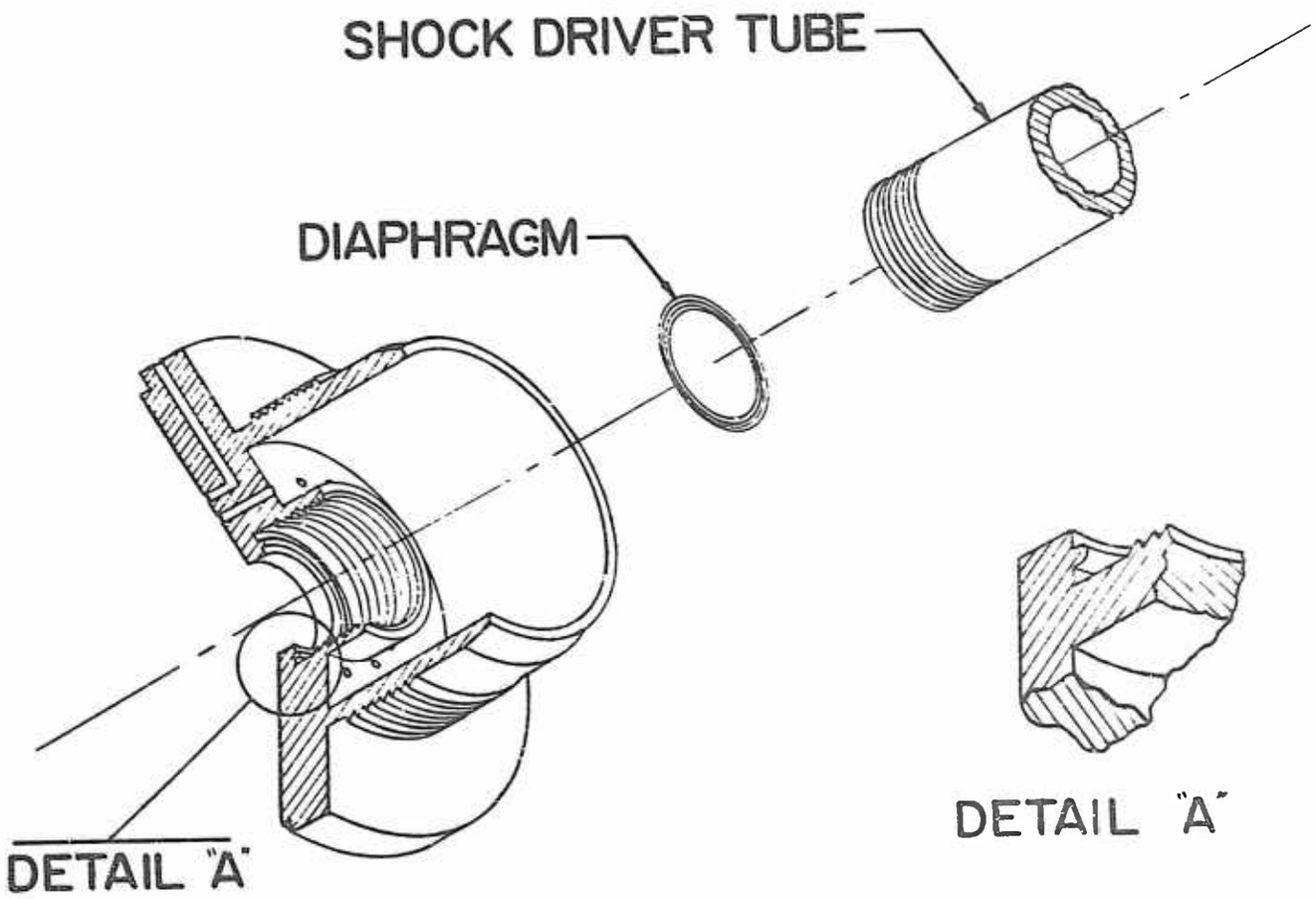

FIGURE 4.7 DETAIL OF INJECTOR - DIAPHRAGM - SHOCK TUBE INTERFACE

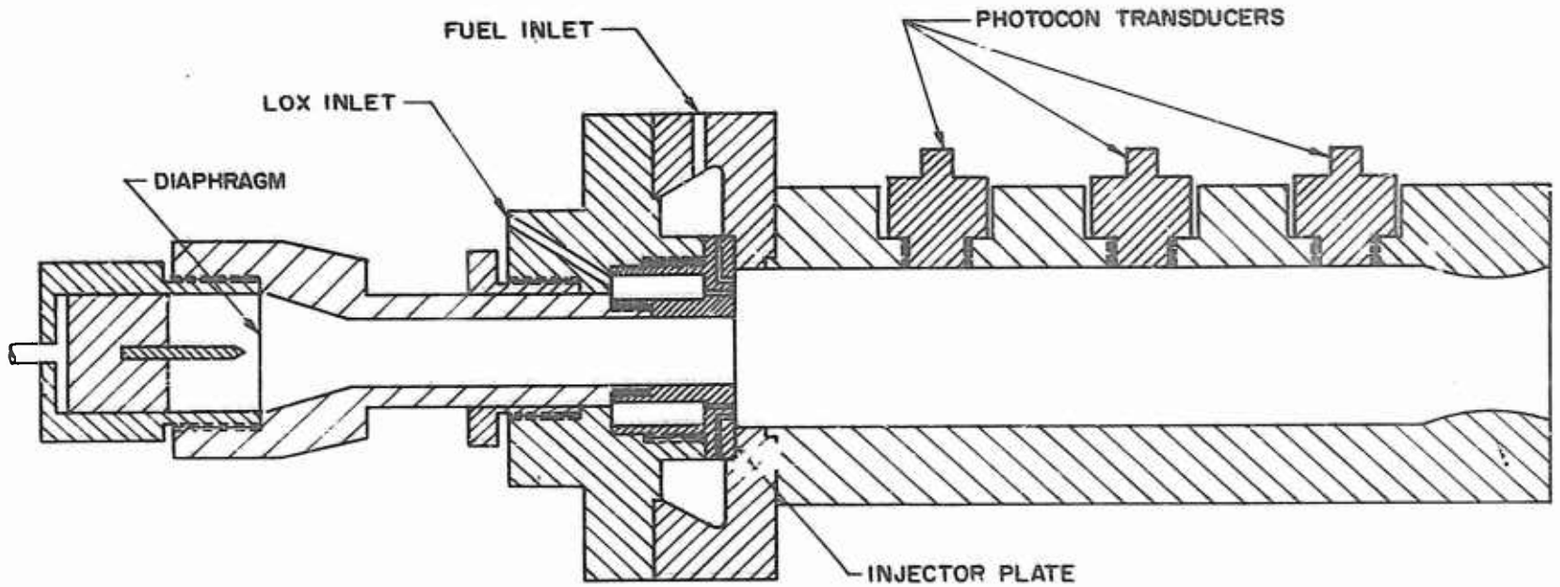

FIGURE 4.8 SCHEMATIC OF THRUST CHAMBER AND WAVE GENERATOR

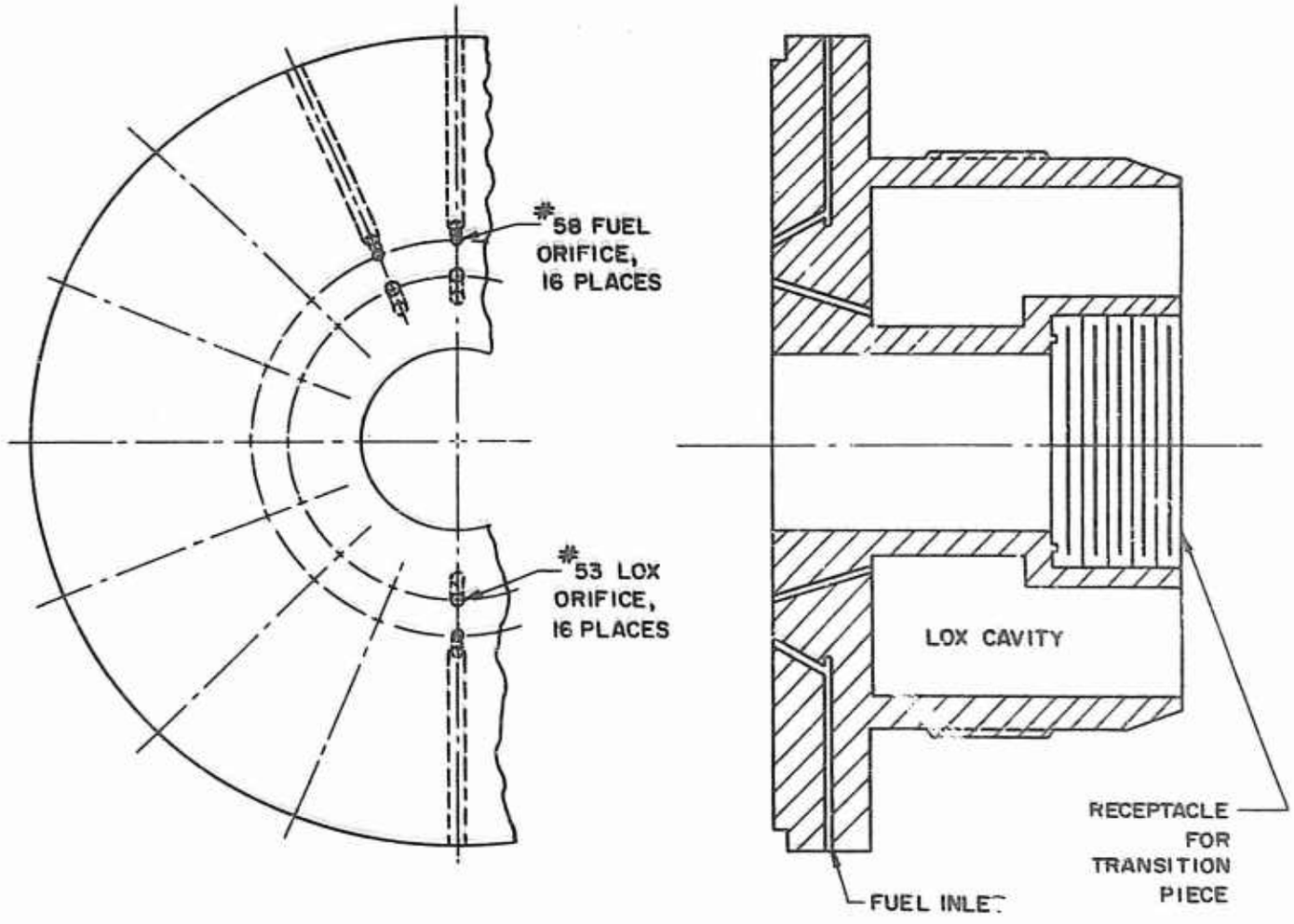

FIGURE 4.9 IMPINGING INJECTOR FOR WAVE PROPAGATION EXPERIMENTS

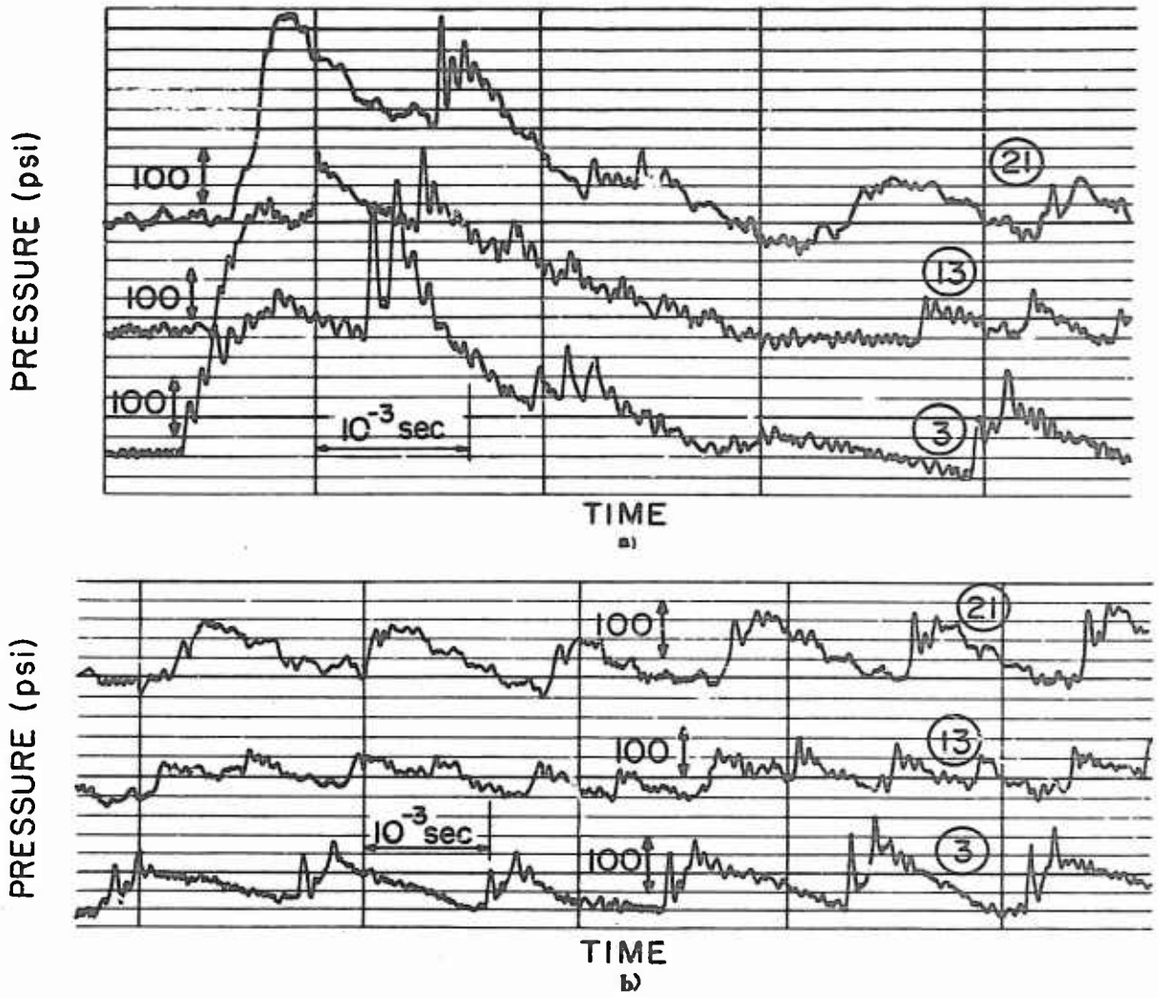

FIGURE 4.10 PRESSURE TIME TRACE DURING A ROCKET FIRING

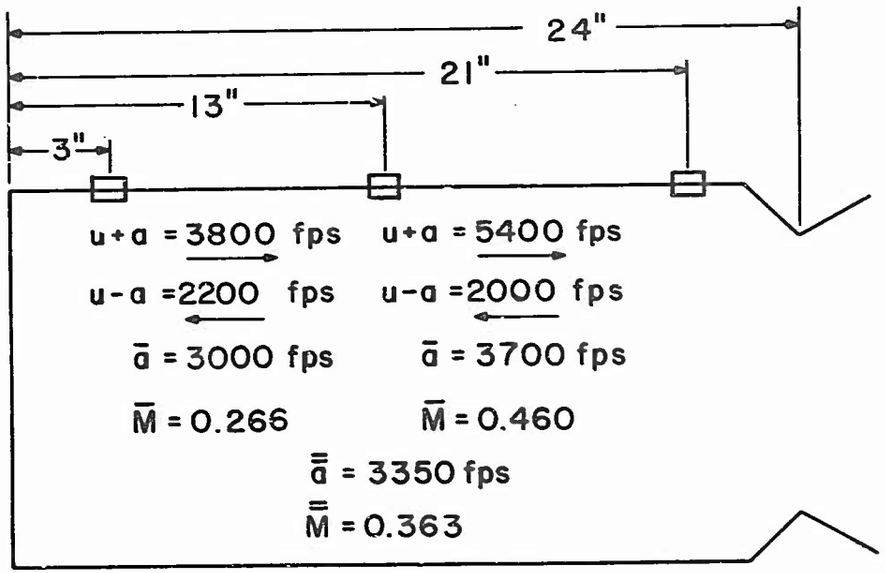

TEST No. 374
TEST No. 323

$\bar{\bar{a}} = 3350$, $\bar{\bar{M}} = 0.367$ } OBTAINED FROM FREQUENCY MEASUREMENTS

FIGURE 4.11 AVERAGE SONIC VELOCITY IN A ROCKET CHAMBER

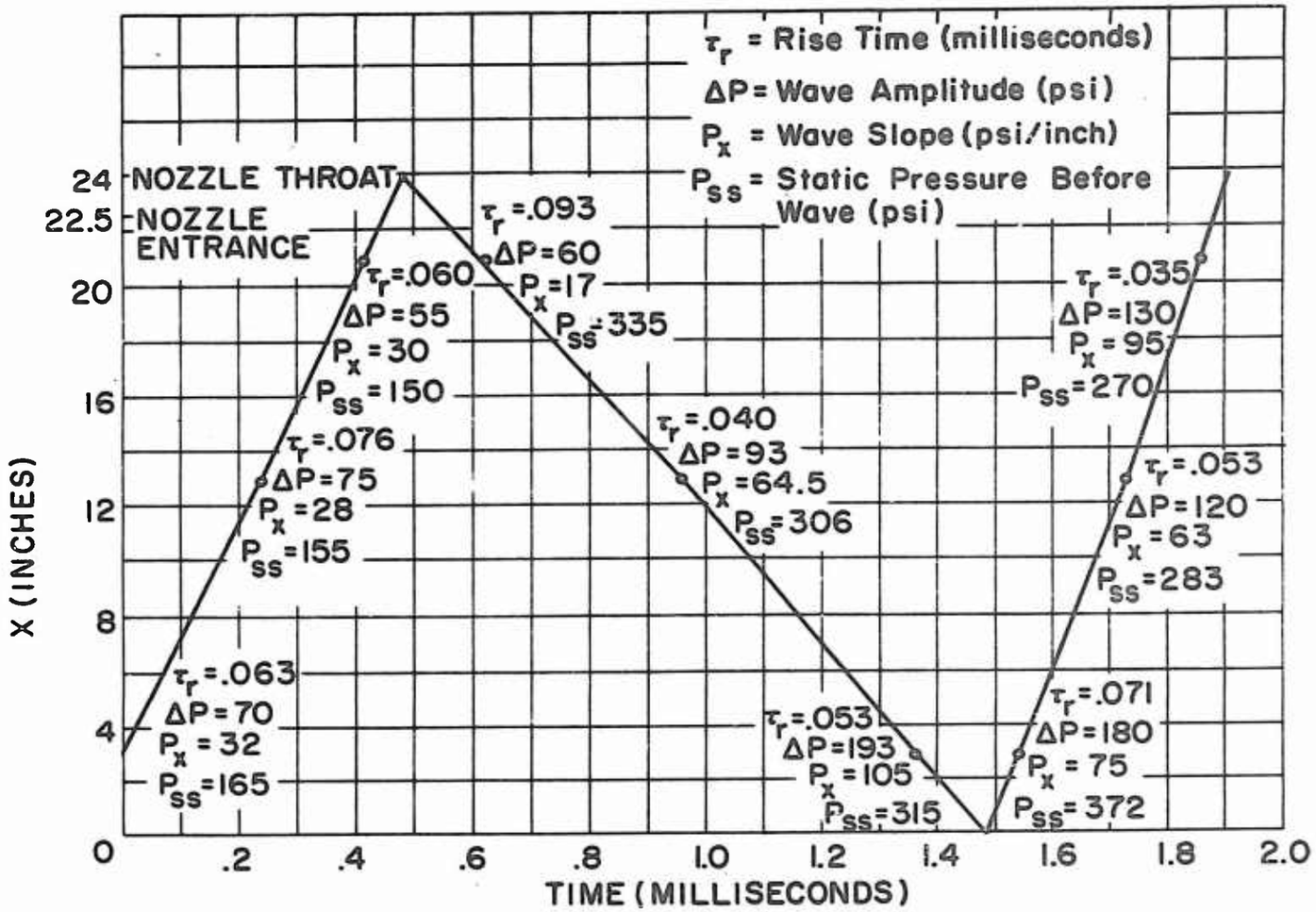

FIGURE 4.12 WAVE ANALYSIS OF A GENERATED WAVE IN A ROCKET MOTOR

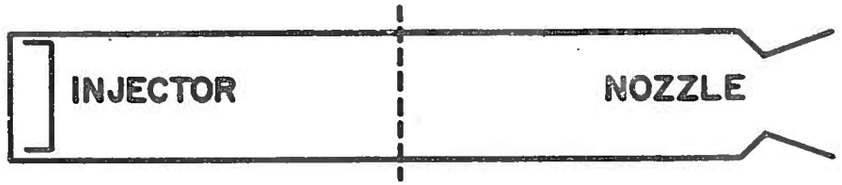

STATION & DIRECTION	INJECTOR DOWNSTREAM	NOZZLE DOWNSTREAM	NOZZLE UPSTREAM	INJECTOR UPSTREAM
SPEED OF SOUND				
TEST 1	2725	3200	3250	3600
TEST 2	2620	2750	2900	2950
TEST 3	2600	2900	3000	3100
TEST 4	2700	2650	2700	2700

TEST 1, 2, 3 SPONTANEOUS INSTABILITY

TEST 4 NO SPONTANEOUS INSTABILITY

FIGURE 4.13 LOCAL SPEED OF SOUND

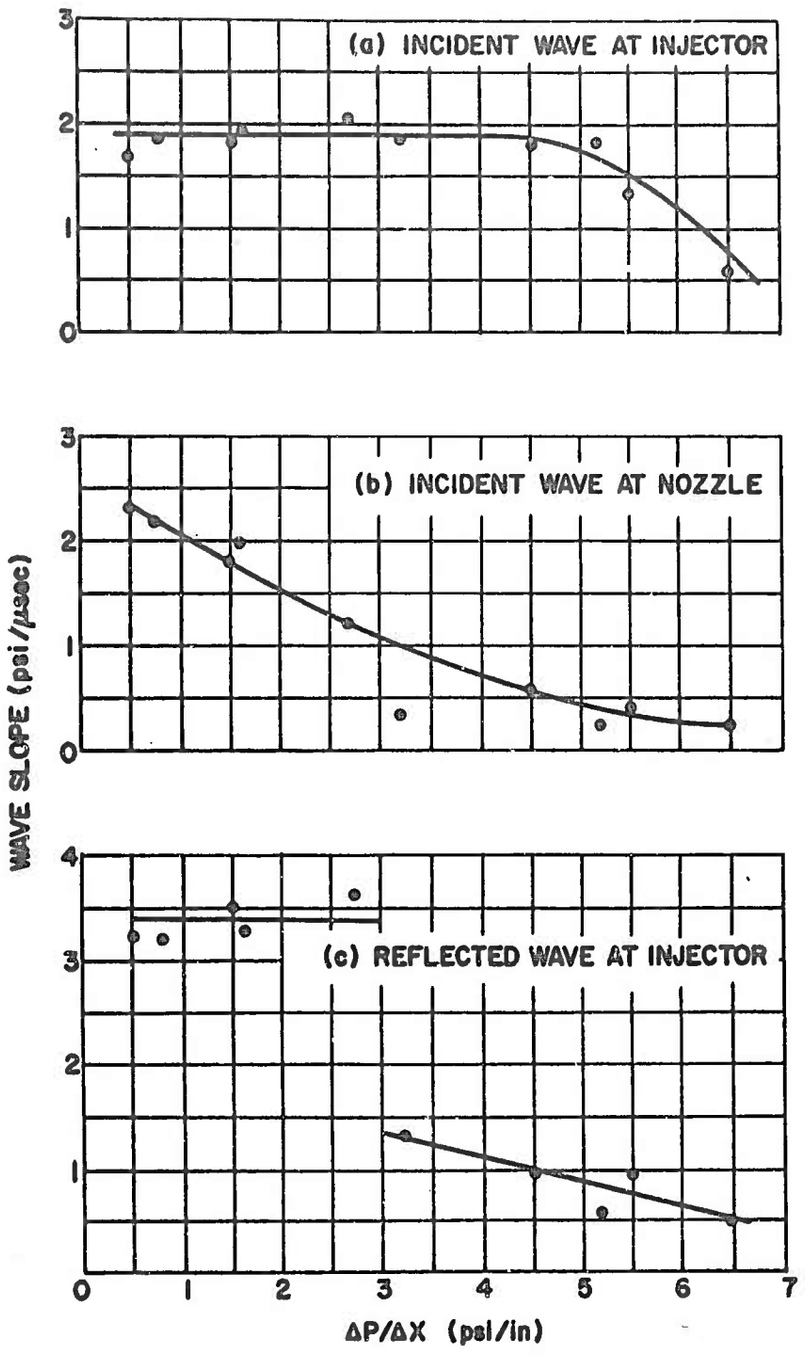

FIGURE 4.14 WAVE SLOPE vs. PRESSURE GRADIENT

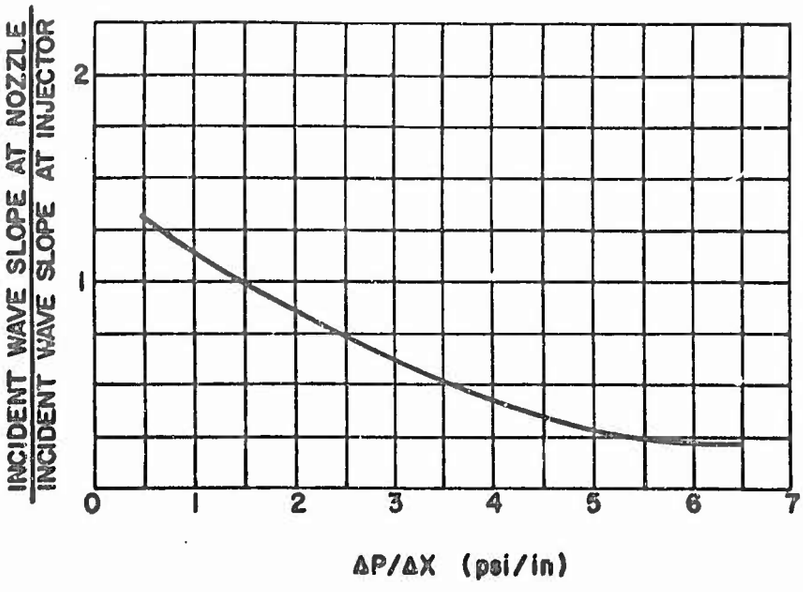

(a)

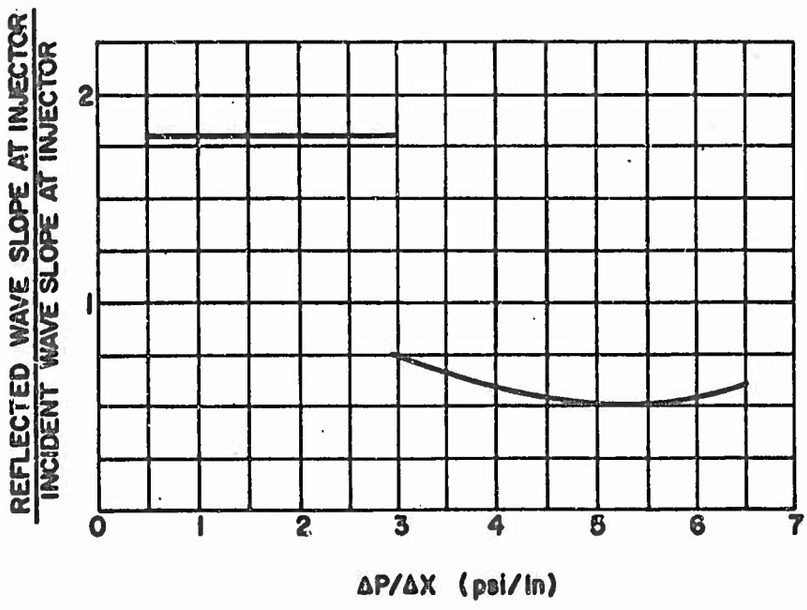

(b)

FIGURE 4.15 NORMALIZED WAVE SLOPE vs. PRESSURE GRADIENT

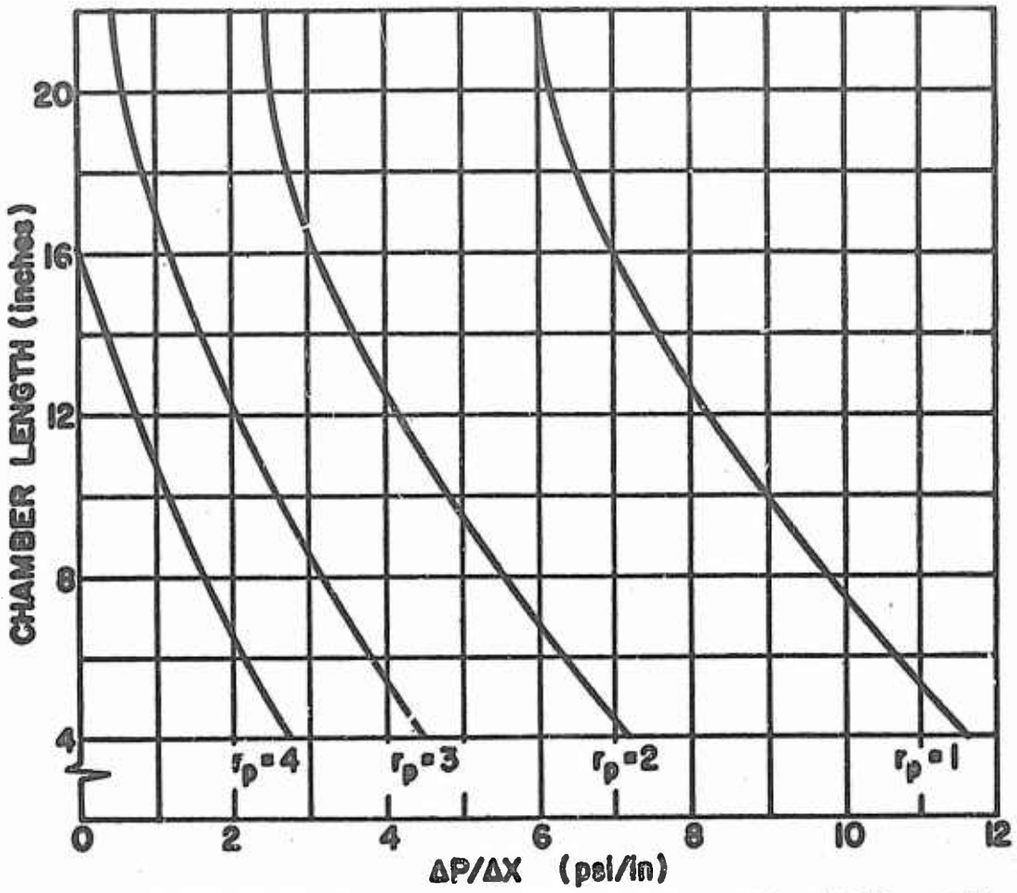

$$r_p = \frac{\text{BASE PRESSURE AT INJECTOR BEFORE REFLECTED WAVE}}{\text{BASE PRESSURE AT INJECTOR BEFORE INCIDENT WAVE}}$$

FIG. 4.16 BASE PRESSURE AMPLIFICATION